Investigation of instability growth in a hypersonic boundary layer using schlieren visualization

Leroy Benjamin

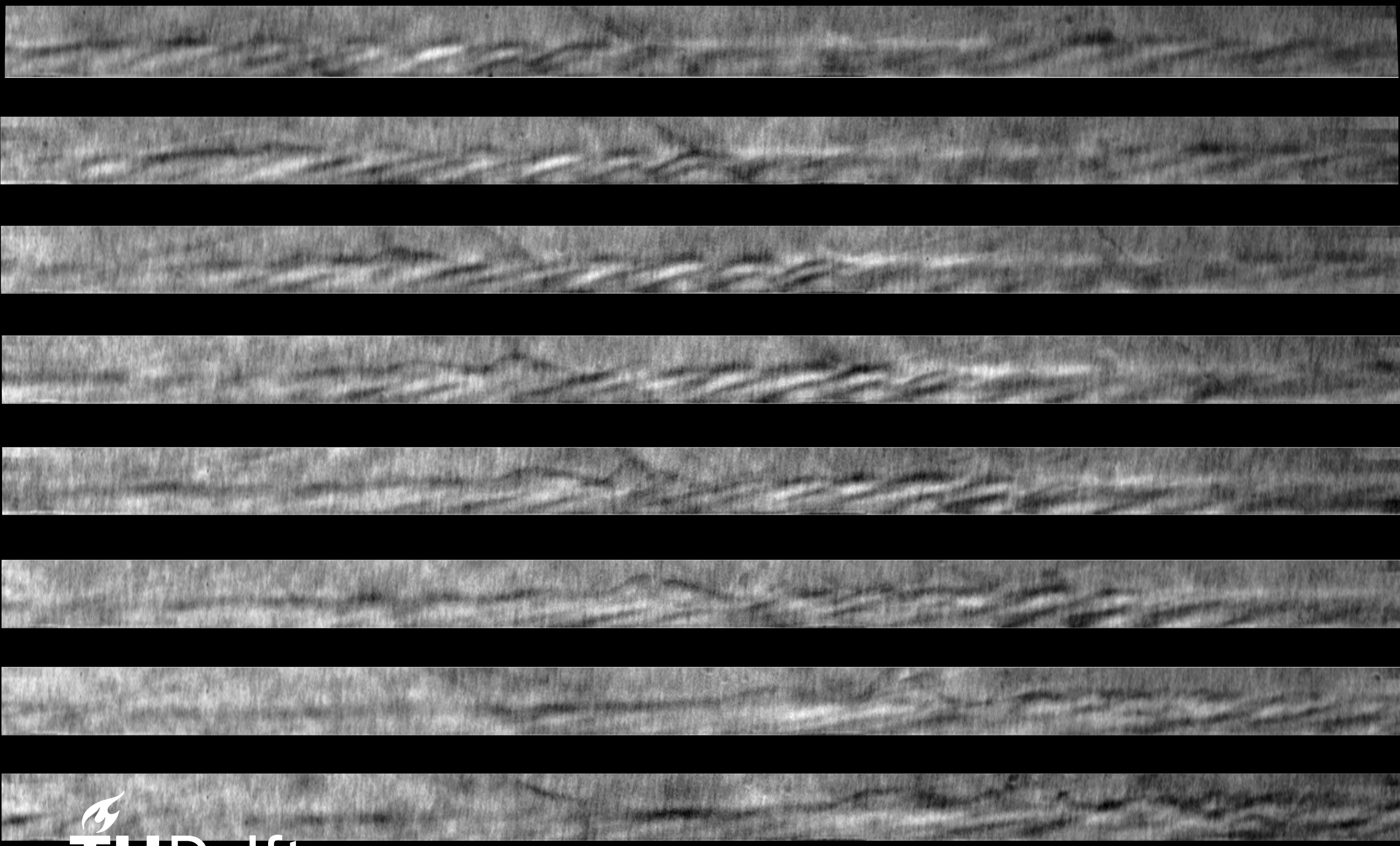

TU Delft

Investigation of instability growth in a hypersonic boundary layer using schlieren visualization

by

Leroy Benjamin

to obtain the degree of Master of Science
at the Delft University of Technology,
to be defended publicly on Thursday August 24, 2017 at 13:30.

Student number:	4412257	
Thesis committee:	Dr. Alexander Wagner,	DLR, supervisor
	Dr. ir. F. F. J. Schrijer,	TU Delft, supervisor
	Dr. ir. B. W. van Oudheusden,	TU Delft
	Dr. F. Avallone,	TU Delft

This thesis is confidential and cannot be made public until August 31, 2018.

Acknowledgment

Silent gratitude isn't much use to anyone. . .

The journey to complete this work was filled with its share of joy and pain. I will like to take this moment to thank my supervisors Dr. Alexander Wagner and Dr. ir. F.F.J. Schrijer for their support and insights throughout the duration of the thesis. I also thank my friends who were a part of my masters journey. Of course mentioning each one of you will be quite tedious, you know how important you are to me and how much our interactions have helped. Thank you guys for all the help!

Finally I thank my parents and siblings, who have been understanding and patient with me throughout my life.

Leroy Benjamin
Delft, August 2017

Abstract

Hypersonic boundary layer transition plays a significant role in the design of hypersonic vehicles as a turbulent boundary layer has higher heat transfer compared to a laminar boundary layer. Transition is a complex phenomenon and various parameters decide how a boundary layer undergoes transition to turbulence. For a hypersonic cone boundary layer, the linear stability theory predicts the second mode waves to be the most unstable instability wave. Hence studying the second mode wave development is crucial from the point of view of hypersonic boundary layer transition control.

The second mode waves cause density fluctuations which enables these structures to be visualized in a schlieren image. This thesis applies the wavelet analysis to schlieren images to study the growth of the second mode waves in a hypersonic boundary layer. The wavelet analysis is a signal processing technique which allows to study waves in frequency/wavelength spectrum without loss in temporal/spatial information unlike conventional techniques like the Fourier analysis. High speed schlieren visualization experiments were performed on a 7° half angle cone in the high enthalpy shock tunnel in Goettingen (HEG), and the images which successfully captured the instability waves were used for the present study.

By applying the wavelet analysis to schlieren images the following is concluded 1) the second mode waves amplifies structures towards the boundary layer edge, 2) A linear wave packet has higher amplitudes concentrated at the leading edge, which gets redistributed towards the center first and then later to a uniform distribution over the whole length of the wave packet, 3) the first harmonic of the second mode wave develops in regions of strong second mode growth, 4) analysis on the growth rates of the second mode fundamental and its first harmonic showed that in regions of harmonic growth there was fundamental wave decay and vice versa, implying a possible energy exchange between the two waves and 5) strong low frequency waves were also detected in the schlieren images, these waves were more dominant during transition while the second mode waves and its harmonics die.

The results from the study sheds more light into the instability development in a hypersonic boundary layer in the following ways: 1) the property of the second mode waves to amplify structures near the boundary layer edge explains why early researchers observed these waves close to the boundary layer edge, 2) linear wave packets with higher amplitudes concentrated at the leading edge of the wave packet, which was predicted from DNS simulations has been experimentally verified, 3) interaction between the fundamental wave and its first harmonic is shown by analysis on the spatial growth rates and 4) the strong presence of low frequency structures during boundary layer transition shows the second mode instability is not the only dominant instability for the hypersonic cone boundary layer under adiabatic wall conditions, as predicted by the linear stability theory.

Nomenclature

Acronyms

Symbol	Description	Dimensions	Units
CWT	continuous wavelet transform	-	-
DNS	direct numerical simulation	-	-
DWT	discrete wavelet transform	-	-

Greek Symbols

Symbol	Description	Dimensions	Units
α	amplification factor	L^{-1}	m^{-1}
δ	boundary layer thickness	L	mm

Roman Symbols

Symbol	Description	Dimensions	Units
A	wave amplitude	–	–
a	speed of sound	L/T	$\mathrm{m}\cdot \mathrm{s}^{-1}$
c	wave speed	L/T	$\mathrm{m}\cdot \mathrm{s}^{-1}$
C_{cross}	cross correlation coefficient	–	–
C_{WT}	wavelet transform coefficient	-	-
h	enthalpy	$\mathrm{L}^2\mathrm{T}^{-2}$	J/kg
M	Mach number	-	-
M_c	relative Mach number	–	–
N_p	number of wave peaks	-	-
p	pressure	$\mathrm{ML}^{-1}\mathrm{T}^{-2}$	Pa
q	heat flux	MT^{-3}	$\mathrm{W/m}^2$
Re_m	unit Reynolds number	L^{-1}	m^{-1}

Subscripts

Symbol	Description	Dimensions	Units
0	total flow condition		
∞	flow condition outside boundary layer		
e	flow condition at boundary layer edge		

Contents

List of Figures

List of Tables

1

Introduction

A major thrust in aerospace research has always been the desire to fly faster, [2]. Fig. 1.1 shows the flight speeds over the years. The Wright flyer first achieved powered flight at a speed of 35 mph in the year 1903 and in a span of 60 years Yuri Gagarin became the first man to travel at hypersonic speeds in 1961. Vehicles in the higher end of the spectrum fall under the hypersonic regime, which has its own unique aerodynamic characteristics, Anderson [2]. A flow is generally termed hypersonic when its velocity is greater than five times the speed of sound (Mach≥5) [2]. The Hypersonic International Flight Research Experimentation (HIFiRE) is a recent research program which aims to explore the basic technologies required to achieve practical hypersonic flight. Flying at hypersonic speeds will revolutionize long distance flight and provide cost effective access to space. A recent experimental flight called HyShot V under the HIFiRE program took place in July, 2017. HyShot V is a free flying hypersonic glider which flies at Mach 8, with an aim to learn how to manoeuvre and fly hypersonic vehicles at high altitude. Hypersonic vehicles will be an integral part of transportation in the future and hence research in this area is crucial.

The biggest challenge in the design of hypersonic vehicles is the heat transfer to the vehicle caused by the deceleration of the high speed flow within the boundary layer. The boundary layer is a thin layer surrounding a body that moves through a fluid, where viscous effects are dominant and they cause the flow to decelerate within the layer. The kinetic energy of the high speed flow is dissipated as heat due to friction. Due to the dissipated heat, the temperature within the boundary layer reaches high magnitudes, in reentry cases sufficient to ionize air. The high temperatures within the boundary layer consequently cause high heat transfer from the hot boundary layer to the surface of the vehicle. The heat transfer can affect the structural integrity of the vehicle, which is why the reentry phase of a spacecraft is prone to accidents, most notably the space shuttle Discovery which had damaged heat shields and was destroyed during reentry into earths atmosphere.

The heat transfer rates depend primarily on the state of the boundary layer (laminar/turbulent). The process by which the boundary layer shifts from laminar to turbulent state is called boundary layer transition. In a turbulent boundary layer due to the chaotic motion of the flow there is more energy transfer from the outer flow to the energy deficit regions close to the surface, which leads to larger gradients at the wall which in turn causes higher aerodynamic heat transfer to the surface and can affect the structural integrity of the vehicle. Hence boundary layer transition plays an important role in the design of hypersonic vehicles. Thermal protection system (TPS) designers usually follow a conservative approach of assuming a completely turbulent flow over the vehicle. This leads to increased structural weight as turbulent flow heat transfer is higher than that of laminar flow, and more material is added to the external structure to protect the payload inside. Studies on the National Aerospace Plane (NASP) showed that the payload-to-gross-weight ratio will double if the boundary layer were fully laminar when compared to fully turbulent [4]. This motivates the study of transition in a hypersonic boundary layer.

Hypersonic boundary layer transition depends on a number of flow parameters. The most important parameters are: 1) Mach number: based on stability theory it is shown that the stability of a laminar boundary is enhanced at higher Mach numbers, 2) Environment: disturbances from the environment like free stream turbulence and disturbances from the turbulent boundary layer on a wind tunnel wall can induce early transition. Surface roughness also affects transition and is known as roughness induced transition. For hypersonic vehicles surface roughness can develop during flight due to friction between surface and high speed flow, which can causes early transition. 3) Angle of attack: three dimensional flows can have a severe effect on transition. For a cone as the angle of attack is increased, transition is delayed on the windward side and is advanced on the leeward side. The delay in transition on the windward side is opposite to what is expected, since the Mach number is reduced and the local Reynolds number increases, the effect of both should be to cause early transition. But from experiments transition moves rearward on the windward side. This shows a three dimensional effect and is called cross flow induced transition and 4) Wall temperature: moderate cooling stabilizes a hypersonic boundary layer, just like in low speeds. For highly cooled walls there are cases where a reversal happens and transition occurs earlier.

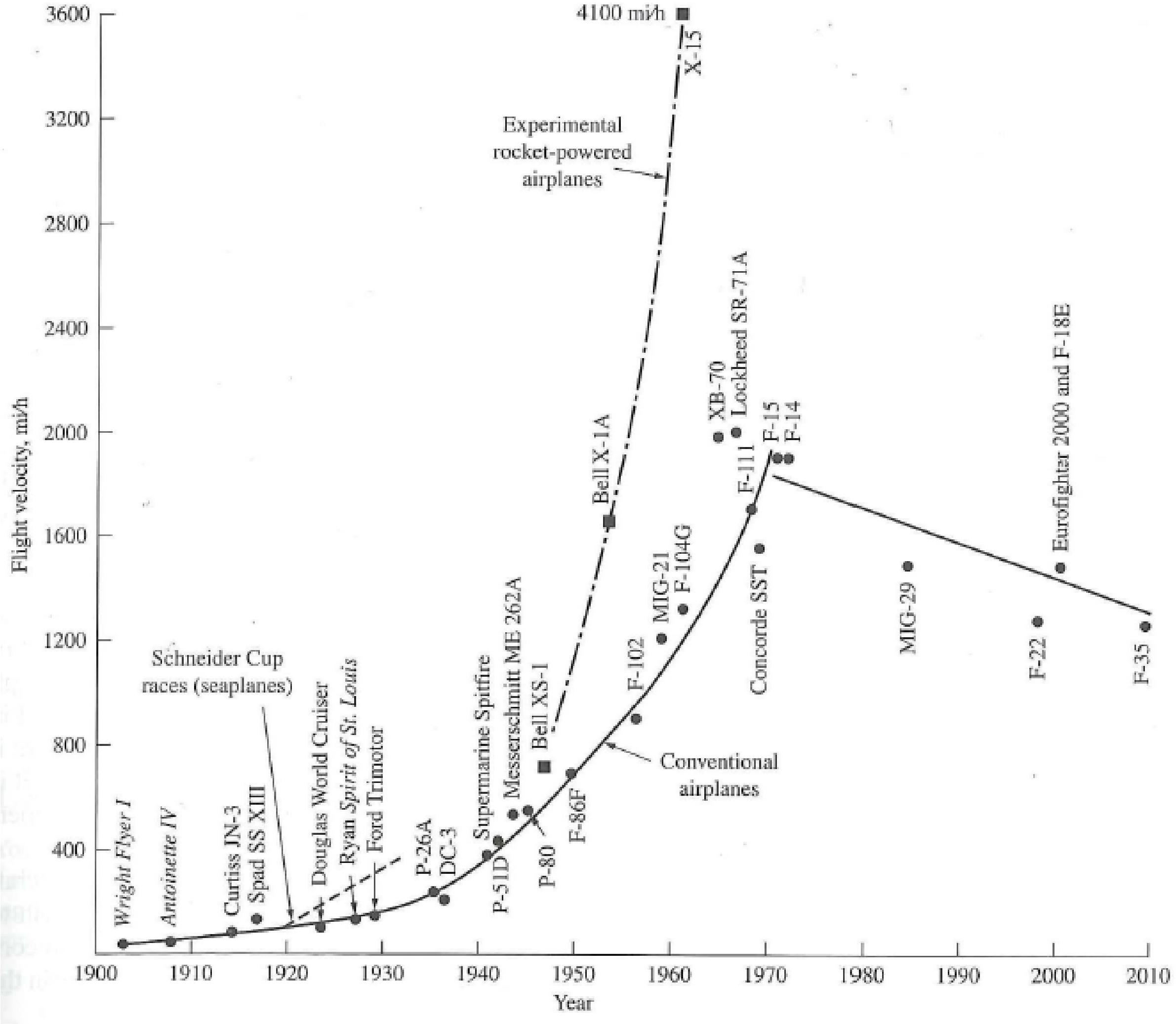

Figure 1.1: Flight speed over the years, Anderson [1].

All the parameters that affect transition make it a complex phenomenon to study and understand. For a smooth wall, the boundary layer develops instability waves, which grow and eventually breakdown into turbulence. The Tollmein-Schlitling (TS) waves is one type of instability wave which develop in subsonic boundary layers. For two dimensional hypersonic boundary layers under adiabatic smooth wall condition the dominant instability is the second mode waves [27]. This thesis aims to study the the growth of second mode waves in a hypersonic boundary layer. In the following sections a brief review of the linear stability theory is provided, since it is the theoretical model that initially predicted the dominance of second mode wave, followed by a discussion on the second mode waves.

1.1. Linear stability theory: a brief review

In this section a brief review of the linear stability theory is presented, a detailed study of this theory is provided by Mack [27, 28]. The aim of the linear stability theory is to determine if a small sinusoidal disturbance introduced into a laminar boundary layer will amplify or damp. The stability theory cannot predict the location of transition or the non linear process through which transition to turbulence occurs. The theory can predict the range of unstable frequencies and unstable boundary layer profiles. The sinusoidal disturbance introduced into the laminar boundary layer is small enough so that the linear theory can be used. The steps performed in linear stability analysis can be summarized into the following points :

1. The flow parameters in the Navier stokes equation are divided into mean flow term and fluctuation term, see equation 1.1, where q is any flow variable (velocity, pressure, temperature) Q is the mean flow property and q' is the fluctuation term.
$$q = Q + q' \tag{1.1}$$
2. The disturbances (q') are assumed to be small enough so that linear theory can be applied. The flow is assumed to be locally parallel that is parallel to the surface.
3. **Linearize** the equations (neglect the higher order terms) and subtract mean flow variables.
4. **Normal Mode analysis** : In this the disturbance is assumed to be a superposition of different modes (physically it can be viewed as superposition of waves). In the normal mode analysis, no interaction between the individual modes exist. In Eqn 1.2 α_s, β_s are the wave numbers in the stream wise and span wise direction and ω_s is the circular frequency of the disturbance.
$$q' = q(y)\exp[i(\alpha_s x + \beta_s z - \omega_s t)] \tag{1.2}$$
5. Substitute Eqn 1.2 for the disturbance variable of each flow property(u', v', p'...). The resulting equations will pose an eigenvalue problem. After solving the eigenvalue problem, it can be determined if a disturbance amplifies, damps or is neutral by analyzing the exponent in Eqn. 1.2. For a spatial stability analysis ω_s is assumed to be real and α_s is complex ($\alpha_s = \alpha_r + \alpha_i$). For a disturbance that amplifies α_i should be negative.

1.1.1. Second mode instability

Mack [27] performed the linear stability analysis on a compressible boundary layer and found that for supersonic boundary layers besides the first mode instability there exists a higher mode which is more dominant (see Fig. 1.2). If the Mach number is greater than 4, adiabatic wall and the boundary layer is two dimensional, the second mode instability is the dominant instability in the boundary layer. The second mode is an acoustic wave which reflects back and forth from the wall and the relative sonic line [28] as shown in Fig. 1.3. In Fig. 1.3 the compression waves are indicated by solid lines and expansion waves by dotted lines. The sonic line is defined as the height at which the convective Mach number M_c, is equal to 1. The convective Mach number is defined by equation 1.3, where c is the second mode wave speed, $u(y)$ is the velocity at a particular distance from the wall and $a(y)$ is the speed of sound at that height.

$$M_c = \frac{c - u(y)}{a(y)} \tag{1.3}$$

Mack [29, 30] found the following properties for the second mode wave: 1) second mode exists when there is a region of local supersonic flow relative to the phase speed of the second mode wave (M_c>1) embedded in the boundary layer, as seen in the region between the wall and sonic line in Fig. 1.3, 2) The wave propagation speed is close to free stream velocity, 3) the wavelength is approximately twice the boundary layer thickness, 4) the waves cause fluctuations in density primarily and 5) the second mode is most unstable for wave angle of 0°.

Since the second mode waves induce fluctuations in density, these flow structures can be visualized using schlieren technique, which depends on density gradients for visualization, see Fig 1.4. As these flow structures are captured in a schlieren image, it motivated researchers to apply signal processing techniques on a schlieren image to extract properties of the second mode wave. The second mode wave is also called Mack mode or acoustic mode.

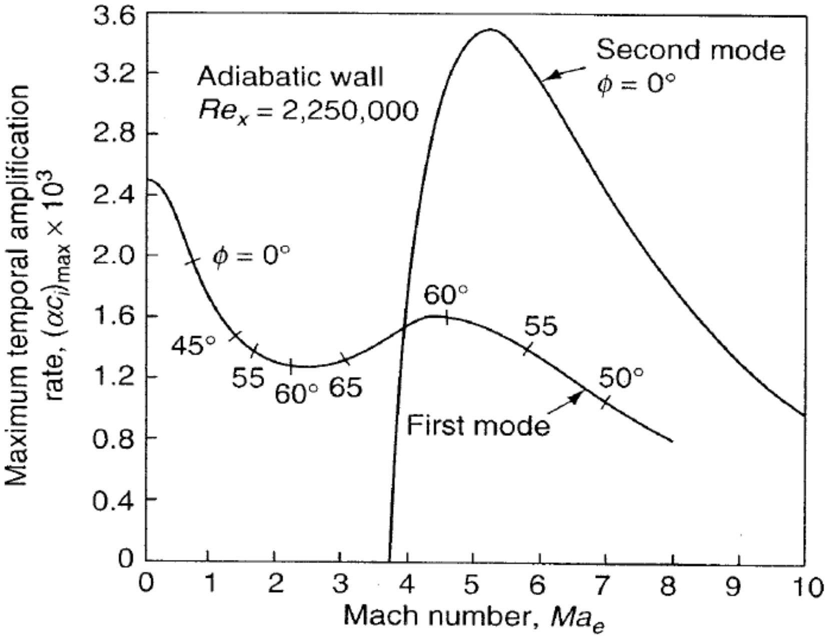

Figure 1.2: Effect of Mach number on the amplification rate, White [52].

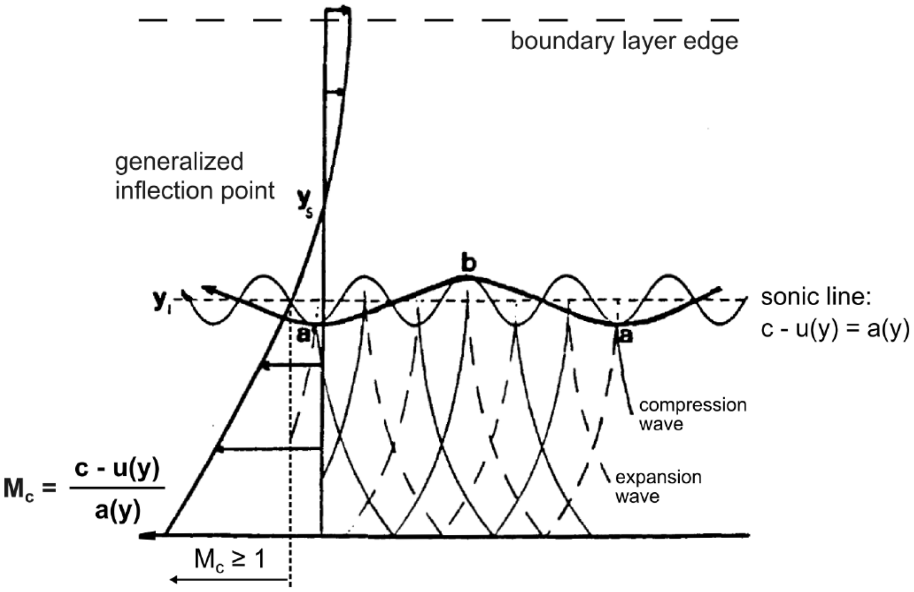

Figure 1.3: Figure shows the propagation of second mode as an acoustic wave, Wagner [50].

Figure 1.4: Second mode wave visualized on a cone, adapted from Casper et al. [6].

Figure 1.5: Taking Fourier transform of a signal, Misiti et al. [31].

1.2. Signal processing techniques

Signal processing techniques are used on signals obtained from experiments. This section introduces the basics of these techniques to help interpret the results discussed in chapter 2.

1.2.1. Fourier transform

The Fourier transform is a mathematical technique which decomposes a signal into sinusoids, given by equation 1.4. Where $f(t)$ is the signal measured in the time domain.

$$F(\omega) = \int_{-\infty}^{\infty} f(t) \exp(-i\omega t) dt \tag{1.4}$$

$$\exp(i\omega t) = \cos(\omega t) + i \sin(\omega t) \tag{1.5}$$

The sine and cosine waves are called the basis functions. The Fourier transform assigns an amplitude to sine/cosine waves of specific frequencies, which results in a set of scaled sine and cosine waves that can be added to produce the original signal [44]. The effect of taking the Fourier transform is pictured in Fig. 1.5. A physical signal (extreme left Fig. 1.5) like pressure/velocity/temperature is measured in the time domain and performing the Fourier analysis gives the dominant frequency in the measured signal. The frequency contained in the measured signal, corresponds to the frequency of the maximum amplitude in the amplitude-frequency spectrum shown in the extreme right of Fig. 1.5. The Fourier transform can be thought of as a technique that converts physical signals measured in the amplitude-time domain to an amplitude-frequency domain.

The Fourier transform has one drawback. In converting the signal to a frequency domain, the time information is lost. Based on the amplitude-frequency plot it is not possible to deduce when a wave moves over the sensor. For signals that do not change much with time (stationary signals), this drawback does not affect the analysis much. However most of the signals that are measured in a lab have non stationary characteristics like abrupt changes or coherent structures in turbulence.

One way to overcome this drawback is to use the short time Fourier transform (STFT). In STFT the Fourier transform is taken only for a portion of the signal and mapped to a frequency-time domain as shown in Fig. 1.6. While this technique is beneficial there are some disadvantages like the time window size is fixed and taking a short time window will result in poor frequency resolution. The wavelet analysis discussed in the next section is one technique which over comes these drawbacks and is well suited to study non stationary signals.

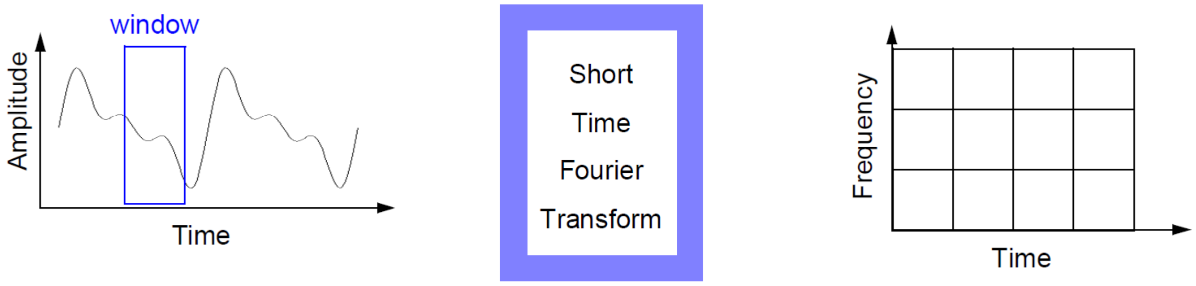

Figure 1.6: Taking short time Fourier transform of a signal, Misiti et al. [31].

1.2.2. Wavelet analysis

The Fourier transform decomposes a signal into sine and cosine (basis functions) components of different frequencies. The wavelet analysis similar to Fourier transform, decomposes a given signal into scaled versions of a mother wavelet, which serves as the basis function for a wavelet transform. The concepts of the wavelet transform are explained by taking the wavelet transform of a row vector from a schlieren image, shown in Fig. 1.7 (top).

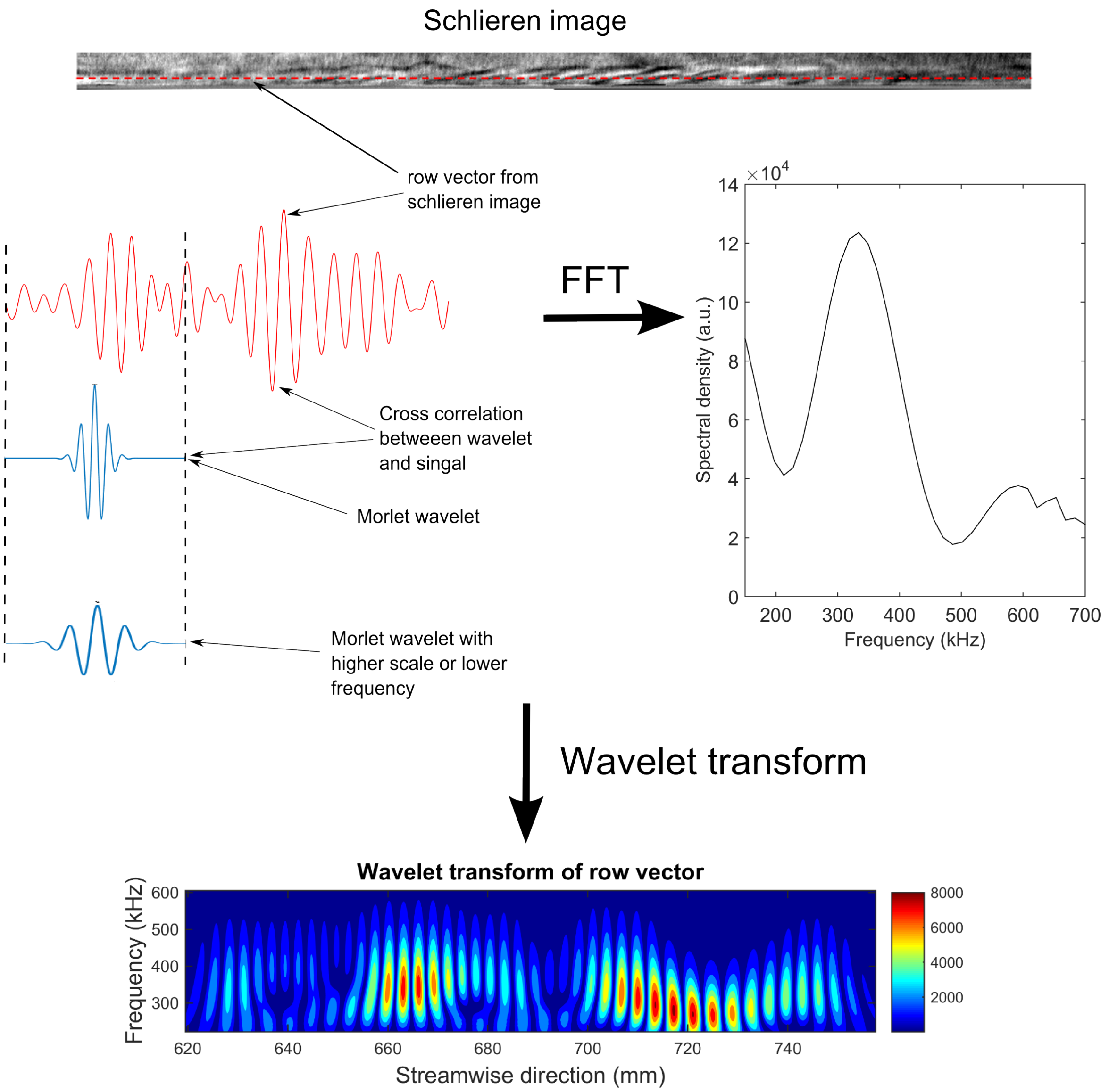

Figure 1.7: Difference between taking the Fourier and wavelet transform of a row vector from schlieren image. Figure demonstrates that while taking the wavelet transform there is no loss in spatial information.

The first step to perform the wavelet transform, is to select a mother wavelet, a few wavelets are shown in Fig. 1.8. The wavelet chosen for the analysis should be representative of the signal that has to be analyzed. For example if the objective is to find out a sudden discontinuity in a signal then the haar wavelet is best suited. For this study, the objective is to analyze the second mode waves which are sinusoidal fluctuations; hence the Morlet wavelet (see Fig. 1.8) which is also sinusoidal in nature is selected for this analysis.

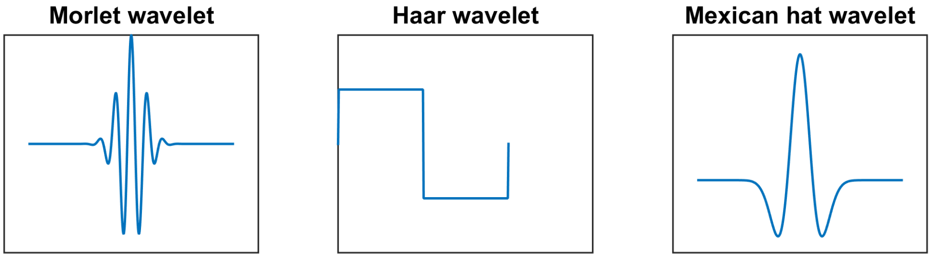

Figure 1.8: Different types of mother wavelets.

An important property of the mother wavelet is its *scale*, which is the wavelet counterpart for frequency of a basis function in FFT. The scale of a wavelet is an indication of the extent it is stretched or compressed, represented by the variable a (see Fig. 1.9). It is understood directly that a small scale wavelet has high frequency and a large scale wavelet has low frequency. The scale of a wavelet is related to its frequency through Eqn. 1.6. The relation between scale and frequency is only approximate [32]. F_c is the center frequency of the wavelet, which is the frequency of a periodic signal associated with the wavelet. F_s is the sampling frequency of the signal under analysis.

$$F_a = \frac{F_c}{a(1/F_s)} \tag{1.6}$$

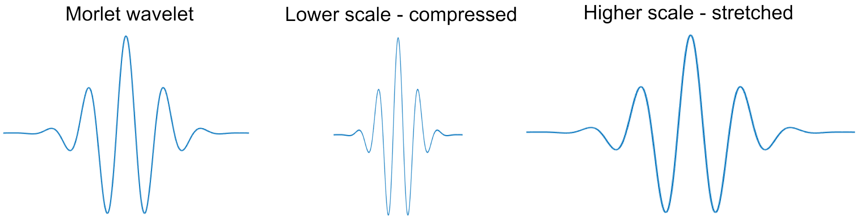

Figure 1.9: Morlet wavelet of different scales.

In the wavelet analysis the mother wavelet is shifted over the entire signal under analysis. For every shift an inner product of the wavelet and the portion of the signal is taken, this is similar to taking a cross correlation (see step1 and step 2 in Fig. 1.10). This generates wavelet coefficients, which give an indication of how similar a portion of the signal is to the mother wavelet. Larger the coefficients more similar that section of the signal is to the mother wavelet. This process is repeated for all scales of interest generating a matrix of wavelet coefficients, see Fig. 1.7 bottom. Every horizontal row of Fig. 1.7 bottom is generated by taking the cross correlation of the signal and a Morlet wavelet of fixed scale.

Fig. 1.7 shows the result of applying the wavelet transform to a row of a schlieren image. The advantage of using the wavelet transform is clear from Fig. 1.7. Taking the Fourier transform of the signal (middle right) the spatial information is lost, while when the wavelet transform is taken (bottom) the location of the second mode is also known in addition to the frequency of the waves. From the large wavelet coefficients in Fig. 1.7 (bottom), the second mode waves are present between 650-680 and 700-740 mm. A visual comparison between the schlieren image and the wavelet transform shows that the wavelet transform does indeed provide the location of the second mode waves. In Fig. 1.7 the row vector from the schlieren image is band pass filtered around the second mode frequency for illustration purposes, to apply the wavelet transform no noise filtering is required. More details of the wavelet analysis are discussed in section 3.2.

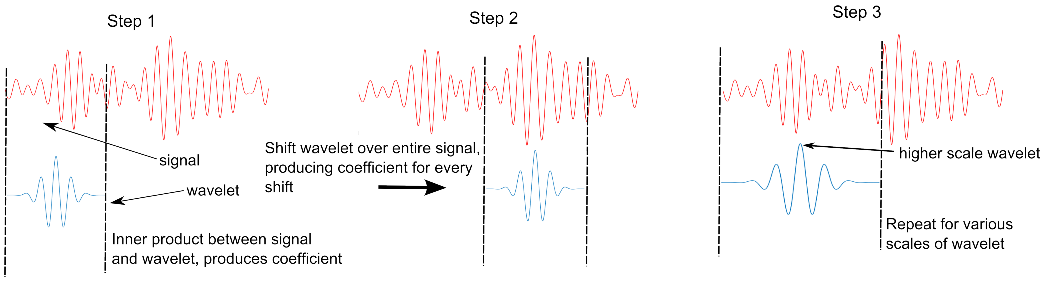

Figure 1.10: Cross correlation between wavelet and signal.

1.3. Thesis Objective and Outline

The objective of this thesis is to develop an algorithm, which applies the wavelet transform to schlieren images to study the following instability wave properties:

- the growth of harmonics of the fundamental instability wave
- the growth rate of the instability wave and
- the instability wave breakdown process.

The subject is introduced in this chapter. In chapter 2 a detailed review of the experimental and computational studies of second mode development is discussed. The literature review is divided into three sections based on the tool used to study the second mode waves, section 2.1 discusses results from hot wire and surface mounted sensors, section 2.2 presents results from visualization based literature and section 2.3 presents the numerical results. In section 2.5 the research proposal and research questions are formulated based on the literature review. The methodology is addressed in chapter 3. The schlieren experimental setup and the test flow conditions are presented in section 3.1. In section 3.2 a further discussion on the wavelet analysis and its application to schlieren images is discussed. The results are presented in chapter 4. The chapter is subdivided into the following sections: 1) section 4.2 studies the second of mode waves, 2) section 4.3 studies the first harmonic of the second mode fundamental waves and 3) section 4.4 discusses the low frequency waves observed in schlieren images. The conclusions of the study is finally presented in in chapter 5.

2

Literature Review

Over the years the scientific community has used a number of techniques to study the second mode disturbances like hot wire anemometer, PicoCoulomB (PCB) transducers [12] and heat flux gages [37]. Recently, optical and visualization based techniques have gained popularity to study the second mode waves. These combine several benefits: they are non-intrusive, able to measure away from the model surface, and typically have bandwidths that are limited only by the recording electronics. This chapter reviews the research performed over the years to study the growth and breakdown of second mode waves. The sections are divided by the technique used in the respective investigations. In section 2.1 investigations using surface mounted techniques are reviewed followed by visualization based techniques and numerical simulations in sections 2.2 and 2.3. In all the experimental and computational investigations presented in this chapter the model used was a cone with a cold wall under hypersonic conditions, hence the second mode wave is expected to be the dominant instability.

2.1. Results from experiments using surface mounted and probe techniques

The study of Mack [28] indicated that natural transition for a two dimensional hypersonic boundary layer with cold wall condition is dominated by the second mode waves. One of the earliest experimental investigations to validate the presence of second mode disturbances in a hypersonic cone boundary layer was that of Kendall [17]. He compared the experimentally measured amplification rates to the theoretical prediction by Mack, see Fig. 2.1a. Although the growth rates did not agree, the most amplified frequencies did which led Kendall [17] to conclude that the measured disturbances were the second mode waves. Further experiments using hot wire anemometers proved the following: 1) wave speed to be $0.9U_\infty$[18], 2) the wavelength to be approximately twice the boundary layer thickness [10, 48] and 3) the waves cause larger density fluctuations than velocity fluctuations [10, 48]. These properties were also experimentally observed by researchers using PicoCoulomB (PCB) transducers and atomic layer thermopile (ALTP) sensors [7, 12, 37]. It is emphasized once again that all the experiments reported here were performed on a cone under hypersonic and cold wall conditions.

Fig. 2.1b, is the disturbance spectrum of a hot wire signal for varying Reynolds number at a fixed stream wise location.The signal was measured at the location of energy peak in the boundary layer. Peaks that occur in the frequency range around 70 kHz, correspond to the frequency of the fundamental second mode wave. Secondary peaks are also observed at higher frequencies (140 kHz), these are the first harmonics. The harmonics of the fundamental frequency were also observed in a hypersonic quiet wind tunnel [20], thus ruling out the possibility that free stream disturbances cause the higher harmonics. The presence of harmonics imply non-linear growth, as these frequencies were not predicted to be dominant by the linear theory. Harmonics were also observed using PCB transducers by Berridge et al. [5], Casper et al. [9]. In Fig. 2.1b it also seen that for thicker boundary layer (lower Reynolds number implies thicker boundary layer) the frequency of the second mode waves is lower, this was dubbed as the *tuning* of the hypersonic boundary layer by Stetson and Kimmel [46].

Kimmel et al. [18] cross correlated circumferentially separated probes to find the span wise extent of the wave packet to be 4δ. It was also observed that as the second mode waves grew, their span wise extent reduced, implying the wave angles were non zero. Casper et al. [7] used span wise PCB transducers to generate

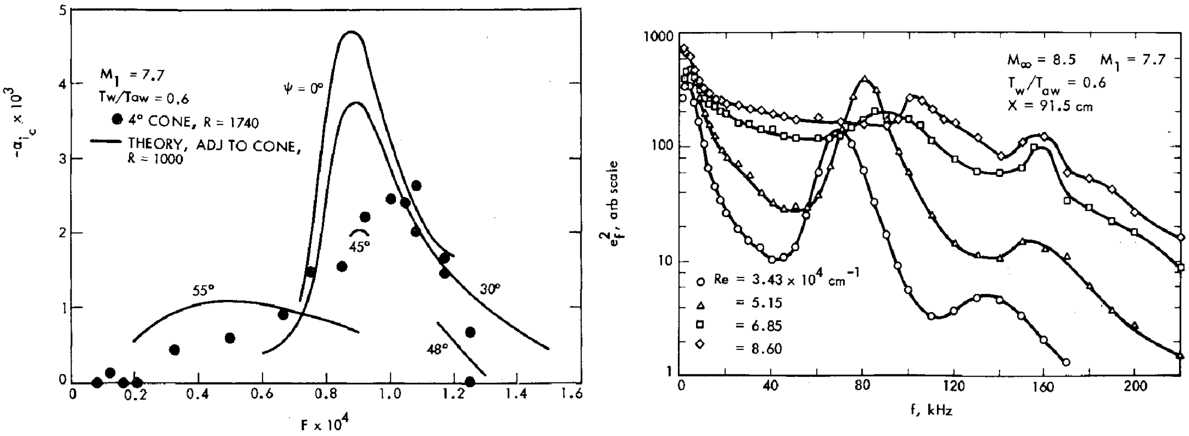

(a) Comparision of amplification factor with Mack's theoretical results. $\psi = 55°$ is for first mode wave and rest are for second mode waves. F is non-dimensional frequency

(b) Energy spectrum at a fixed stream wise location for varying Reynolds number. The signal was measured at the location of energy peak in the boundary layer.

Figure 2.1: Results from Kendall [17].

a pressure contour (Fig. 2.2). The circumferential extent of the second mode structures were found to be 4δ, agreeing with Kimmel et al. [18]. Kimmel also found the structure angle of the wave packet in the wall normal direction (Fig. 2.3a). Second mode structure angle represents the inclination of the line of constant phase and the wall (see drawing in Fig. 2.3a). The second mode structure angle was found to be low in the inner half of the boundary layer, increase from 15° at $y/\delta = 0.7$ to a maximum of 60° close the boundary layer edge.

Demetriades [10] observed that the second mode cause higher temperature fluctuations than velocity fluctuations, as seen in the temperature fluctuations in Fig. 2.4a. Fluctuations in temperature affect the density through the equation of state ($p = \rho RT$). The figure also shows that the second mode waves are concentrated close to the boundary layer edge. Kimmel et al. [18] cross correlated vertically separated hot wire signals for varying Reynolds number shown in Fig. 2.4b. From the figure it is seen that for the lower Reynolds number the second mode waves are concentrated at the boundary layer edge and for the higher Reynolds number the vertical extent of the waves increase.

The growth rate of the second mode wave is defined as given in equation 2.1, where A_1, A_2 is the wave amplitude corresponding to second mode frequency measured upstream and downstream and Δs is the distance between the sensors.

$$-\alpha = \frac{\ln(A_1/A_2)}{\Delta s} \tag{2.1}$$

Stetson and Kimmel [47] plotted the maximum second mode growth rates against the Reynolds number (Fig. 2.3b) and observed that the second mode growth rates reduced at the Reynolds number larger than 1400, for which harmonics developed. Stetson and Kimmel [47] proposed that the decrease in the amplification factor of the fundamental wave can be due to non-linear growth, which amplifies the harmonics during breakdown. However, Roediger et al. [37] study on the growth rates of harmonics, showed no significant increase in the growth rates of the harmonics during breakdown. Roediger et al. [37] found the second mode wave and the first harmonic to have amplification factors of $25\,\mathrm{m}^{-1}$ and $27\,\mathrm{m}^{-1}$. In the experiments performed by Estorf et al. [12] the maximum amplification factor obtained was $6\,\mathrm{m}^{-1}$. Casper et al. [8] studied the breakdown using pressure sensors, and observed that breakdown is initiated in the center of the wave packet where amplitudes are the largest.

Zhu et al. [53] experimental study using PCB transducers in the Mach 6 quiet wind tunnel at the Peking university showed that low frequency structures had significant amplitude during the breakdown of hypersonic boundary layer. Fig. 2.5 shows that the second mode initially grows in amplitude and then decays downstream whereas the low frequency waves continues to grow, the transition onset location is x/L≈0.78 from optical measurements. This trend was also observed for varying Reynolds number as shown in the fluctuating pressure amplitude plots in Fig. 2.6. Zhu et al. [53] then proceeded to analyze the PCB signals using bispectral analysis, to determine the non-linear interactions that occur in a given signal. The bispectral analysis takes a signal and decomposes it in two frequency axes. The peaks that occur in a bispectrum indicate that the frequencies corresponding to a peak interact with each other and exchange energy. From Fig. 2.7 it is seen that there are strong peaks that occur at the second mode fundamental frequency (240 kHz) and low frequency wave (<100 kHz) , indicating an interaction between these waves. The interaction is stronger at x/L= 0.69 compared to x/L=0.54, and eventually dies as the second mode waves decay at x/L=0.84. The velocity of the low frequency waves were also found to be equal to the second mode propagation speed. The two results, the bispectrum peaks and the equal velocities indicate a phase locked mechanism, in which waves with equal velocities interact and exchange energies. Zhu et al. [53] concluded that the second mode wave initially grows and interacts with the low frequency waves via a phase locked mechanism and transfers it's energy and then decays. After interaction the low frequency waves continue to grow in amplitude and the second mode waves decay; hence concluding that the low frequency waves eventually drive the boundary layer to turbulence and not the Mack modes.

The most common signal processing technique used to analyze the measured signals is the Fourier transform, as discussed in the preceding paragraphs. In this thesis the wavelet analysis will be used to study the development of the second mode waves. The wavelet transform has been used by Grossir et al. [14], Wagner et al. [51] to analyze the signals from surface sensors. Fig. 2.8 shows the wavelet transform of a pressure signal at two stream wise positions on a cone. If the Fourier transform of the signal was taken, a result similar to Fig. 2.1b would be generated. In doing so the information of when the second mode passes over the sensor is lost, where as in Fig. 2.8b the second mode passes over the sensor at the time instant corresponding to appearance of large wavelet coefficients around 200 kHz. As seen in Fig. 2.8a there is no large wavelet coefficient implying no second mode waves pass over this sensor. For the downstream sensor Fig. 2.8b there are second mode waves as well as its harmonics that develop.

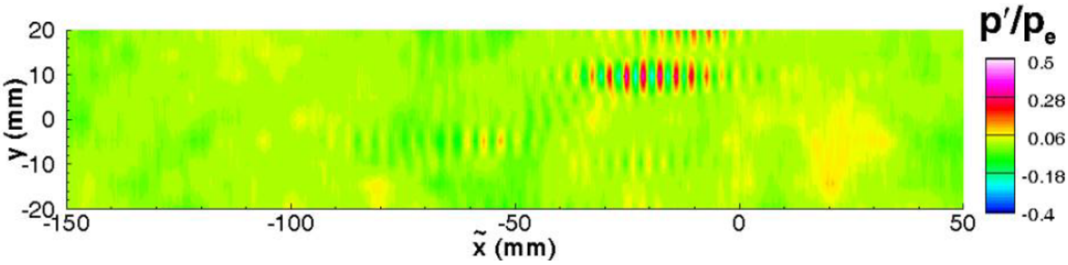

Figure 2.2: Pressure contour of span wise PCB transducers, showing the circumferential extent of the wave packet to be 4δ [7]. $\tilde{x}$-stream wise distance and y- span wise distance.

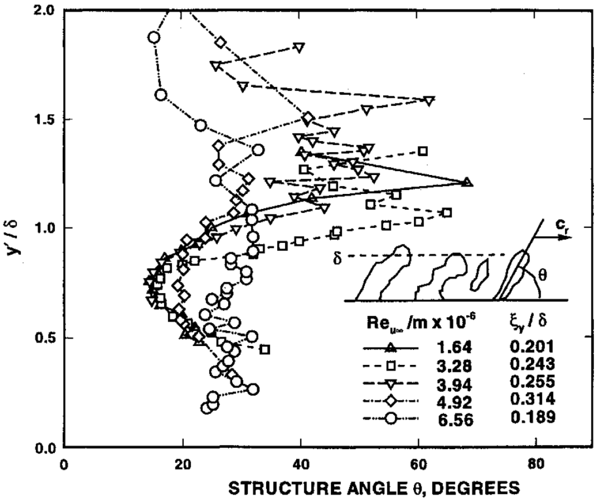

(a) second mode structure angle measured by Kimmel et al. [18].

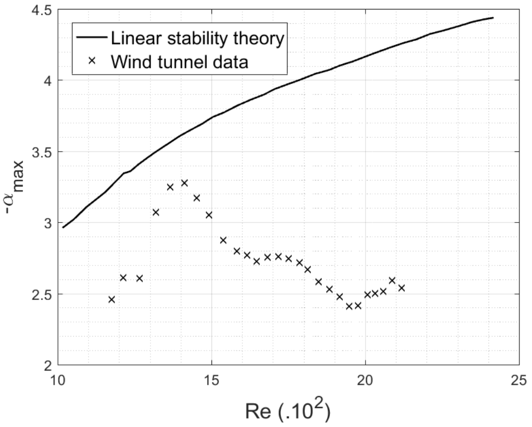

(b) Maximum second mode growth rate vs Reynolds number, adapted from Stetson and Kimmel [47].

Figure 2.3: Hot wire results from Kimmel et al. [18] and Stetson and Kimmel [47].

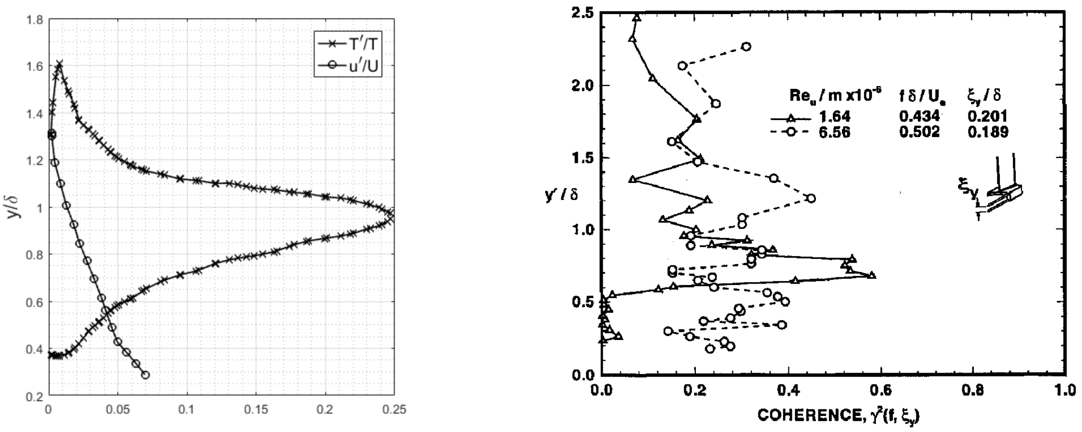

(a) Adapted from Demetriades [10], shows that the second mode causes more variation in density than velocity.

(b) For low Reynolds number waves concentrated at $y/\delta=1$ [18].

Figure 2.4: Results showing the second mode wave concentrated at the boundary layer edge.

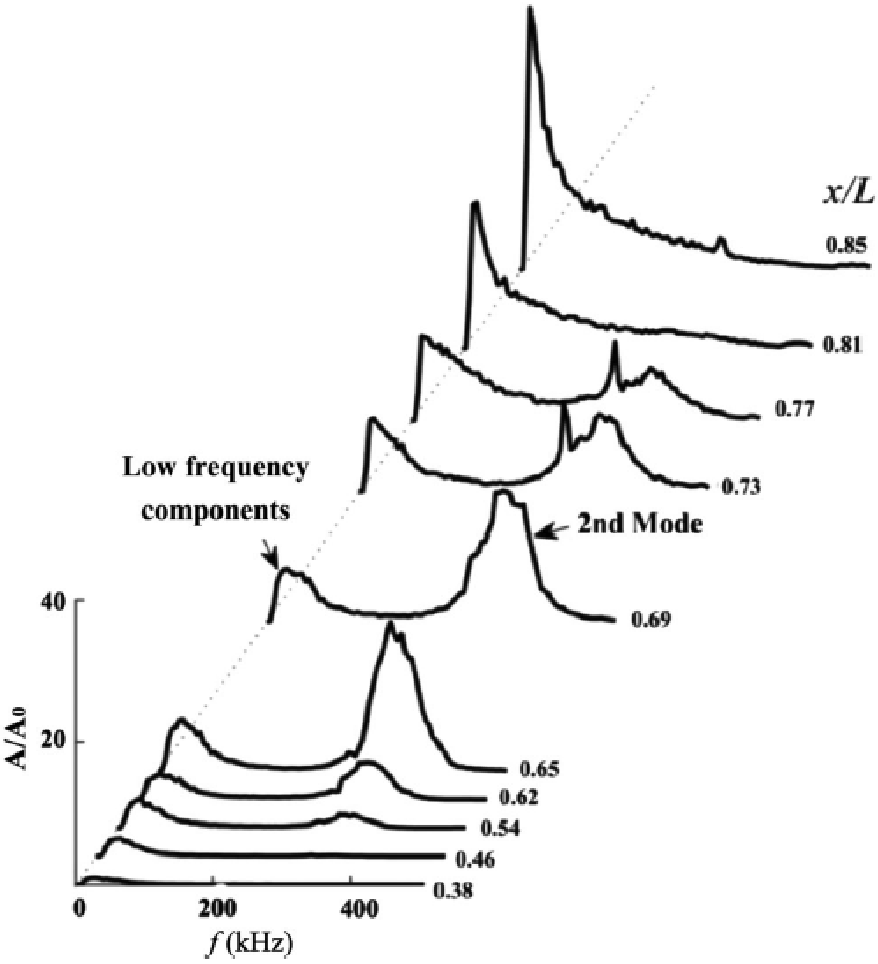

Figure 2.5: Frequency spectrum at different stream wise positions[53].

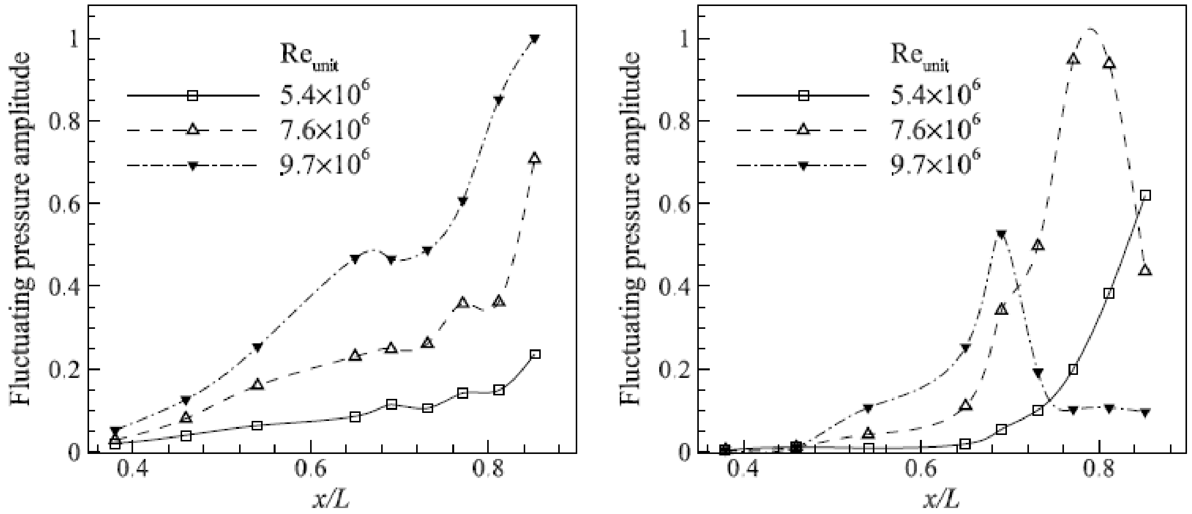

Figure 2.6: Fluctuating pressure amplitude for (left) low frequency waves and (right) second mode wave [53].

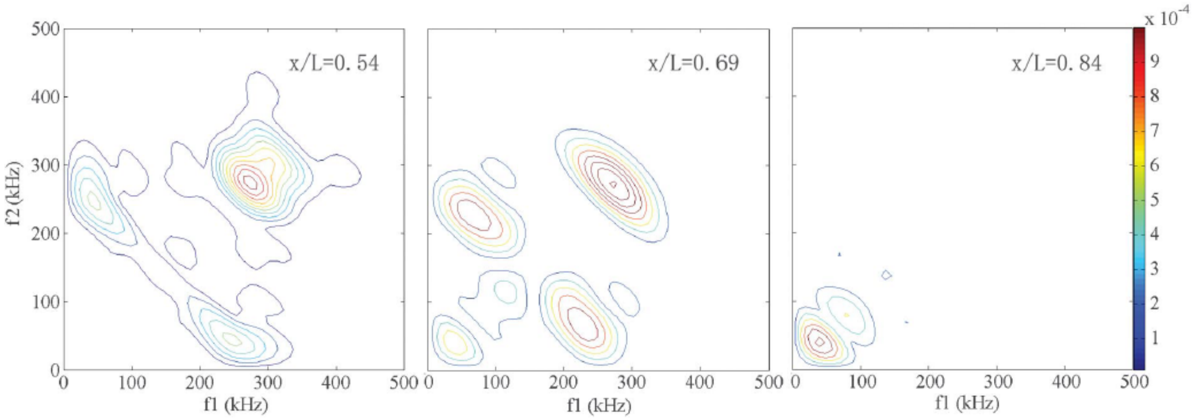

Figure 2.7: Fluctuating pressure amplitude for (left) low frequency waves and (right) second mode wave [53].

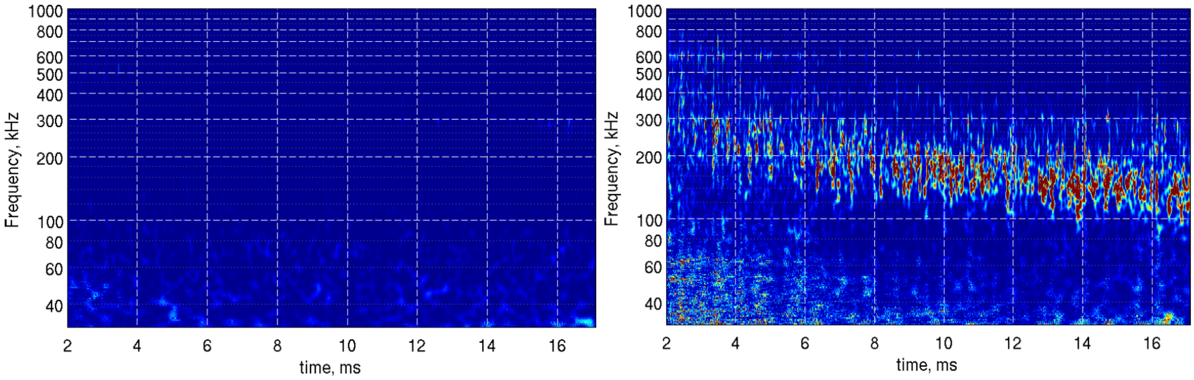

(a) PCB at x= 490 mm.

(b) PCB at x= 710 mm.

Figure 2.8: Wavelet transform of PCB signals [14].

2.2. Results from visualization based techniques

Visualization techniques have gained popularity recently to study the second mode instability. These techniques are non-intrusive unlike hot wire anemometers and can also be used in high enthalpy conditions where hot wires can be damaged. Visualization techniques can also take measurements in the wall normal directions, where surface based techniques like PCB and heat flux sensors cannot. Potter and Whitfield [36] were the first to observe rope-like structures in schlieren images of a hypersonic boundary layer which were later identified as the second mode waves by Smith [43].

Three optical based techniques: schlieren, deflectometry and focused laser differential interferometry (FLDI) have been used to study the Mack modes. In schlieren deflectometry the basic principles are the same, the only difference being that in the image plane, photo detectors are placed at a specific position. These detectors have a higher bandwidth in comparison to schlieren visualization [23]. Focused laser differential interferometry (FLDI), was implemented by Parziale et al. [33]. FLDI detects the change in phase due to variation in density of two spatially separated points. This makes the interferometer sensitive to spatial density differences in the stream wise direction [33].

Laurence et al. [22], demonstrated that image processing techniques can be applied to schlieren images, to obtain the wavelength and velocity of the second mode waves. To find the wavelength, the power spectral density of the pixel intensity of a row from the schlieren image is taken (see Fig. 2.12). Two dimensional image cross correlation was applied to consecutive images (see Fig 2.9) to find the velocity of the waves [22–24]. The velocity of the disturbances was found to be $0.8U_e$, once again confirming the theoretical prediction of Mack and the results of surface mounted sensors presented in sections 1.1.1 and 2.1. Grossir et al. [15] also visualized the rope like structures in schlieren images of a hypersonic cone boundary layer, and his results agree well with the theoretical results. The FLDI investigations of Parziale et al. [33, 34, 35] also found the second mode wave propagation speed to be equal to the free stream velocity.

Laurence et al. [24, 25], studied the second mode wave growth and breakdown in a hypersonic cone boundary layer using high speed schlieren visualization. Fig. 2.10a shows the frequency spectra developing over time, the Fourier transform of the maximum amplitude row was selected for the plots. In Fig 2.10a second mode wave packets are not seen all through out the test time, evident from the peaks that occur at 300 kHz at various time instants. VanDercreek et al. [49], attributes this intermittent appearance of the Mack mode to the vibration of the cone model which changes the free stream conditions. In Fig 2.10b, the spectra is spread over a wide range of frequencies indicating a transitional or turbulent boundary layer for this condition. The result of Fig 2.10b, is similar to Fig. 2.1b (Re=6.85,8.5 $\cdot 10^4$ cm^{-1}) which shows the energy being distributed among all frequencies. Using the images it was also possible to generate a spatial mean power spectra, Fig. 2.11a. Second mode peak is seen upstream between 725 -740 mm. Fig. 2.11a shows that as the wave packet travels downstream the frequency decreases (due to boundary layer growth), this was also reported by Stetson et al. [48] and discussed in section 2.1.

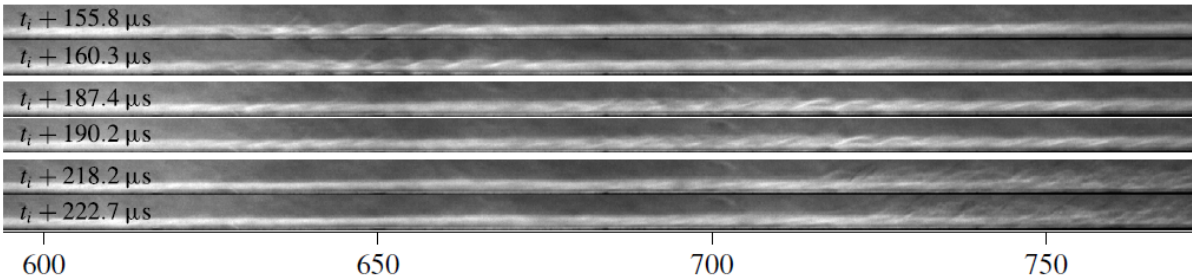

Figure 2.9: Consecutive schlieren images showing the second mode disturbance developing and breaking into turbulence[25].

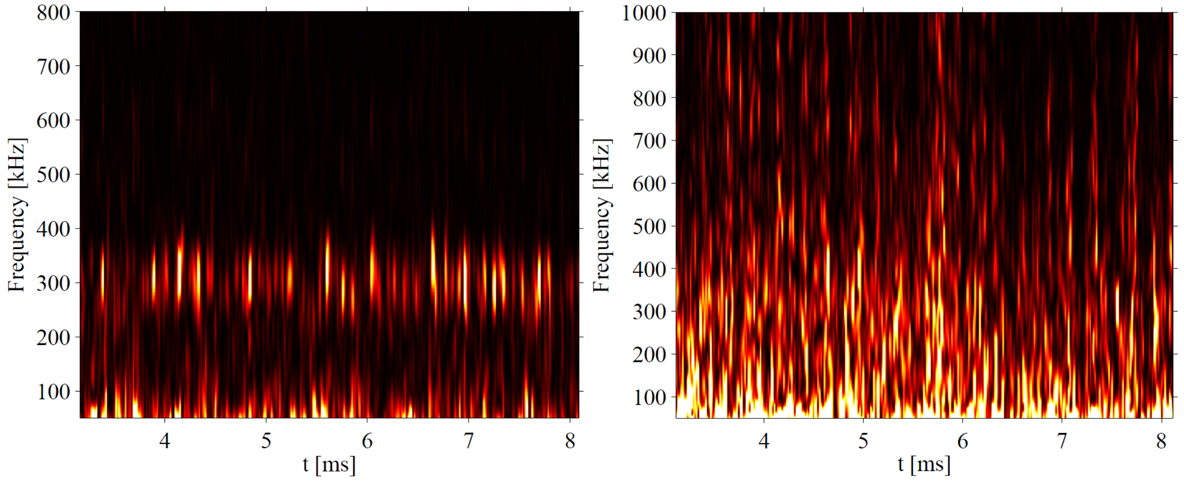

(a) Re = 2.6 $\cdot 10^6$ m^{-1}, beginning of visualization window.

(b) Re = 4 $\cdot 10^6$ m^{-1}, ending of visualization window.

Figure 2.10: Time developing power spectra at a fixed stream wise location and height above the surface for consecutive images, for a laminar and turbulent boundary layer [24].

Following Kimmel's study of the structure angle [18], Laurence also studied the variation of structure angle of the wave packets in the wall normal direction from schlieren images, by cross correlating vertically separated image rows. Laurence found the structure angle to be 70-80° at y/δ=0 decreases to 12-13° at y/δ=0.7 and finally increases to 100° at the boundary layer edge (Fig. 2.11b). By band pass filtering the row signals around the first harmonic frequency, the structure angle of the harmonic was also found in Ref [25]. Parziale et al. [35] found the structure angle to be 11-15° using schlieren images, although the distribution along the wall normal direction is not provided in the study.

Some unique features of the second mode disturbances could be investigated using schlieren images. The distribution of the wall normal energy by taking fast Fourier transforms of each image row is shown in Fig. 2.12. Laurence et al. [25] observed that, the distribution of the wall normal energy varied during the development of wave packets. In particular it was noted that there were two peaks present, one close to the boundary layer edge (as reported by hot wire measurements) and the other close to the cone surface (Fig. 2.12a). Laurence et al. [25] noted that as the wave packet developed there was a development of a third peak in the wall normal direction before breakdown occurs (Fig. 2.12b). By bandpass filtering an image separately around the second mode fundamental frequency and the first harmonic frequency, and comparing the images, Laurence et al. [25] found the harmonic energy to be concentrated at the center of a wave packet (see Fig. 2.13). Casper et al. [8] observed that the wave packet breakdown is initiated at the center of the wave packet. These two observations may be an indication of the role of harmonics play in the breakdown process. By applying the wavelet transform to schlieren images, it will be possible to study point of initial breakdown inside a wave package and the growth of harmonics; hence establishing a link between the observations of Casper et al. [8] and Laurence et al. [25]. Hofferth et al. [16] performed bispectral analysis on focused schlieren deflectometry signals from a hypersonic flared cone boundary layer, and found that there was interaction between the fundamental second mode wave and it's first harmonic.

The amplification factor of the second mode instability wave was computed using schlieren deflectometry [23, 49] and FLDI [34]. Laurence et al. [23] used schlieren deflectometry to measure the growth rates shown in Fig. 2.14, the figure provides only normalized values and not the absolute values. The highest amplification rate occurs for the wave having a frequency of 400 kHz which corresponds to the fundamental second mode frequency. There is also significant amplification for lower frequencies below 100 kHz, although the author does not discuss the implications of this result, in light of the study conducted by Zhu et al. [53] (discussed in section 2.1) these can be the amplified low frequency waves which drive the boundary layer to turbulence. Parziale et al. [34] found the maximum growth rates of the waves to be 5.4 - 9.8 m^{-1}, for Mach number 5 and unit Reynolds number of 2$\cdot 10^6$ m^{-1} and enthalpy of 9.02 MJ/kg. The growth rates have not been computed from schlieren images yet, and if successful it can shed more light into the waves which drive the boundary layer to turbulence; hence it is one of the objectives of this work.

Shumway and Laurence [38] used methods like wavelet analysis and auto-correlation to identify the second mode wave in a schlieren image. Casper et al. [6] used schlieren images to detect the intermittency of the boundary layer. Casper et al. [6] used an edge detection algorithm to determine intermittency, if the edges detected were larger than laminar boundary layer height it was defined turbulent and given value 1, and if less than it was defined laminar and given 0.

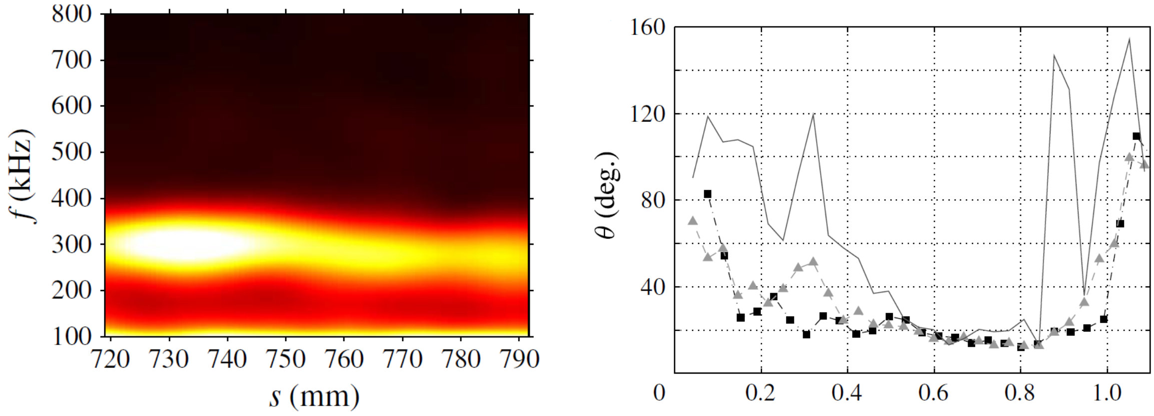

(a) Spatially developing mean power spectra, Laurence et al. [25].

(b) Variation of structure angle in the wall normal direction, Laurence et al. [25].

Figure 2.11: Different analysis performed on the schlieren images[25].

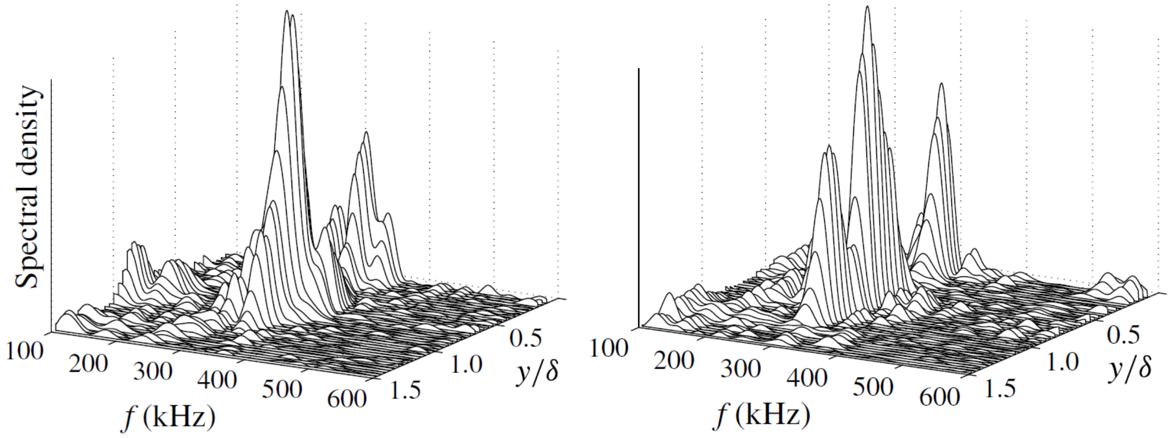

(a) Double peak distribution observed during early stages of wave packet development.

(b) Three peak distribution observed during later stages of wave packet development.

Figure 2.12: Variation in wall normal energy distribution [25].

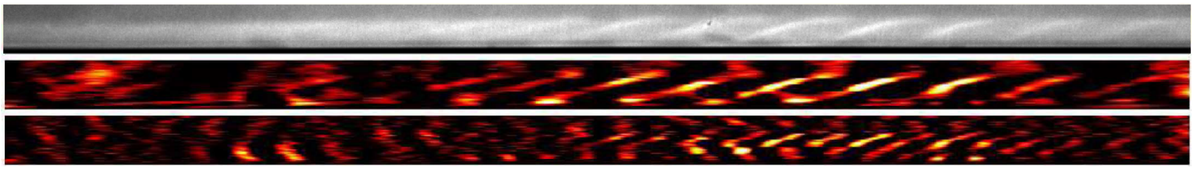

Figure 2.13: (top) Schlieren image, (middle) schlieren image band pass filtered about the second mode fundamental frequency and (bottom) band pass filtered about the first harmonic, Laurence et al. [25].

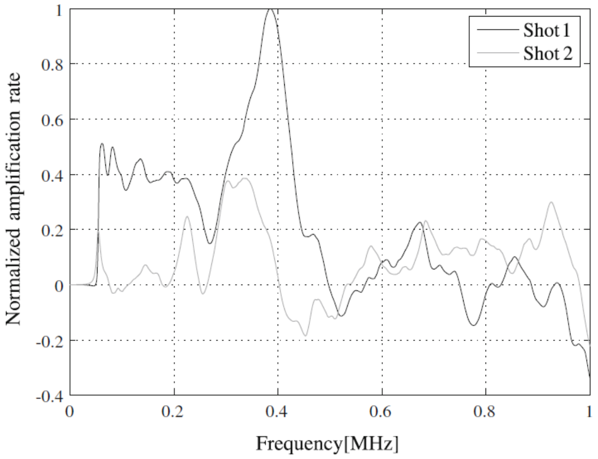

Figure 2.14: Amplification factor obtained from deflectometry [23].

2.3. Investigations using numerical simulations

Numerical simulations of hypersonic boundary layer were also performed over the years to get a more detailed picture of the instability growth. The results discussed in this section are direct numerical simulations (DNS) results. DNS uses the exact Navier-Stokes equation and does not perform any turbulence modeling either. However discretization errors can occur because the grid sizes have to be small enough to capture all the small scale (Kolmogorov scale) structures of turbulence. Hence the results from these simulations have to be validated through experimental investigations. In this section a review of the results from direct numerical simulations (DNS) investigating second mode instability growth are presented.

The simulations conducted by researchers were performed on a hypersonic cone boundary layer, conditions which are conducive to the growth of the second mode waves [29, 30]. Disturbances over a broad spectrum of frequencies are introduced into the boundary layer close to the nose tip, and it was observed that only the second mode waves were amplified after a certain distance from the disturbance source [39].

Sivasubramanian and Fasel [39, 40, 41] and Sivasubramanian et al. [42] found three breakdown mechanisms to be relevant for a hypersonic cone boundary layer. The three mechanisms are 1) fundamental resonance mechanism, 2) subharmonic resonance mechanism and 3) oblique wave breakdown mechanism. In the fundamental resonance mechanism, there is an interaction between a primary wave and two oblique waves with the same frequency. For the subharmonic resonance there is interaction between a primary wave and two oblique secondary waves at half the frequency of the primary wave. Finally in the oblique breakdown mechanism two oblique waves of opposite angles interact with each other causing breakdown. The primary and secondary waves interact via a phase locked resonance mechanism. In phase locked resonance a planar wave and pair of oblique waves with any frequency but same phase velocity interact to generate new oblique waves. Resonance among the planar, oblique and newly generated wave leads to rapid growth of obliques waves and eventually transition to turbulence. In the paragraphs that follow a summary of the numerical results supporting the above breakdown mechanisms are discussed. The frequency spectra for the linear wave packet (Fig. 2.15a) shows that wave is two dimensional since most of the energy is concentrated at the azimuthal mode number, k equal to zero. This is again in agreement with previous experimental and theoretical investigations discussed in previous sections. There is also energy contained in oblique waves at lower frequencies in Fig. 2.15a, this is the first mode wave which is also present in the wave packet, as the theory predicts the amplification of the first mode wave is small in comparison with the second mode (Fig. 1.2). In contrast to the linear wave packet, the frequency distribution for the non-linear wave packet exhibits strong three dimensional characteristics, from the energy concentrated in non-zero mode numbers in Fig. 2.15b.

Fig. 2.15b shows the disturbance spectrum for a non-linear wave packet. As mentioned previously, fundamental resonance is the interaction between a primary wave and two oblique waves with the same frequency. Fig. 2.15b shows the disturbance spectrum for a non-linear wave packet, and the dominant frequencies in the spectrum indicate the possible interactions that occur. The fundamental resonance is seen in Fig. 2.15b (solid red circles), the oblique waves have a frequency of 210 KHz similar to the primary wave (black region) and azimuthal mode number (k_c) of 150. The dotted blue circles in Fig. 2.15b indicate the subharmonic

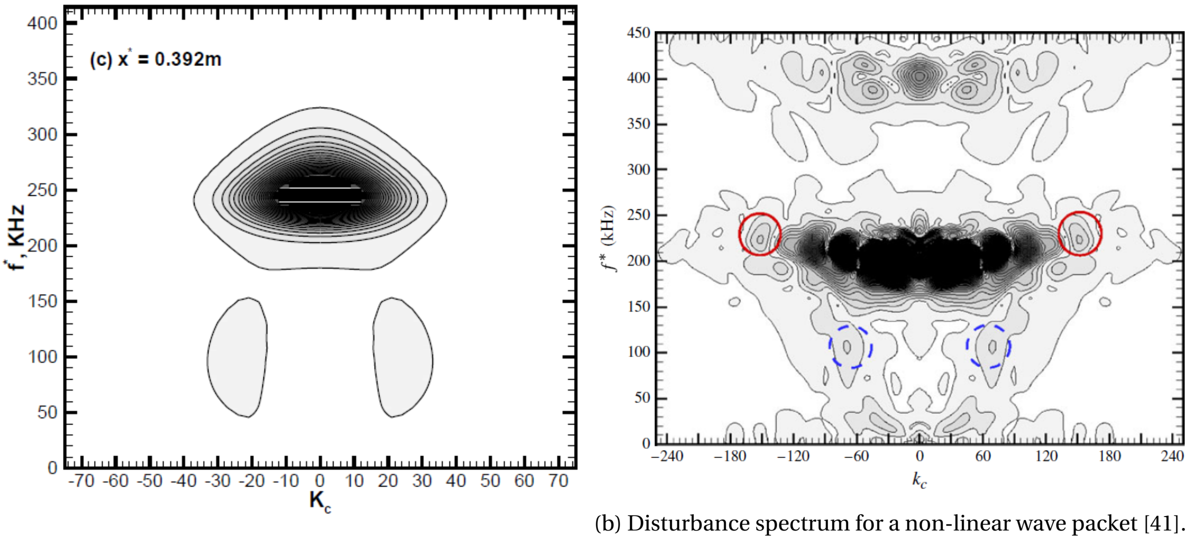

(a) Disturbance spectrum for a linear wave packet [39].

(b) Disturbance spectrum for a non-linear wave packet [41].

Figure 2.15: Disturbance spectrum for wave packets, K_c is the azimuthal mode number.

resonance, in which interaction occurs between the primary wave and secondary waves at frequencies half of the primary wave. Sivasubramanian and Fasel [40] observed that the growth rate of the disturbances was larger for fundamental resonance mechanism and concluded that the fundamental resonance mechanism was stronger than subharmonic resonance for a hypersonic cone boundary layer. Experimental verification of subharmonic resonance has been reported by Kimmel and Poggie [19], Lachowicz et al. [21]. Fundamental resonance has not yet been verified experimentally. Harmonics are also seen in Fig. 2.15b, similar to the experimental observations discussed in sections 2.1 - 2.2.

Fig. 2.16 shows the pressure amplitude for a wave packet. From the figure it is seen that higher pressure amplitudes occur in the leading edge of the wave packet. From Fig. 2.16, it is concluded that the maximum amplitude of a linear wave packet is concentrated at the leading edge, contrary to the experimental observations of Casper et al. [8] who found the maximum amplitude to be at the center of the wave packet. Casper et al. [8], observed the wave amplitudes to be at center close to breakdown, therefore it can be possible that the waves were non-linear before breakdown occurred. The two results suggest that during the initial stages wave packet development (linear) the energy is concentrated at the leading edge, after sufficient growth non-linear process redistribute the energy to the center of the wave packet. Fig. 2.17 adapted from Casper et al. [7] shows that there are wave packets that agree with the numerical observation of Sivasubramanian et al. [42].

Fig. 2.18a shows the spatial frequency distribution, here the decrease in second mode frequency due to boundary layer growth is seen, this is similar to Fig. 2.11a obtained using schlieren visualization. In the upstream portion of Fig. 2.18b the waves are concentrated at the boundary layer edge and during breakdown it spreads vertically. This characteristic is seen in Fig. 2.4b from the study performed by Kimmel et al. [18], where for lower Reynolds number the waves are concentrated at the boundary layer edge and for higher Reynolds number the waves are spread in the boundary layer. Sivasubramanian and Fasel [39] observed that the wave packets stretch in the stream wise direction as it travels. Sivasubramanian and Fasel [39], attributed the stretching to the differential velocity between the leading and trailing edges of the wave packet (leading edge has higher velocity). This is also seen in schlieren images shown in Fig. 2.14. The differential velocity between the leading and trailing edges can be measured by cross-correlating the separate sections of the wave packet between images. It was also observed that as the wave packet travels downstream, it becomes more three dimensional (wave angle larger than 0°) this was also observed using hot wire [18] and PCB transducers[6], discussed in section 2.1.

The investigations of Li et al. [26] provide results which are in contrast to the simulations discussed in the paragraphs above. Li et al. [26] observed low frequency waves to be prominent prior to breakdown of the boundary layer. Li et al. [26] observed that the low frequency waves are amplified and rapidly distorted, which indicated that they play a vital role to initiate transition. It was also concluded that the second mode waves trigger the growth of these low frequency structures, these waves were also observed experimentally by Zhu et al. [53] as discussed in section 2.1.

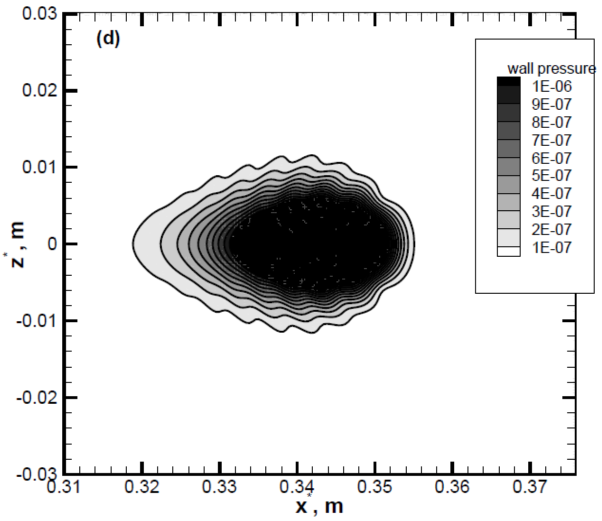

Figure 2.16: Wall pressure contours for a linear wave packet, x^* stream wise direction and z^*-span wise direction [42].

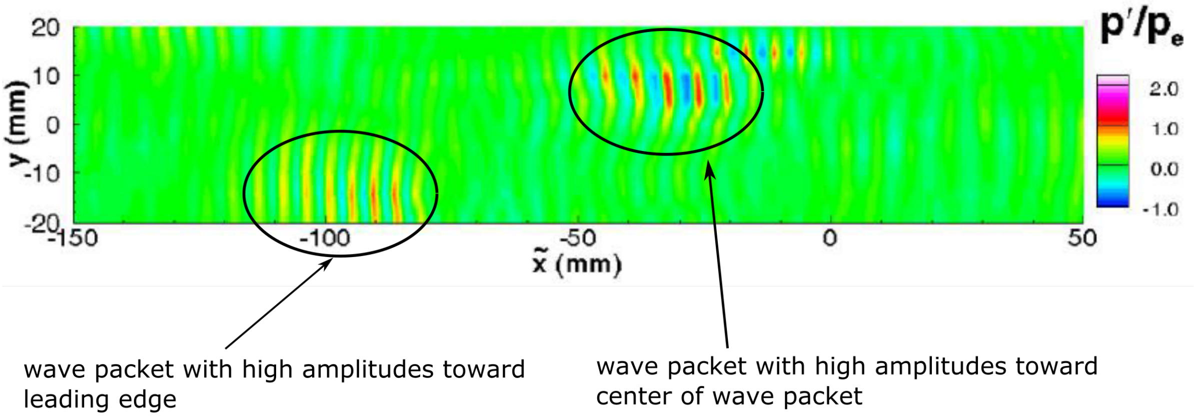

wave packet with high amplitudes toward leading edge

wave packet with high amplitudes toward center of wave packet

Figure 2.17: Pressure contour of span wise PCB transducers showing two wave packets, one with amplitude concentrated at the leading edge and the other at the center, adapted from Casper et al. [7].

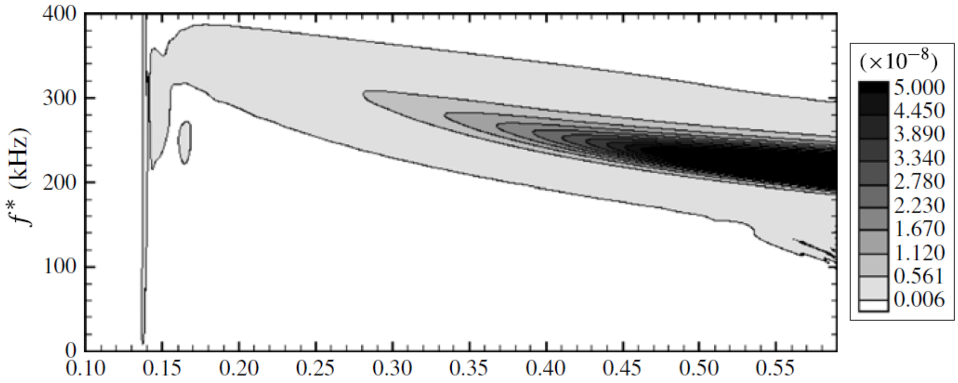

(a) Stream wise frequency of second mode wave [42].

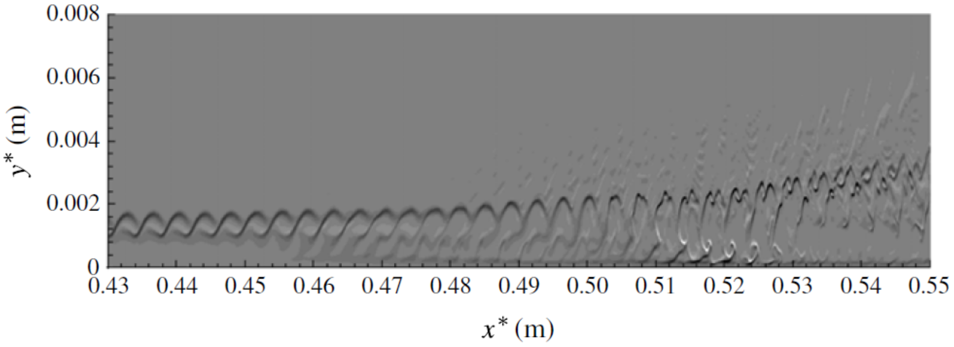

(b) Wall normal density contour from numerical simulation showing acoustic wave radiation and second mode breakdown [41].

Figure 2.18: Results from numerical simulation of hypersonic cone boundary layer.

Author	Mach	Re(m^{-1})	Enthalpy (J/kg)	$(\alpha_i)_{max}$ (m^{-1})
Roediger et al. [37]	5.8	$4.29 \cdot 10^6$	$429 \cdot 10^3$	25
Estorf et al. [12]	5.8	$9.17 \cdot 10^6$	$417 \cdot 10^3$	36.7
Estorf et al. [12]	5.8	$1.5 \cdot 10^6$	$417 \cdot 10^3$	6
Parziale et al. [34]	5.8	$2 \cdot 10^6$	$9.02 \cdot 10^6$	5.4 - 9.8
Wagner [50]	7.3	$1.5 \cdot 10^6$	$3.25 \cdot 10^6$	11-13

Table 2.1: Maximum second mode growth rates reported in literature.

2.4. Summary

In this chapter a review of the experimental and numerical investigations undertaken to study the development of second mode waves were presented. The discussion can be summarized into the following points:

1. The experimental studies on hypersonic boundary layers confirmed the following theoretical predictions of Mack [27]:1) The second mode waves were the most dominant instability, and the most unstable wave angle was 0°, 2) wave propagation speed is 0.9 U_∞[18] and 3) wavelength is approximately twice boundary layer thickness [10, 48].

2. The second mode waves cause density fluctuations primarily and are concentrated towards the boundary layer edge. This was reported in hot wire measurements [10, 18], schlieren visualization [23, 25] and direct numerical simulations [39]. The fluctuations in velocity are negligible in comparison to the density fluctuations (see Fig. 2.4a).

3. As the second mode propagates downstream, the frequency of the waves reduce due to increase in the thickness of the boundary layer. This was termed as the "tuning effect" of the boundary layer by Stetson et al. [48]. This is seen in Figures 2.1b, 2.11a and 2.18a.

4. The second mode wave packet has limited span wise extent, which means it does not cover the entire circumference of the cone. The circumferential extent was found to be 4δ by researcher using PCB transducer and hot wire anemometer [7, 18]. In numerical studies of Sivasubramanian and Fasel [39] it was found that as the wave packet travels it becomes less two dimensional (wave angle non zero), this can affect the schlieren results as the technique averages across the line of sight.

5. Harmonics of the fundamental mode were observed in a significant number of studies (experimental and numerical). The harmonics were not predicted by the linear theory and their presence indicated that non-linear mechanisms are present in the boundary layer which generate these harmonic waves.

6. Stetson [48] observed that a property of transition is the decrease in the growth rates of the second mode waves and an increase of the first mode growth rates [48]. Zhu et al. [53] also makes a similar observation but does not identify the low frequency waves as first mode waves. The low frequency structures observed by Zhu et al. [53] have not been reported in optical investigations although a closer look into Fig. 2.12a shows energy contained at lower frequencies and Fig. 2.14 showed significant amplification in the low frequency ranges. These could be an indication of low frequency waves captured in schlieren images. If these waves (second mode, harmonic and low frequency waves) are captured in schlieren images computing their amplification factor can help verify the observations of Stetson et al. [48] and Zhu et al. [53].

7. The investigations of Sivasubramanian and Fasel [41] concluded that the fundamental resonance mechanism is the strongest in a hypersonic cone boundary layer. Since the mechanism involves interaction with oblique waves and schlieren visualization averages across the line of sight, experimental verification of this breakdown mechanism is beyond the scope of this study. If waves cover the entire circumference of the cone, i.e. they do not have a limited circumferential extent; then it can be detected by schlieren visualization. Span wise probes will have to be used to study and verify the breakdown mechanisms.

8. Sivasubramanian et al. [42] observed the wave packet energy to be concentrated at the leading edge of a wave packet, whereas Casper et al. [8] observed the energy to be concentrated at the center of the wave packet before breakdown; indicating a redistribution of energy due to non linear processes. The wavelet analysis can be used to study stream wise energy distribution of the wave packet at various stages and confirm these observations. Laurence et al. [25] reported a variation in the distribution of the wall normal energy, by applying the wavelet analysis to schlieren images this variation can also be studied.

9. The growth rates of the second mode waves have been extracted using surface mounted sensors and schlieren deflectometry. The maximum growth rates reported in literature are summarized in table 2.1.

2.5. Research proposal based on the literature reviewed

As stated in section 1.3, the objective of the thesis is to study the development of second mode waves by applying wavelet transform to schlieren images. Based on the literature reviewed in this chapter a link is established between the present study and published material through the following points:

- Can harmonics of the fundamental wave be detected?

  Harmonic waves have been observed in schlieren images [23, 25]. Applying the wavelet transform will allow to compare the spatial location of the harmonics with respect to the fundamental wave. The amplitude distribution of the waves can also be compared.

- Can the amplification factor of the waves be determined?

  Second mode growth rates have been extracted using surface mounted sensors primarily. Using these sensors the temporal amplification factor can be determined. Using schlieren images in conjunction with wavelet transform, the spatial growth rates can be determined. This will allow to study the growth of different portions of the wave packet like the leading/trailing edge or the core of the wave packet.

- How does the second mode wave breakdown process start?

Stetson and Kimmel [47] predicts that during transition the harmonics of the fundamental second mode wave should amplify. A recent study by Zhu et al. [53] proposes that it is low frequency waves that cause transition after interaction with the second mode waves. These observations can be tested by taking the wavelet transform of schlieren images capturing transition.

2.5.1. Research question

The research question has been formulated based on the objectives outlined in section 1.3 and literature reviewed in this chapter. The main research question is further divided into sub-questions, which will together answer the principal research question. The research question and it's sub-questions are:

What properties of the second mode wave can be studied by applying the wavelet transform to schlieren images of a hypersonic boundary layer?

- Can the amplitude distribution of the second mode wave in the wall normal and stream wise direction be studied?
- Can harmonics of the fundamental frequency be detected as the instability grows?
- Can the amplification rate of wave be determined?
- How does the second mode wave breakdown process start?

3

Methodology

In this chapter the method followed to study the growth of the second mode waves is discussed. First the experiments performed in HEG are explained in section 3.1 followed by a discussion on the wavelet transform in section 3.2, which is the primary signal processing technique employed to study the waves captured in the schlieren images.

3.1. Experiments

Experiments were performed in the high enthalpy shock tunnel in Goettingen (HEG). HEG is a reflected shock tunnel which uses a free piston to compress the driver gas. HEG was designed to simulate hypervelocity flow conditions at Mach 7, both the velocity and the high temperature effects. The facility is capable of generating test gas of stagnation pressure of 200 MPa and stagnation enthalpies up to 25 MJ/kg [11]. A disadvantage of impulse facilities like the HEG is the short test time. Typical test time in the HEG is about 3 ms.

The free piston compresses the driver gas in the compression tube adiabatically to high pressures which causes the main diaphragm to rupture. Rupturing of the main diaphragm causes a primary shock to travel through the driven section (shock tube in Fig. 3.1) compressing the test gas. The primary shock travels to the end of the shock tube (upstream of the nozzle) where it is reflected from a secondary thin diaphragm. The test gas which has now been compressed by the primary and reflected shock, is expanded through the nozzle to hypersonic test conditions.

The experiments were performed on a 7° half angle cone with a length of 1.1 m and variable nose radii of 2.5 and 0.1 mm, see Fig. 3.3. The cone geometry develops an axi symmetric boundary layer with no pressure gradient, conditions which are conducive to second mode development [27, 29]. The second mode waves cause density fluctuations primarily. Density fluctuations also cause variations in the refractive index of the medium, and hence these waves can be visualized by techniques which depend on the gradients of refractive index like the schlieren visualization.

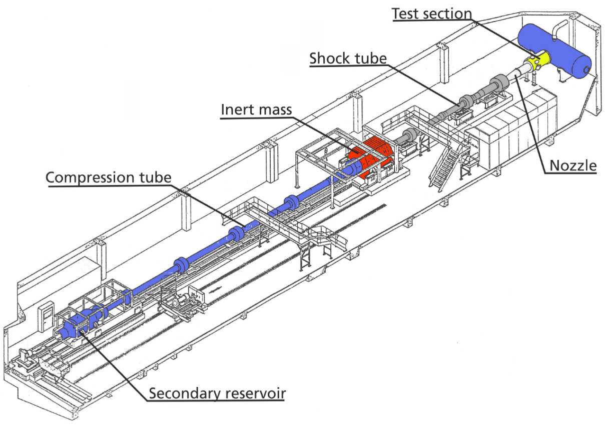

Figure 3.1: Different components of HEG [24].

3.1.1. Basics of schlieren visualization

There are various density gradients that are encountered in a flow, like flow past a shock wave or within the boundary layer. In the boundary layer density gradients are created by the friction between shear layers which generate heat and hence reduce the density ($\rho = (p/RT)$, pressure remains the same in the boundary layer). The second mode waves as introduced in the previous chapters travel through reflection of compression and expansion waves (see section 1.1.1 and Fig. 1.3), which also cause density fluctuations. Density fluctuations cause variations in the refractive index of the media, given by equation 3.1, where n is the refractive index and K is the Gladstone-Dale coefficient.

$$n - 1 = K\rho \tag{3.1}$$

The variations in the refractive index causes the light to bend as it passes through the regions of density gradients. The light bends towards a region of higher refractive index or in this case higher density. These bent rays are either blocked or passed by a knife edge resulting in either a dark or bright region in the image corresponding to the location of the density gradient. This is explained better with an example. Consider an experiment to visualize the boundary layer that develops on a cone. The schlieren setup uses a horizontal knife edge and, the density within the boundary layer will be lower than the free stream density. As the light passes through the boundary layer on the upper surface of the cone, it is bent upwards due to density gradient and passes through the horizontal knife edge resulting in a brighter region. The opposite happens on the lower surface, the light is bent downwards, towards the knife edge and gets blocked by it resulting in a dark region on the schlieren image, see Fig. 3.2. As discussed in section 1.1.1 the second mode travels by reflecting compression and expansion waves which cause density gradients. Hence the second mode waves appear as alternate dark and bright regions.

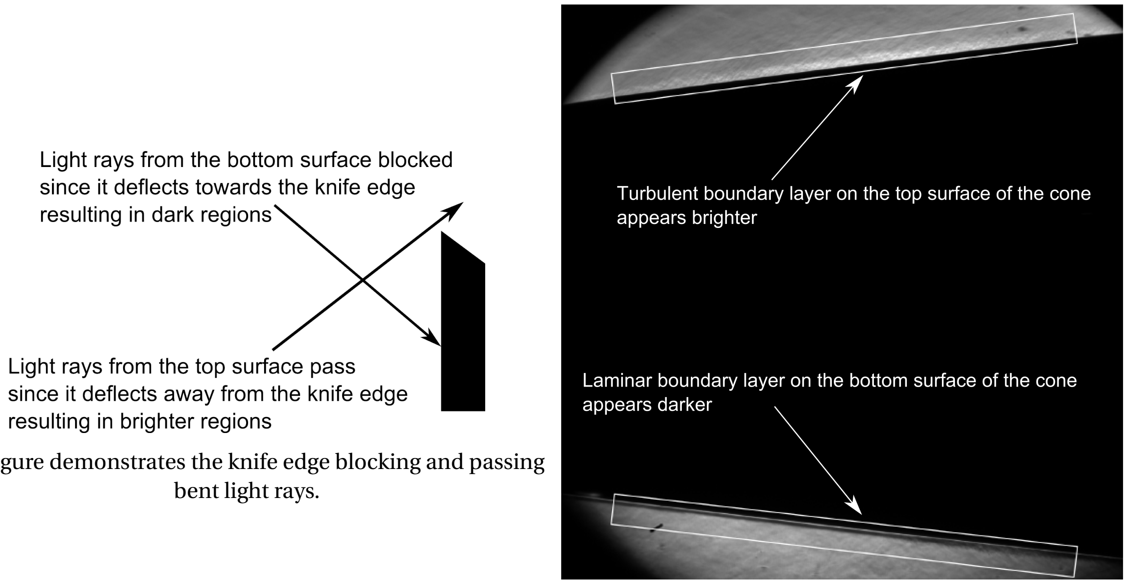

(a) Figure demonstrates the knife edge blocking and passing bent light rays.

(b) Boundary layer on the top and bottom surface of a cone, adapted from Wagner [50].

Figure 3.2: Schlieren visualization.

3.1.2. Schlieren experimental setup

A conventional Z-fold schlieren setup was employed in the experiments, shown in Fig. 3.4a . Two spherical mirrors with 1.5 m focal length was used to focus the light beam to the test section and to refocus it to the camera. A horizontal knife edge was used in the setup which implies density gradients in the wall normal direction are measured. A Phantom v1210 camera was employed at a frequency of 175 kHz, exposure time of 4 μs and a resolution of 1280 × 45 pixels. Cavilux smart visualization laser was used to provide a monochromatic and incoherent source of light with a wavelength of 640 nm. The pulse length of the laser was set to 20 ns in order to avoid motion blur as the exposure time of the camera was too high to freeze the instability wave.

HEG Run number	Nose radius (mm)	M_∞	Re_m ($\cdot 10^6\,m^{-1}$)	h_0 (MJ/kg)	U_∞ (m/s)	Window (mm)
1443	2.5	7.29	2.23	3.48	2500	572.47-737.59
1440	2.5	7.3	2.23	3.48	2486	576.97-766.05
1447	2.5	7.36	4.09	3.26	2432	519.23-659.35
1308	2.5	7.3	2.41	3.48	2480	697-812
1438	0.1	7.3	2.24	3.4	2481	619.51-757.55
1439	0.1	7.3	2.24	3.37	2480	572.47-737.59

Table 3.1: Flow conditions of the schlieren images to be analyzed. M_∞-Mach number, Re-Reynolds number, h_0-total enthalpy and U_∞-free stream velocity

In the experiments a pulsed light source was used instead of a continuous light source. When a continuous light source is employed, the frequency is limited by the camera frame rate and the exposure time of the camera may not be sufficient to freeze the motion of the wave. To overcome these limitations a short duration pulsed light source is used. The two pulses are fired such that each pulse catches a different exposure window, similar to the setting shown in Fig. 3.4b. The exposure time is now reduced to the pulse length of the light source which is 20 ns, sufficient to freeze the motion of the second mode waves.

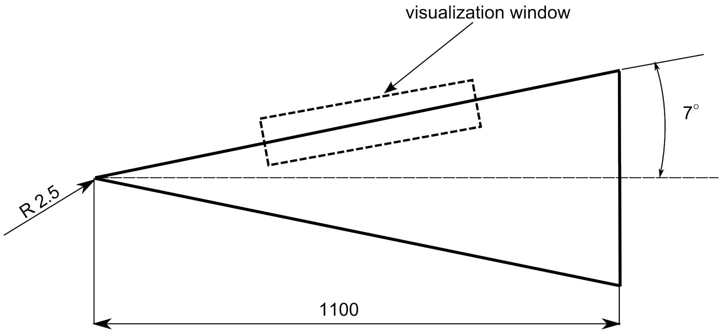

Figure 3.3: Cone model with visualization window. All dimensions are in mm, not to scale.

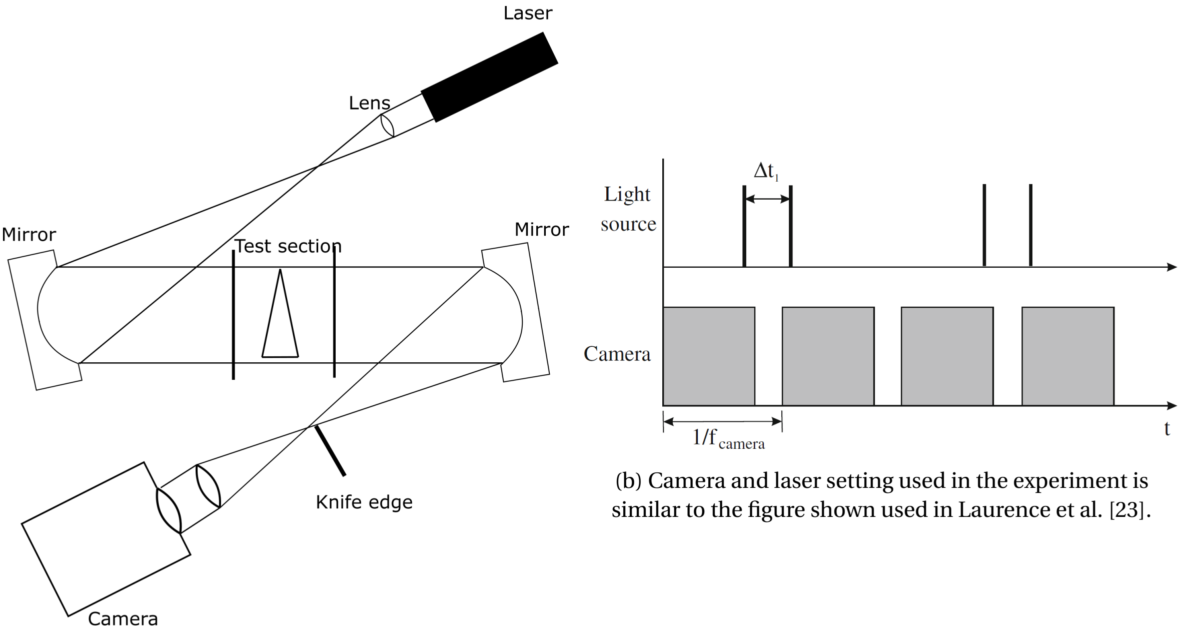

(a) Schlieren setup.

(b) Camera and laser setting used in the experiment is similar to the figure shown used in Laurence et al. [23].

Figure 3.4: Schlieren visualization setup.

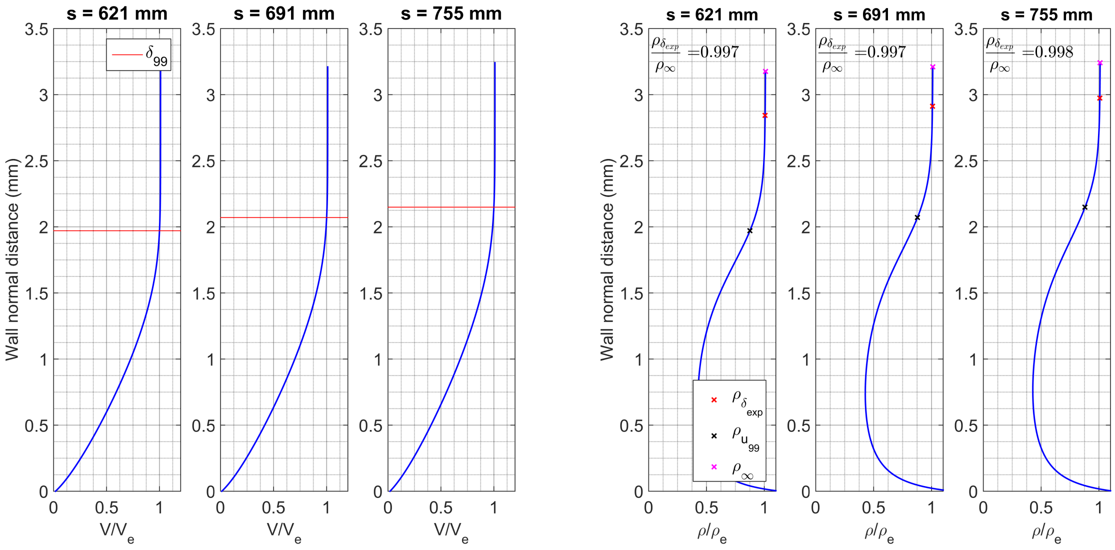

(a) Velocity profile.

(b) Density profile.

Figure 3.5: Boundary layer profile for run 1438, extracted at the beginning, center and end of visualization window.

3.1.3. Test conditions

The flow conditions are given in Table 3.1. The free stream Mach number is approximately 7, high enough for the second mode to be the most dominant instability in the boundary layer [27]. The enthalpy is kept rather constant for all the cases, and the unit Reynolds number is increased so that the visualized boundary layer is at different states of transition(early/late transition). Two nose radii (0.1 and 2.5 mm) are tested because a sharp nose radius initiates transition earlier than a blunt nose at a given Reynolds number [45], allowing to study a more mature boundary layer for lower Reynolds numbers.

Fig. 3.6 shows the surface heat flux sensor measurements. The theoretical laminar and turbulent heat transfer distributions are calculated using the reference temperature method [52]. The theoretical laminar and turbulent heat flux reduces in the stream wise direction as the temperature gradients decrease owing to a growing boundary layer. The boundary layer is considered transitional when the measured heat flux starts to deviate from the theoretical laminar heat flux distribution. Once transitional the heat flux continues to rise till a fully turbulent boundary layer is formed and then reduces and matches with the theoretical turbulent heat flux. As shown in Fig. 3.6 the test cases analyzed all capture a transitional boundary layer. The test cases are labeled as least/modestly/highly transitional based on the local Reynolds number and the state of the boundary layer from Fig. 3.6, given in table 3.3.

CFD simulations were performed using the DLR-TAU code to determine the boundary layer edge values of the flow variables, see table 3.2. The boundary layer edge conditions are used to compute the theoretical heat transfer distribution in Fig. 3.6. For each run three boundary layer profiles were extracted at the beginning, middle and end of the visualization window (see Fig. 3.5). The ratio of the density at the experimental boundary layer edge (determined from the schlieren images) and the free stream density ($\rho_{\delta_{exp}}/\rho_\infty$) is marked in Fig. 3.5b. Since schlieren measures density gradients, the boundary layer captured in the images is a density boundary layer whose edge is defined as $0.99\rho_\infty$. The proximity of the ratio $\rho_{\delta_{exp}}/\rho_\infty$ to the theoretical value ($\rho_e/\rho_\infty = 0.99$), shows the precision of the experiments performed in the HEG.

HEG Run number	M$_e$	T$_e$ (K)	p$_e$ (kPa)	Re$_e$($\cdot 10^6$ m^{-1})	δ_{u99} (mm)	δ (mm)	δ/δ_{u99}
1443	6.29	351.62	3.18	3.5	2.04	2.73	1.33
1440	6.29	351.66	3.18	3.5	2.06	2.93	1.42
1447	6.32	346.66	5.28	6.05	1.52	2.27	1.49
1308	6.29	351.66	3.18	3.5	2.1	2.33	1.10
1438	6.28	370.21	3.4	3.5	2.06	2.90	1.40
1439	6.28	370.21	3.4	3.5	2.04	3.1	1.51

Table 3.2: Boundary layer edge conditions from CFD solutions. δ_{u99} - velocity boundary layer thickness and δ - density boundary layer thickness. δ_{u99},δ reported in table is the average from the three profiles extracted.

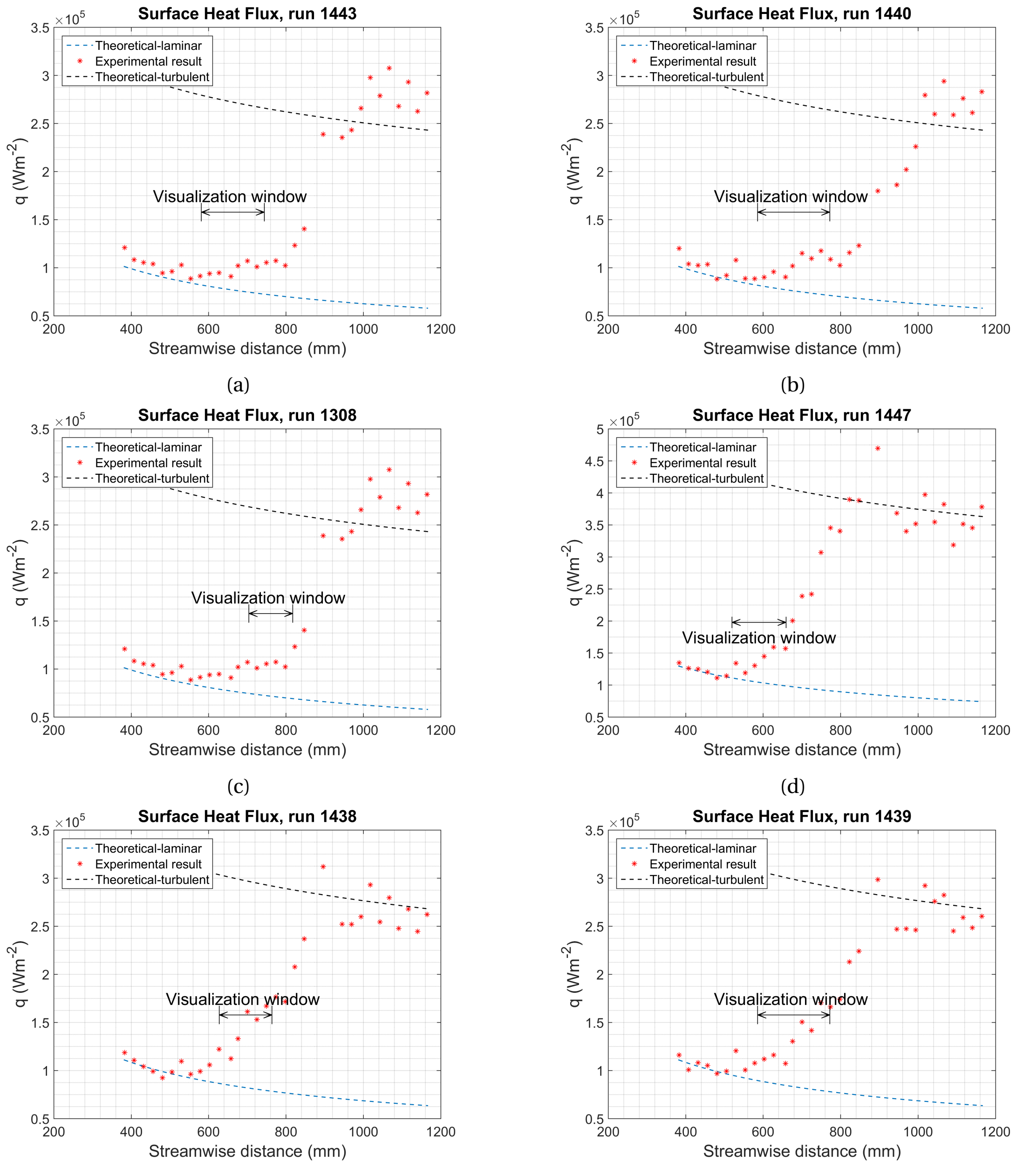

(a)

(b)

(c)

(d)

(e)

(f)

Figure 3.6: Surface heat flux measurements for the runs analyzed, figures show the state (laminar/transitional/turbulent) of the visualized boundary layer.

HEG Run number	local Re ($\cdot 10^6$)	Nomenclature
1443	1.57	Least transitional
1440	1.61	Least transitional
1308	1.81	Modestly transitional
1447	2.12	Modestly transitional
1439	1.61	Highly transitional
1439	1.65	Highly transitional

Table 3.3: Test case nomenclature based on the local Reynold's number and visulation window from Fig. 3.6. Local Reynold's number is the product of unit Reynold's number and mid point of visualization window.

3.2. Wavelet Analysis

An introduction to the wavelet transform was provided in section 1.2.2. This section continues with the theory of wavelet analysis based on the discussion presented in Bentley and McDonnell [3], Farge [13].

There are two types of wavelet transforms, the continuous wavelet transform (CWT) and the discrete wavelet transform (DWT). The CWT is computed for all scales that are set by the user and the wavelet is shifted over the signal under analysis in a continuous fashion. Whereas in the DWT the transform is computed at specific scales and positions. It is important to note that in both the cases the signal under analysis is discrete in time (or space). In the study here the continuous wavelet transform is used since the entire schlieren image should be analyzed and not just a portion of it.

The continuous wavelet transform is defined by equation 3.2, where a is the wavelet scale, b is the shift parameter which represents the wavelet shift, $s(x)$ is the signal under analysis and $h(x)$ is the wavelet function which varies depending on the mother wavelet selected. The Morlet wavelet is defined by equation 3.3 is an example of the function $h(x)$.

$$CWT(b,a) = \frac{1}{\sqrt{a}} \int h^* \left(\frac{x-b}{a} \right) s(x)\, dx \tag{3.2}$$

$$h(x) = \exp(-x^2/2)\cos(5x) \tag{3.3}$$

To be considered as a mother wavelet, the integral of the function $h(x)$ must be zero, this is known as the admissibility condition. Scaling of the wavelet causes wavelets of high frequency (small scale) to have better spatial/temporal resolution and wavelets of lower frequency (large scale) to have more duration and have lower spatial/temporal resolution as shown in Fig. 3.7b. A higher scale wavelet has more duration/support, which means a larger portion of the wavelet is non zero, which leads to coefficients being generated while taking the inner product. This is known as the cone of influence and is shown in Fig. 3.8. Fig. 3.8 is the wavelet transform of shifted impulse with impulse occurring at point 500. In the wavelet transform it is also possible to reconstruct the original signal from the wavelet coefficients computed, this is called invertibility.

Wavelet analysis was initially applied in fluid mechanics to study coherent structures occurring in turbulent flows. Fourier transform cannot be used to study coherent structures that occur in turbulent flows because of its nonlocal nature. The wavelet analysis is performed locally and is best suited to analyze coherent structures within a signal. The continuous wavelet transform allows to track the dynamics of coherent structures and measure their contributions to the energy spectrum.

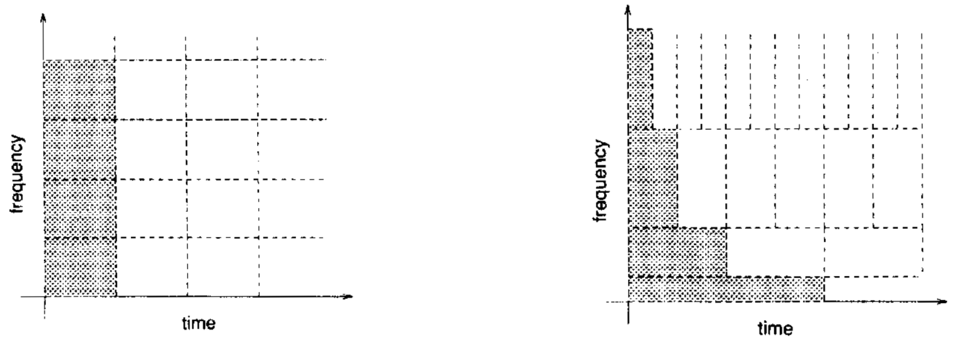

(a) Short time Fourier transform (STFT).

(b) Wavelet transform.

Figure 3.7: Time-frequency plane coverage. Dimensions of the square represent the frequency time resolution.

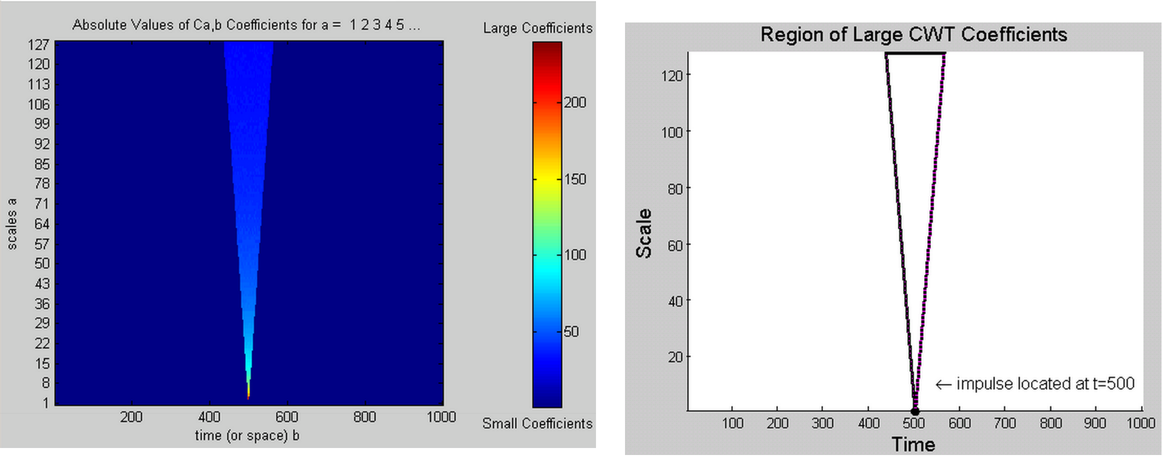

(a) Wavelet transform of an impulse signal, with impulse at t=500.

(b) Cone of influence due to the impulse.

Figure 3.8: Cone of influence generated while taking the wavelet transform.

3.2.1. Applying the wavelet analysis to schlieren images

As discussed in the previous section taking the wavelet transform of a signal allows to decompose a signal into different frequency components without loss of spatial content within the signal. Applying the wavelet analysis to schlieren images will allow to study the spatial distribution of the second mode waves and its harmonics and also compute the spatial amplification factors.

Each shock tunnel test generates approximately 470 images, which do not have the same brightness level. Hence first the raw images are taken and the brightness level of the images are normalized. A reference image is created by averaging all the images in a run and it's brightness is computed by averaging over all pixels. The brightness of each image is also computed and the image brightness is linearzed.

After the brightness of images are normalized, the reference image is subtracted from each image to remove background noise and improve the signal quality. The first step to consider while applying the wavelet analysis is the selection of an appropriate mother wavelet. From Fig. 3.9 it is seen that the response of the Mexican hat is lower than the Morlet wavelet in magnitude and does not reconstruct the original signal. The Haar wavelet also has a lower response and shifts the signal peak forward close to where a valley occurs in the original signal (phase shift). Hence the Morlet wavelet was selected for the analysis, as it gives a higher magnitude and is better at reconstructing a given sinusoidal signal. In order to perform the wavelet analysis, the frequency range of the second mode waves must be known to select appropriate scales for the mother wavelet. The fundamental frequency of the second mode waves is known from Fourier analysis, in which a schlieren image is taken, divided into six sections and a Fourier analysis is performed in each section to obtain the frequency of the second mode. From the Fourier analysis it was found that the second mode frequency reduction from the beginning to the end of the visualization window is around 20 kHz. The wavelet transform is done over a range of frequencies to account for the reduction in fundamental frequency as the wave packet develops (see section 4.1 for more details). The following steps are implemented in applying the wavelet transform to the images:

1. The wavelet analysis is applied on a single row for a range of frequencies, this generates a wavelet coefficient matrix. Fig 3.10 (middle left) shows the contour plot of this matrix. The range of frequencies set for each run is f_{beg}-30 kHz and f_{end}+30 kHz, where f_{beg} is second mode frequency at the beginning of visualization window and f_{end} is the second mode frequency at the end of the visualization window (see table 4.2 and section 4.1).

2. The maximum wavelet coefficient for each column in the coefficient matrix is found and stored (Fig 3.10 middle right). This vector now has wavelet coefficients over a range of frequencies, which would have been neglected had a fixed scale approach been followed.

3. These steps are done for all rows in the image above the cone surface. A contour plot is generated for analysis, see Fig. 3.10 (bottom). Fig. 3.11 shows a schlieren image superposed with maximum wavelet coefficients in a frequency range of 305-323 kHz. From the figure it is seen that the wavelet transform does capture the second mode structures in a schlieren image.

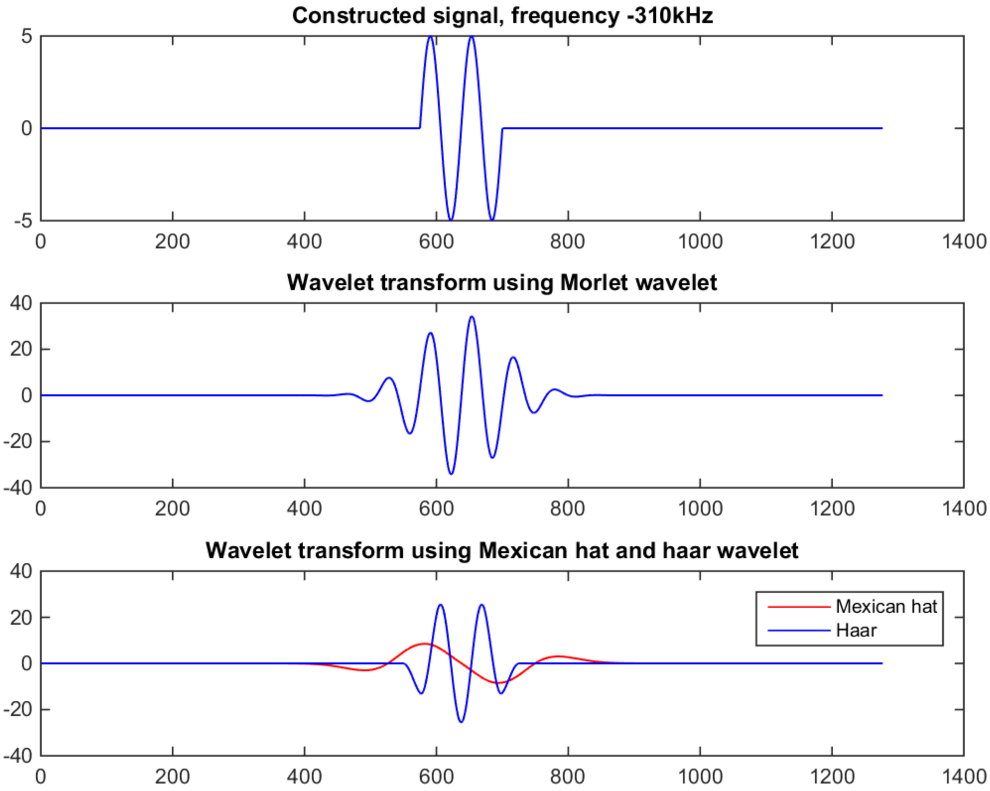

Figure 3.9: Studying the responses of different mother wavelets to a sinusoidal signal. Sinusoidal signal selected for this study since the density fluctuations are also sinusoidal in nature.

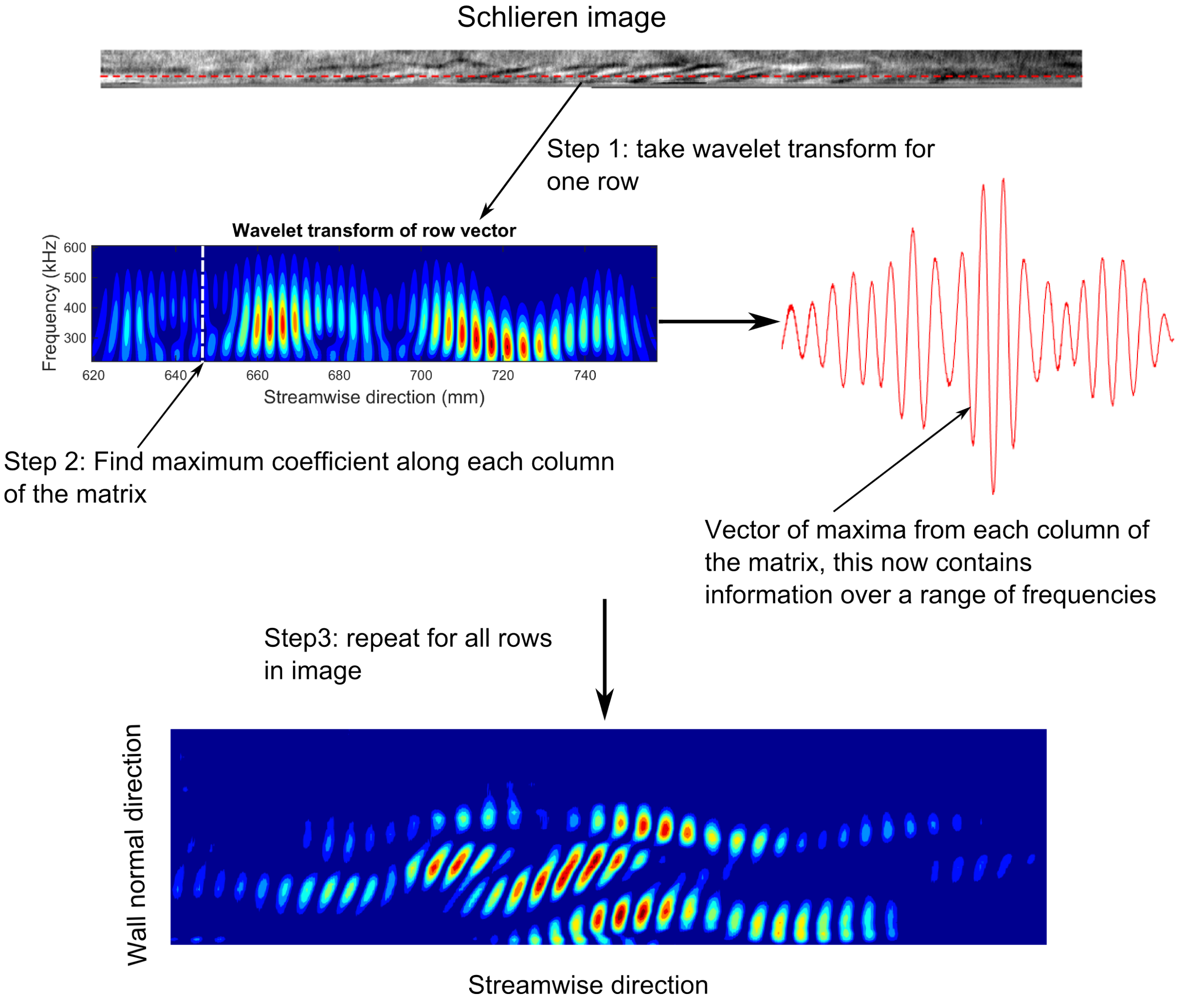

Figure 3.10: Applying the wavelet transform to schlieren image with a frequency range of ≈ ±40 kHz of the fundamental frequency.

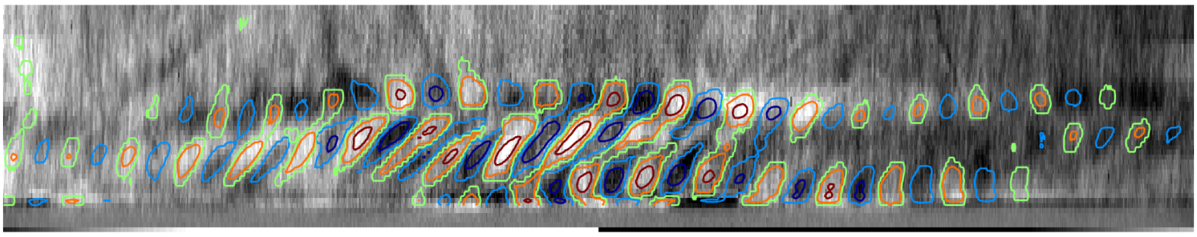

Figure 3.11: Schlieren image superposed with contour of maximum wavelet coefficients over a frequency range of 305-323 kHz.

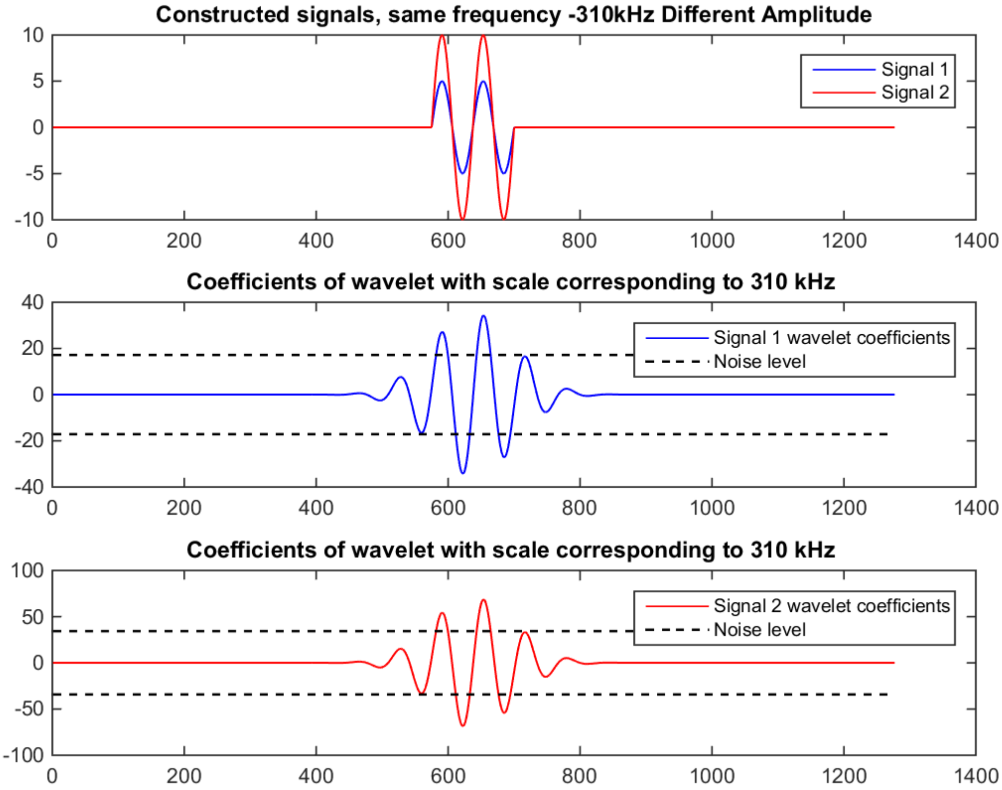

Figure 3.12: Figure demonstrates the linear nature of the wavelet analysis and also shows that the noise generated during analysis is equal to 50% of the maximum wavelet coefficient.

3.2.2. Important properties of wavelet transform

There are some properties of wavelet analysis which are important to the analysis performed in this study. Fig. 3.12 shows the response of the wavelet analysis to two signals which have different amplitudes. The coefficients of wavelet transform also double when the signal amplitude is doubled, which shows that the wavelet transform is a linear technique. The linear property is significant to study the growth rate of the waves because, if a wave is amplified it gives a higher amplitude and the wavelet analysis in turn generates a higher coefficient (since it is linear). The linear property of the wavelet transform is also important to study the energy distribution.

The wavelet analysis has a short coming as well. In Fig. 3.12 close to the start and end of the wave in the signal, there is an extra period generated even though there is no actual wave present at that location. This is the noise that is generated through the wavelet analysis. There is noise of significant amplitude close to the position of the actual waves, 50% of the maximum wavelet coefficient. For the results presented in chapter 4, coefficients greater than 60% of the maximum wavelet coefficient are taken; hence it is above the noise level.

3.3. Growth rate determination

To compute the growth rate of second mode waves two consecutive schlieren images shown in Fig. 3.13 are taken and Eqn. 3.4 is applied. Where A_1, A_2 are the wavelet transform coefficients from two schlieren images and Δs is the distance traveled by the wave packet between the images.

$$-\alpha = \frac{\ln(A_1/A_2)}{\Delta s} \tag{3.4}$$

First the wavelet transform of two consecutive images is computed. The wavelet coefficients of a row at a fixed height above the wall is taken from each image and cross correlated to find the displacement of the waves. The displacement corresponding to the maximum cross correlation coefficient gives the wave packet displacement (Δs).

In order to calculate the term A1/A2 in Eqn. 3.4, the vectors of wavelet coefficients have to be divided. If the coefficients shown in Fig. 3.15a are divided, large amplification factors are generated in the vicinity of local coefficient peaks (where local coefficient becomes zero) see Fig. 3.15b. To avoid this error the growth rates are computed only at the position of the peaks. Fig. 3.16 shows growth rates computed for the particular row. Since the amplification factor is not computed at all locations and only at the peak locations, it is interpolated for the distance between the peaks as shown in Fig. 3.16.

In the given example, the extent of the wave packet from Fig. 3.13(bottom) in the stream wise direction is 600 - 1200 pixel; hence this region is significant to the analysis while values close to 500 in the upstream portion of Fig. 3.16 can be ignored. These steps are performed for all the rows in the images to obtain the growth rate of the entire wave packet. The growth rates for the harmonics can also be found by simply changing the frequency range analyzed while performing the wavelet transform.

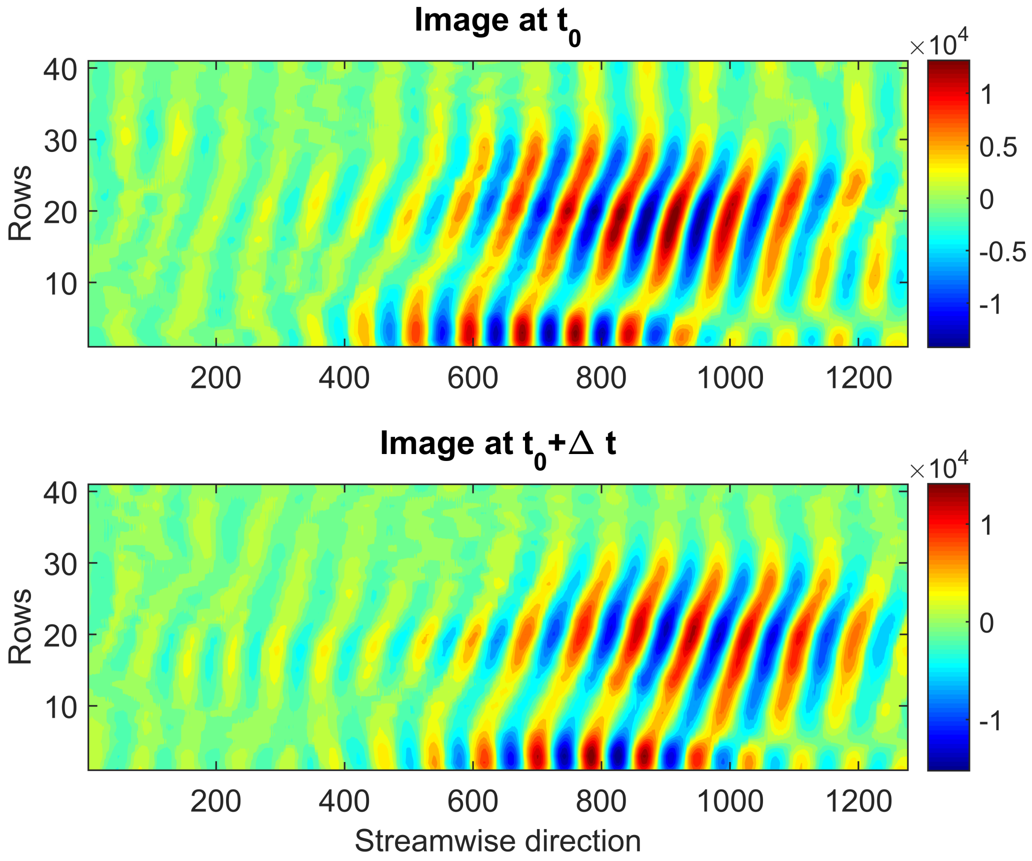

Figure 3.13: Computing the displacement from the cross correlation coefficients, Δs = 2.06mm.

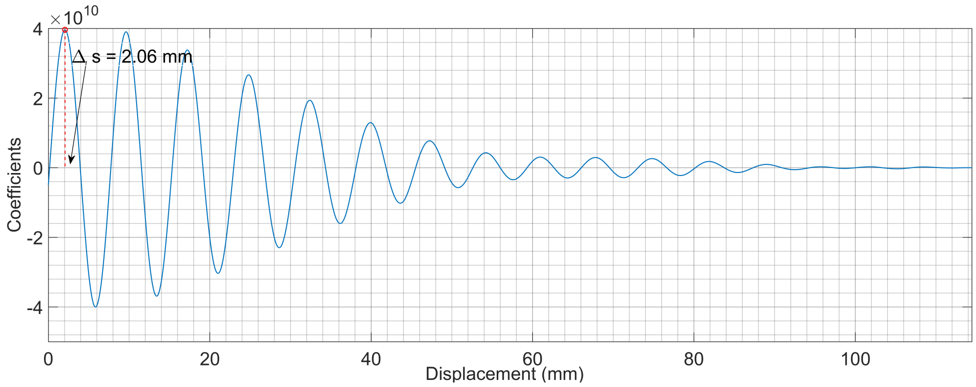

Figure 3.14: Computing the displacement from the cross correlation coefficients, Δs = 2.06mm.

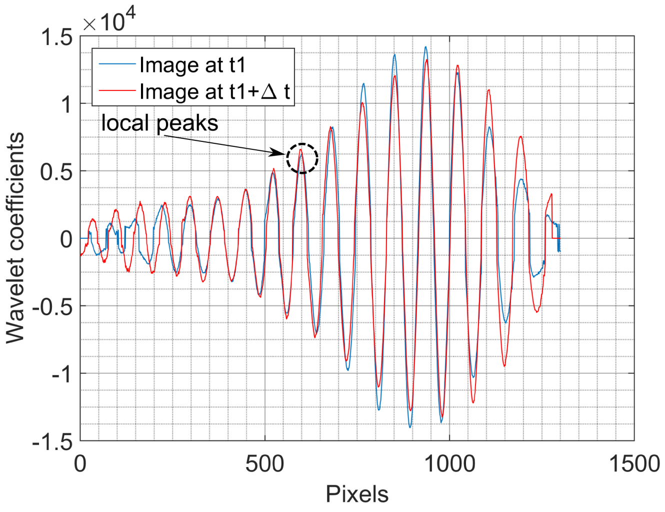

(a) Wavelet coefficients of a row from two consecutive images. Coefficients of image at t1+Δt is shifted to the right by the number of pixels determined from cross correlation.

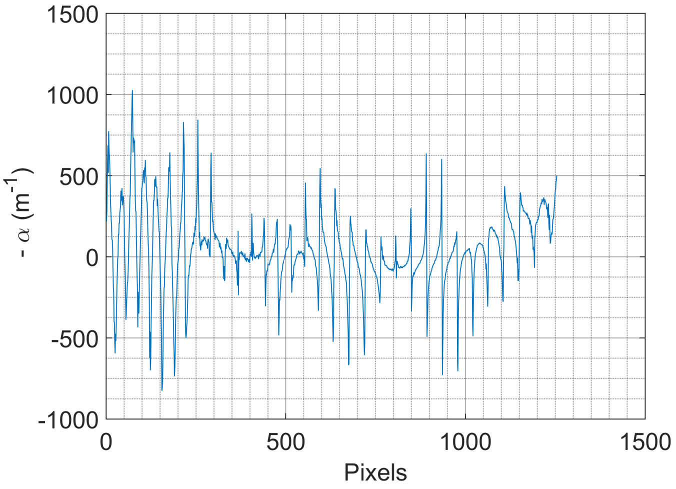

(b) Amplification factor computed from signals shown in Fig. 3.15a.

Figure 3.15: Computing growth rates for a row vector from schlieren image.

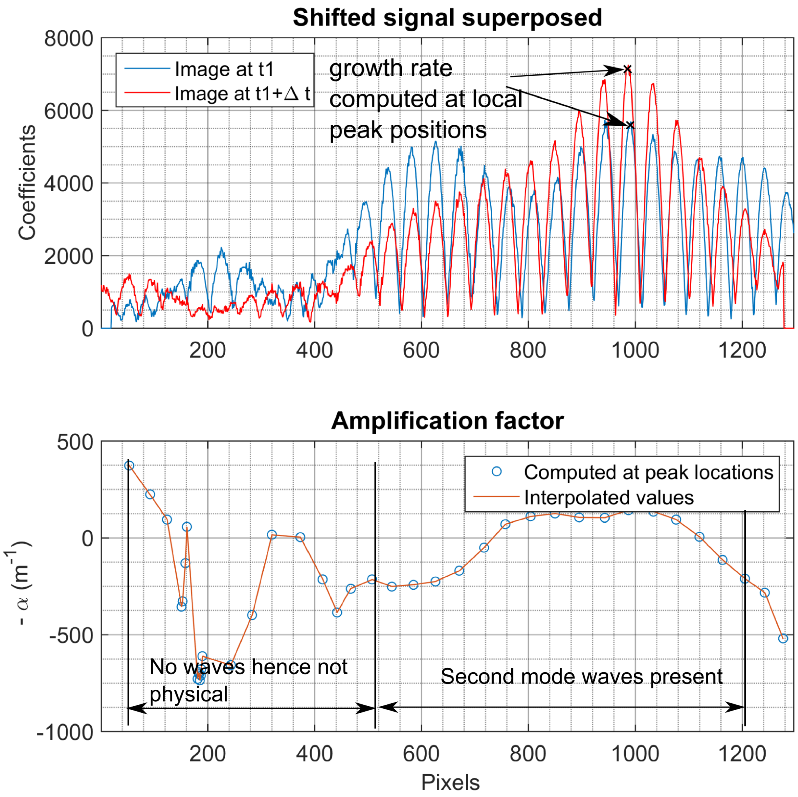

Figure 3.16: Amplification factor computed for one row of images from Run 1308.

3.4. Summary

The topics discussed in this chapter can be summarized into the following points:

1. The HEG is an impulse facility capable of simulating flight conditions at Mach 7. The flow conditions used in the experiments performed (cone model and hypersonic) are sufficient for the growth of the second mode waves.
2. Since the second mode waves cause density fluctuations, they can be visualized using schlieren visualization technique. A conventional Z-fold schlieren setup is used. A pulsed light source is used in the experimental setup to achieve a higher frequency and freeze the motion of the waves.
3. While using the Fourier transform to study the waves, there is a loss in spatial information. The wavelet analysis can be used to overcome this short coming of the Fourier transform.
4. The wavelet transform is a linear technique, and can be used to study the energy distribution and growth rate of instability waves. The wavelet transform also generates noise equal to 45% of the maximum amplitude. This is overcome by considering the coefficients which are above the noise level for the analysis.

From the discussion presented in this chapter the wavelet analysis will be used in the following ways to meet the research objectives:

- The wavelet analysis successfully captures the second mode waves in a schlieren image (see Fig. 3.11) and can be used to study the spatial development of instability waves captured in a schlieren image. Applying the wavelet analysis to schlieren images (as outlined in section 3.2.1) generates a matrix of coefficients, which can now be studied for different properties of the waves like the amplitude distribution in the stream wise or wall normal direction.

- By varying the scales of the wavelet the presence of harmonics can also be investigated and their growth (concentration of harmonic amplitudes) with respect to the fundamental wave can also be looked into. The wavelet analysis will also be used to extract the spatial growth rates of the fundamental wave and it's harmonic, using the procedure discussed in section 3.3.
- A sequence of schlieren images capturing instability growth and boundary layer transition can be decomposed into different wavelength (or frequency) spectra using the wavelet analysis. By decomposing into different spectra the most dominant instability waves can be identified.

4

Results and Discussion

The results of taking the wavelet transform of schlieren images are discussed in this chapter. The wavelet transform is applied: 1) to study the energy distribution of the second mode wave and its growth rates, 2) to identify harmonics of the fundamental wave and extract its location with respect to the fundamental wave. In the course of the study strong low frequency waves were observed, their effects and properties are also discussed. The test conditions are provided in Table 3.1 and the nomenclature assigned to the test cases are given in Table 3.3.

4.1. Determining the wavelength and velocity of the second mode waves

Before applying the wavelet transform the frequency range of the second mode waves have to be determined in order to select the scale of the mother wavelet accordingly, which can save computational time. In this section the Fourier analysis and cross correlation is used to determine the frequency and speed of the waves.

The wavelength of the Mack mode was determined by taking a Fourier transform of the schlieren image. The analysis was performed by taking a schlieren image and dividing the image into six sections in the span wise direction, and taking the Fourier transform for every row in the section and averaging it over all images in a run. Fig. 4.1 shows the Fourier transform for each of the six sections of a schlieren image. The velocity was determined by cross correlating consecutive images. Using the wave velocity and wavelength, the frequency of the waves are calculated and reported in table 4.1. According to linear stability theory the second mode waves must have velocity approximately equal to free stream velocity and a wavelength approximately twice the boundary layer thickness [27, 30]. From table 4.1 it is seen that the experimental results agree well with the theoretical predictions of Mack [27, 30]; hence it is verified that the waves captured in the schlieren images are second mode waves.

As the wave develops second mode wavelength increases (or frequency reduces) due to the growth in boundary layer, this is seen in table 4.2 which shows the second mode frequency at the beginning and end of the visualization window. This was also observed in previous hot wire [48] and PCB [8] investigations (discussed in chapter 2). Fig. 4.1 shows that the waves are concentrated close to the boundary layer edge, agreeing with the observations of Kimmel et al. [18]. The growth of first harmonics is also observed by the increase in amplitude for $\lambda/\delta \approx 1.25$ from Fig. 4.1a to 4.1f as the wave travels from the beginning of the visualization window towards the end of it. Fig. 4.2 shows the Fourier transform for the other test cases. The first

HEG Run number	δ (mm)	λ/δ	v_{SM} (m/s)	f_{SM} (kHz)	V_∞ (m/s)	v_{SM}/V_∞
1443	2.34	2.55±0.41	2148±1	326±50	2500	0.85
1440	2.52	2.27±0.34	2102±1	318±47	2486	0.85
1308	2.33	2.63±0.44	2022±5	275±46	2405	0.84
1447	2.09	2.23±0.32	2109±2	424±59	2432	0.86
1438	2.39	2.25±0.47	2106±1	309±64	2481	0.85
1439	2.23	2.20±0.55	2114±2	305±57	2480	0.85

Table 4.1: Wavelength, frequency and velocity of the second mode waves. The values show that the experimental results agree with the theoretical predictions.

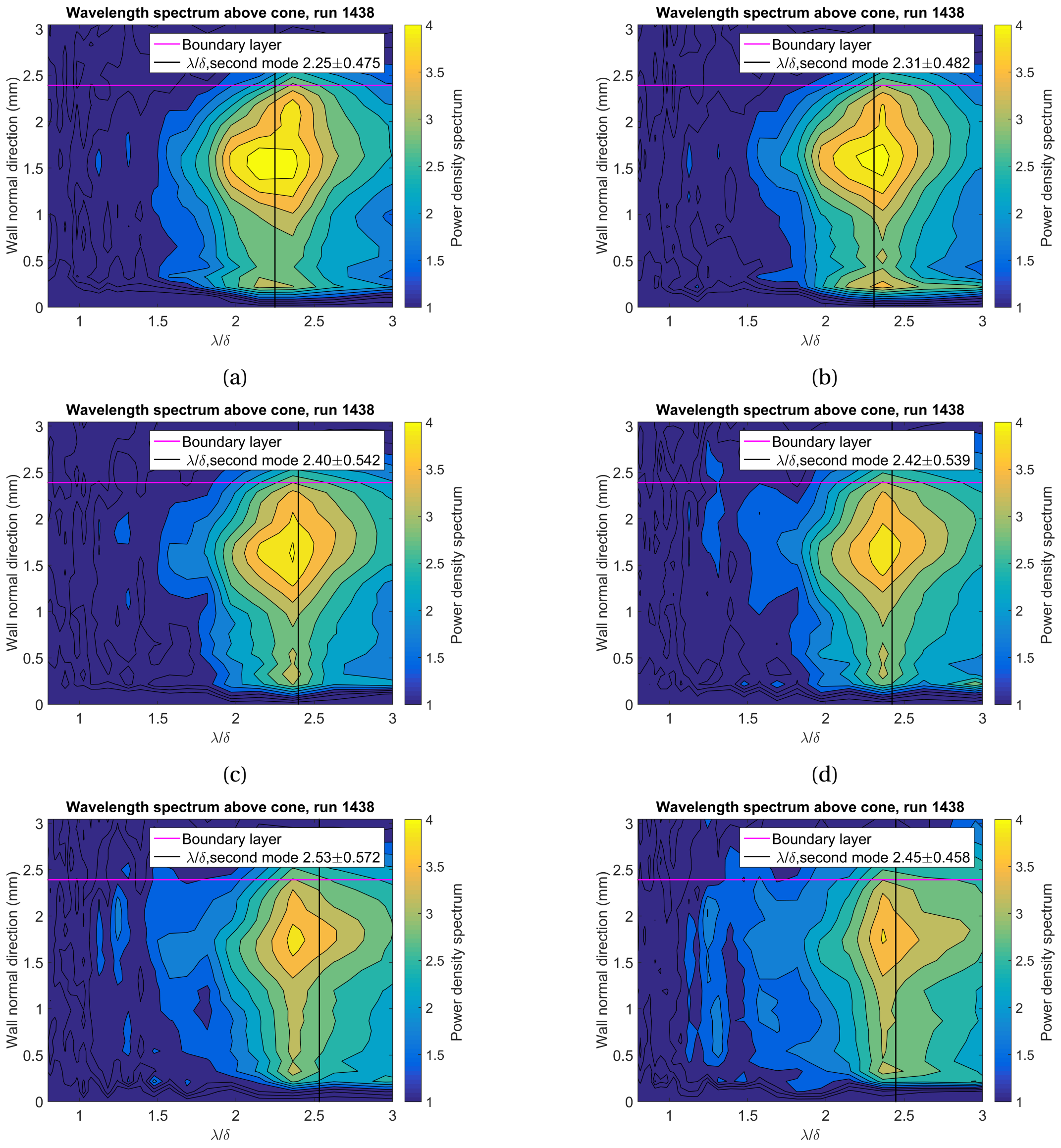

(a) (b)

(c) (d)

(e) (f)

Figure 4.1: Fourier transform of schlieren image divided into 6 sections. Run 1438.

harmonic is present in Run 1439, as observed by the amplitude present for $\lambda/\delta \approx 1.25$ in Fig. 4.2d.

HEG Run number	f_{bw} (kHz)	f_{ew} (kHz)
1443	343	308
1440	323	310
1308	285	260
1447	441	405
1438	323	305
1439	310	302

Table 4.2: Second mode fundamental frequency at the beginning (f_{bw}) and end of visualization window (f_{ew}).

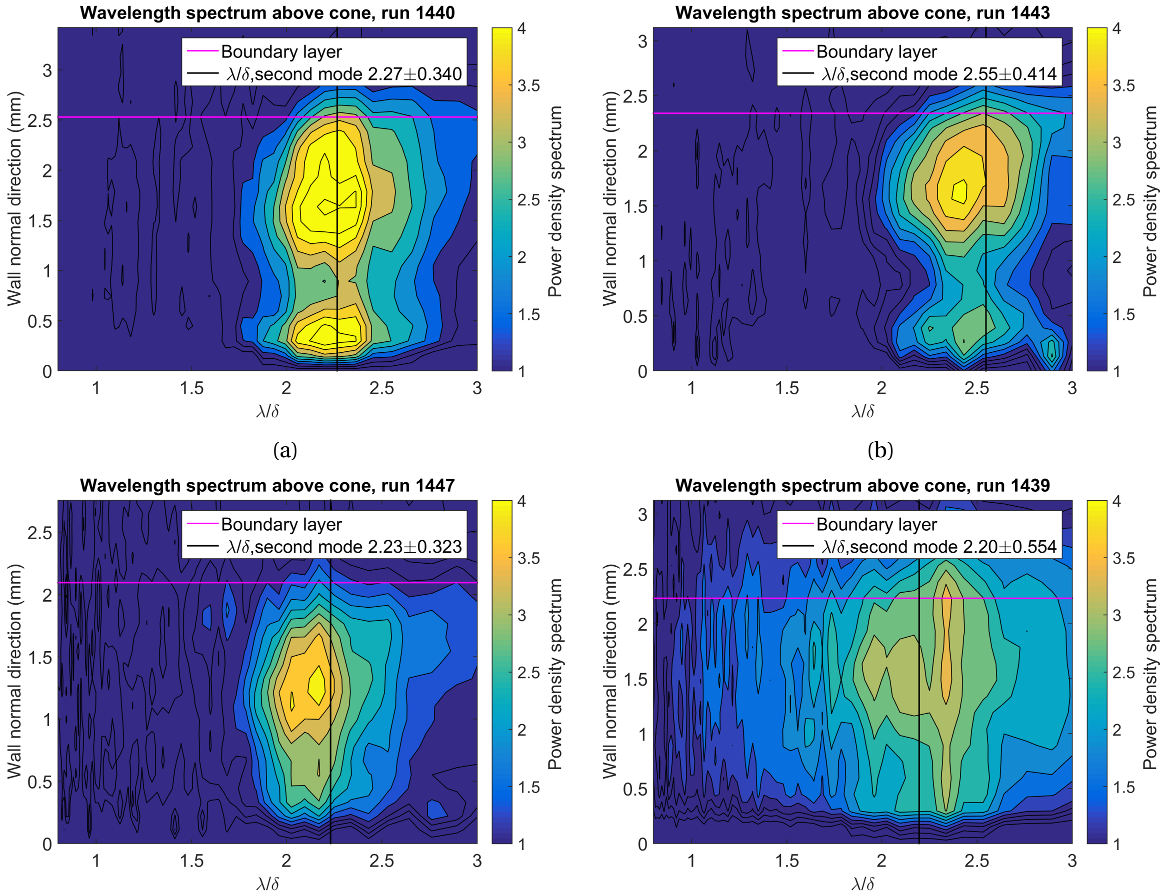

(a) (b)

(c) (d)

Figure 4.2: Fourier transform of schlieren image.

4.2. Second mode fundamental wave amplitude distribution and growth rates

The wavelet analysis is applied to schlieren images following the procedure outlined in section 3.2.1. Table 4.2 gives the frequency of the second mode waves at the beginning and end of the visualization window, obtained by taking the Fourier transform of different sections of a schlieren image. For the wavelet analysis the frequency range considered is f_{bw}-30 kHz and f_{ew}+30 kHz. In this section the wavelet analysis is applied to schlieren images to study the second mode amplitude distribution and growth rates.

4.2.1. Discussion on wall normal amplitude distribution

A number of studies have shown the second mode waves to be concentrated close to the boundary layer edge (discussed in section 2.1 and 2.2). Fig. 4.3, shows the wavelet transform for a sequence of images. The crosses indicate the location of the maximum amplitude for individual compression/expansion wave, referred to as the *wave peaks* (see Fig. 4.4). The wave peaks are concentrated at the outer half of the boundary layer and also show a movement within the boundary layer. Fig. 4.5 shows the wave peak locations for a sequence of images, it can be seen that there is a movement in the wave peak locations. An analysis was performed for the entire run and the number of wave peaksN_p, were converted into a contour plot, shown in Fig. 4.6. In Fig. 4.6 the wave peak vertical locations are plotted against the normalized wave packet length, where 0 indicates wave packet trailing edge and 1 indicates leading edge. In this section a study of the wall normal amplitude distribution of the wave packet is discussed.

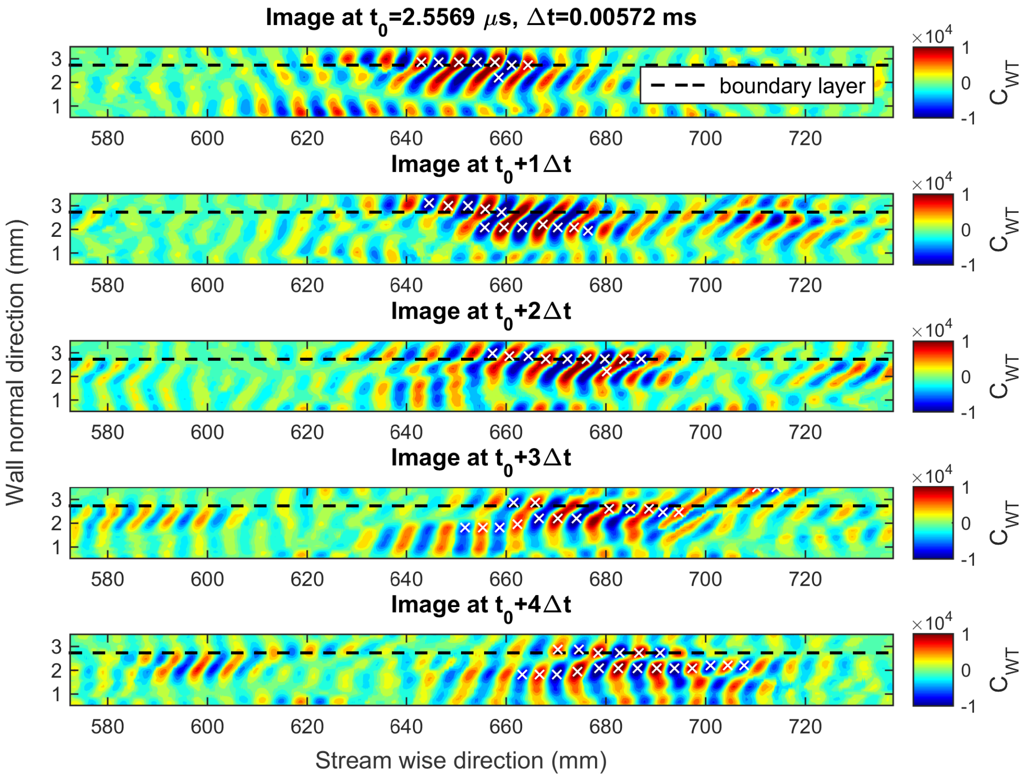

Figure 4.3: Sequence from run 1443, the crosses indicate location of maximum amplitude for each wave. Figure shows the movement of the maximum wave amplitude (wave peaks).

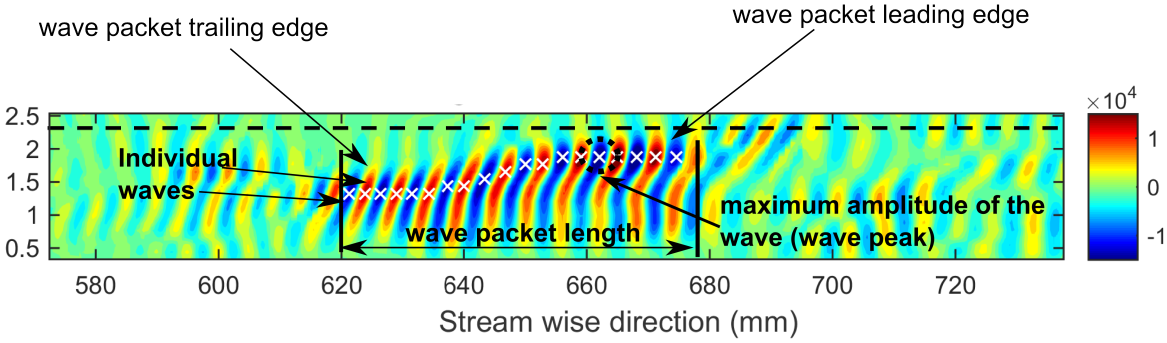

Figure 4.4: Wave packet length and location of the individual wave peaks.

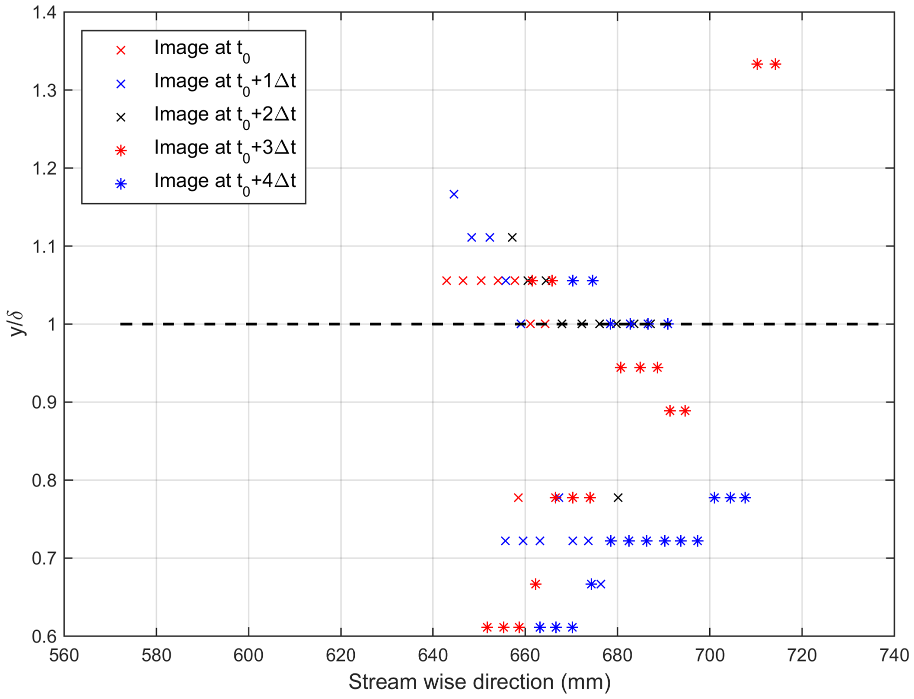

Figure 4.5: Variation in wave peak locations for a sequence of images.

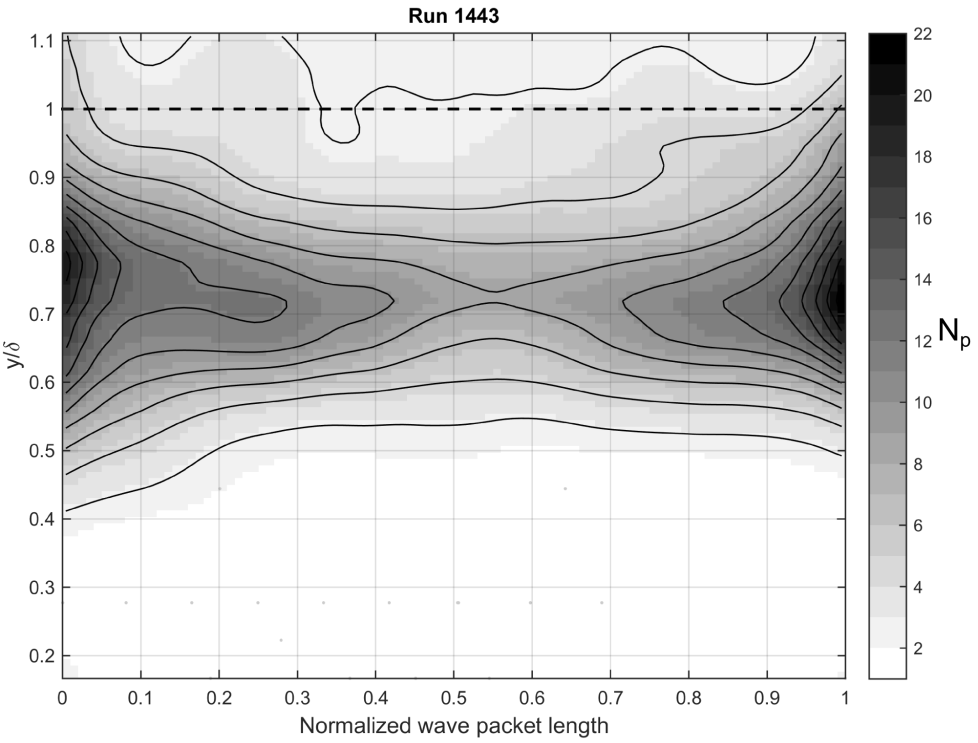

Figure 4.6: Distribution of wave peak positions along wave packet length for run 1443.

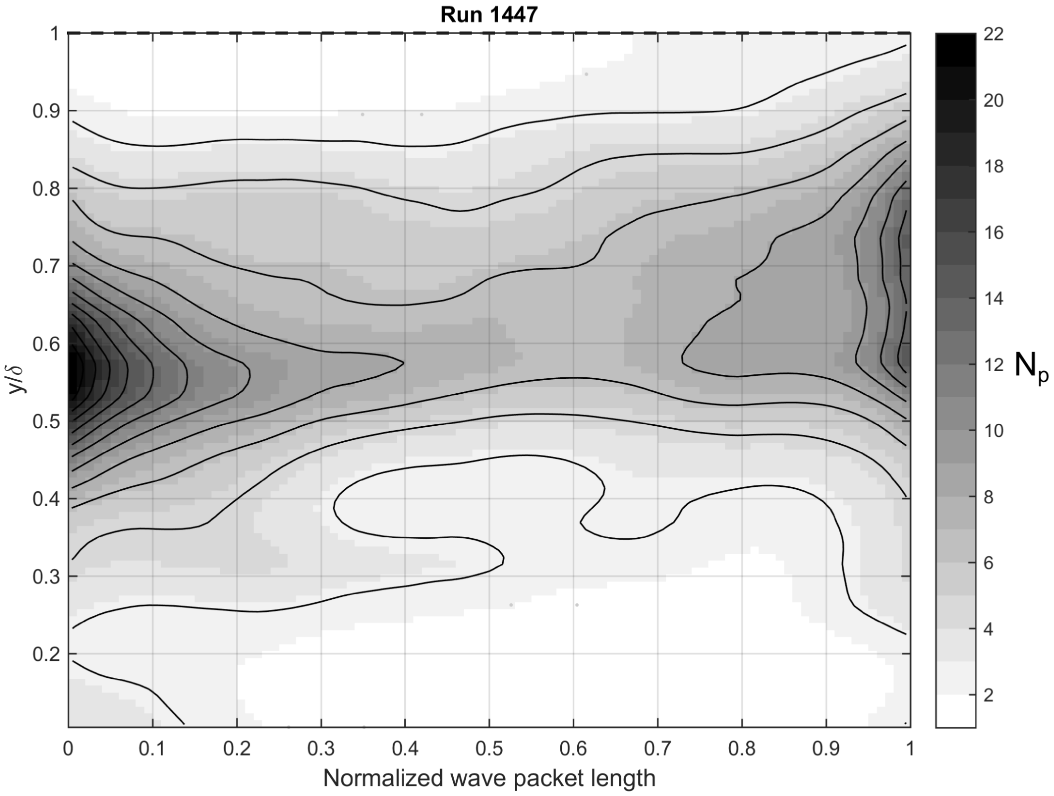

Figure 4.7: Distribution of wave peak positions along wave packet length for run 1447.

From Fig. 4.6 it is observed that in run 1443 the wave peaks are concentrated near the boundary layer edge throughout the length of the wave packet. The early hot wire measurements of Demetriades [10], Kimmel et al. [18] and Stetson et al. [48] showed that the second mode waves were concentrated at the boundary layer edge. Further Laurence et al. [25] performed Fourier analysis on schlieren images, which revealed that in the early stages of second mode development the energy was concentrated close to the boundary layer edge. The observed concentration of the wave peaks in the outer half of the boundary layer edge in Fig. 4.6 is in agreement with these published results and indicates that the wave packets in run 1443 are its early stages of development.

The results for run 1440 (shown in Fig. A.1) are different compared to run 1443, although both runs capture the least transitional boundary layer (see table 3.3 for run nomenclature). There are peaks concentrated close to the wall, which have been reported by Laurence et al. [25] (shown in Fig. 2.12). The position of the wave peaks in the boundary layer do not shift vertically (this occurs for highly transitional boundary layers discussed next), but remains fixed approximately at the same height similar to run 1443. Run 1440 visualization window is further downstream compared to run 1443, see table 3.1 and could be a reason for the development of peaks close to the wall.

Comparing Fig. 4.6 with 4.7 which visualizes a more transitional boundary layer, it is observed that the wave peaks while still concentrated in the outer half of the boundary layer have a larger vertical spread within the boundary layer. The leading edge of the wave packet (normalized wave packet length=1) especially has peaks that are spread throughout the boundary layer. This observation agrees with the result of Kimmel et al. [18] shown in Fig. 2.4b, where for the higher Reynold's number tests the vertical extent of the second mode waves increased. A close look at Fig. 2.18b also shows that second mode waves are initially concentrated near the boundary layer edge (extreme left in Fig. 2.18b) and as it develops the vertical extent within the boundary layer increases. The results from run 1438 which also captures a highly transitional boundary layer, are similar to run 1447 (see Fig. A.2). It is also important to keep in mind that the movement of the wave peaks towards the wall as it develops can also indicate that the wave packet is becoming three dimensional (wave angle non zero). However in the absence of span wise sensor measurements, it is not possible to verify this.

Another interesting observation is the breaking up of the waves into a double peak distribution (see image at $t_0+4\Delta t$ from Fig. 4.3). Laurence et al. [25] performed Fourier analysis in the wall normal direction on schlieren images and observed a shift from a two peak distribution to three peaks within the boundary layer (see Fig. 2.12, section 2.2). For the sequences analyzed in this study a three peak distribution was not found.

To conclude this discussion, the major observations are reiterated:

1. In the early stages of second mode development the wave peaks are concentrated in the outer half of the boundary layer. This is observed for the least transitional cases (run 1443 and 1440).
2. As the second mode develops the wave peaks tend to shift towards the wall and there is an increase in the vertical extent of the wave packet. This is observed for modestly transitional and highly transitional cases (run 1447 and 1438).

4.2.2. Discussion on stream wise amplitude distribution

Sivasubramanian and Fasel [39] observed that for a linear wave packet higher amplitudes were concentrated towards the leading edge of the wave packet, see Fig. 2.16. In experiments performed by Casper et al. [8], wave packets were observed with energy concentrated at the leading and at the center of the wave packet (see Fig. 2.17). Taking the wavelet transform of schlieren images with second mode waves allows to study the amplitude distribution along the length of the wave packet. To study the amplitude distribution along the length of the wave packet, the wavelet coefficients and the stream wise distance were averaged for each wave as shown in Fig. 4.8). The individual wave amplitude is normalized by the maximum amplitude of the strongest wave. The normalized amplitude is plotted against the normalized wave packet length for a sequence of images from a run as shown in Fig. 4.9, where normalized wave packet length of 0 indicates the trailing edge and 1 is the leading edge of the wave packet.

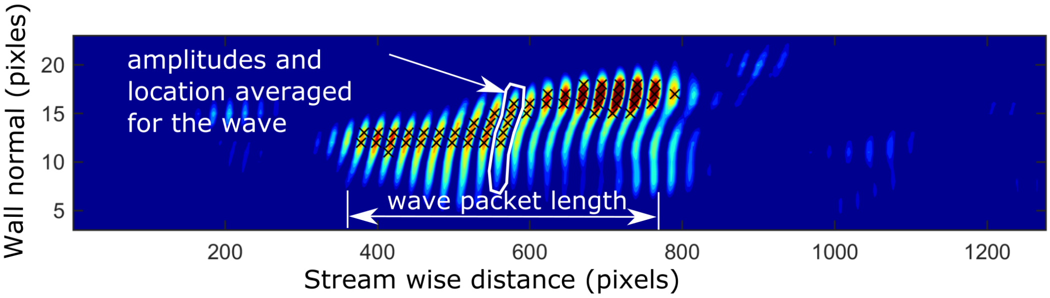

Figure 4.8: Averaging the coefficients and stream wise location of each wave, to compute the energy distribution in the stream wise direction.

From Fig. 4.2a and 4.2b it is seen that harmonics do not develop for Runs 1440 and 1443 (discussed in section 4.1); Hence the wave packets that develop in these cases are expected to be linear. Fig. 4.9 shows the evolution of stream wise amplitude distribution over a sequence of schlieren images for run 1440. In Fig. 4.9 (a)-(d) the maximum wave packet amplitudes are concentrated towards the leading edge, agreeing with the DNS results of Sivasubramanian and Fasel [39]. As the wave packet develops the amplitudes shifts towards the center of the wave packet see Fig. 4.9(e)-(f), similar to the result of Casper et al. [7] (see Fig. 2.17). This redistribution of amplitudes from the leading edge to the center of the wave packet is also observed in run 1443, see Fig. A.3a. For run 1443 the amplitudes eventually are distributed equally over the length of the wave packet Fig. A.3a(d). The wavelet transform of the schlieren images were performed in the first harmonic range to study if harmonics were responsible for the redistribution of amplitudes. The redistribution of amplitudes was not accompanied by the appearance of harmonics, indicating that non linear mechanisms do not cause this redistribution. For runs 1438 and 1447 that capture a more mature boundary layer amplitudes are redistributed from the leading edge to the entire length of the wave packet without any concentration to the center, see Fig. 4.10 and A.3b. Harmonics did not develop in this case as well, hence ruling out non-linear mechanisms causing them. The major observations based on the analysis on stream wise energy distribution are as follows:

1. Linear wave packets exist in the boundary layer which have the maximum amplitudes concentrated toward the leading edge of the wave packet. This agrees with the computational result of Sivasubramanian and Fasel [39]. For the test cases which are least transitional (run 1443 and 1440), the amplitudes

are redistributed from the leading edge to the center of the wave packet and eventually reach a uniform distribution.

2. For a wave packet in the modestly transitional and most transitional boundary layer(run 1447 and 1438), the energy is redistributed from the leading edge to the full length of the wave packet.

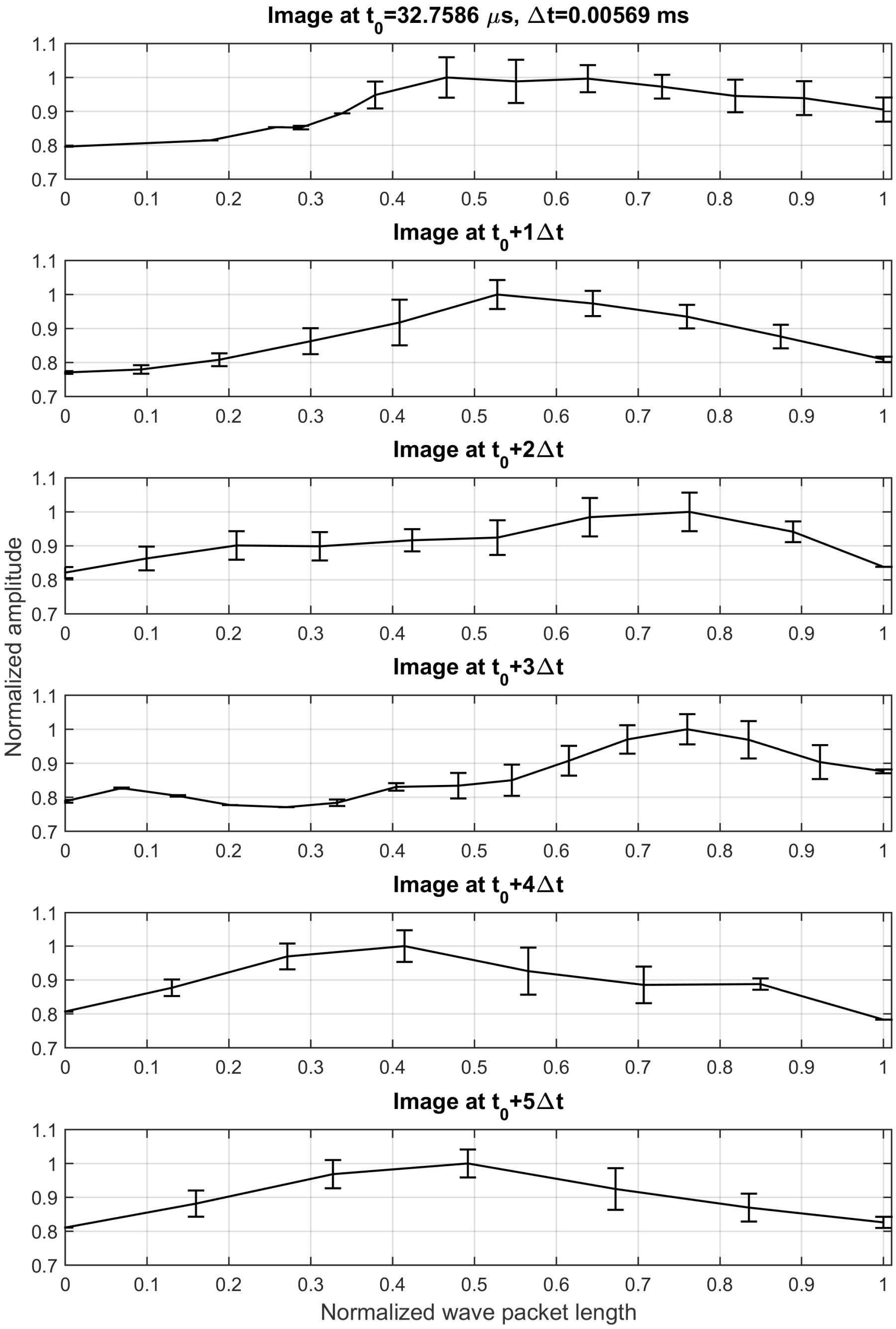

Figure 4.9: Stream wise energy distribution for a wave packet, run 1440. Figure shows the redistribution of energy from the leading edge toward the center of the wave packet.

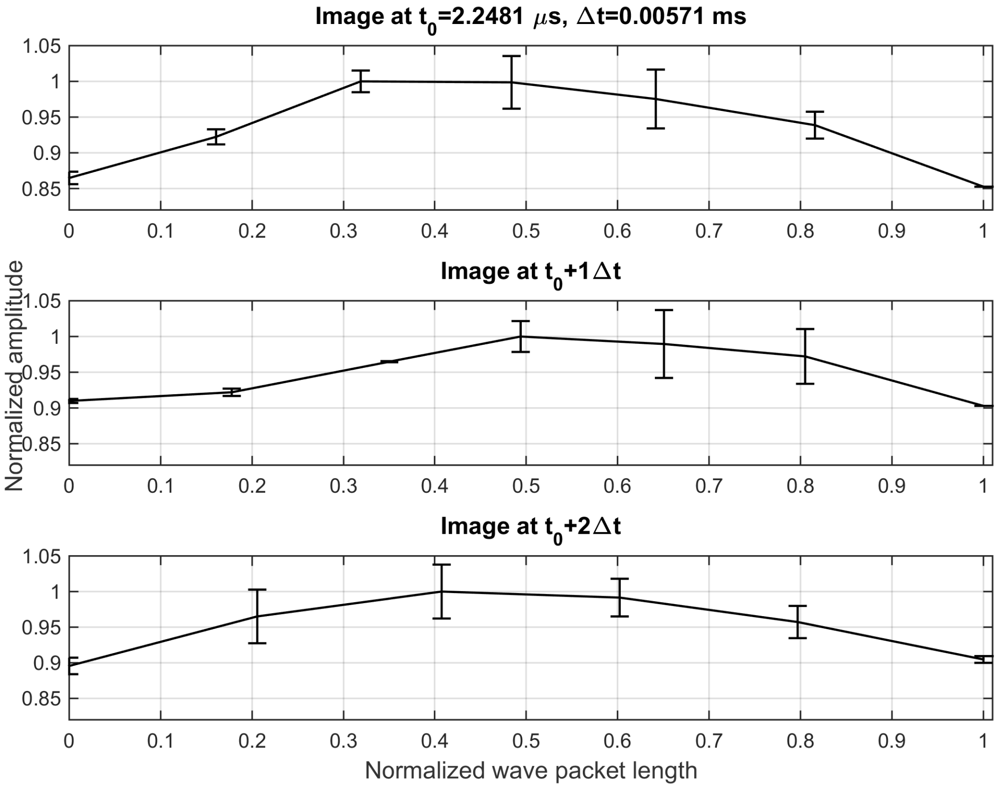

Figure 4.10: Stream wise energy distribution for a wave packet, run 1438. Figure shows the redistribution of energy from the leading edge to the full length of the wave packet.

4.2.3. Discussion on growth rates of second mode waves from schlieren images

The method followed to compute the growth rate was outlined in section 3.3. Fig. 4.11, shows the growth rates computed for a sequence of images of run 1438. Certain regions of the wave packet grow in amplitude while others decay in this sequence of images (Fig. 4.11b), especially at the edges of the wave packet. The regions of strong growth and decay in the wave packet are indicated by white ellipses in Fig. 4.11b. These large values arise due to the sudden appearance/disappearance of structures as the wave packet changes it's structure during development inside the boundary layer. Ignoring the extreme values that occur at the edges of the wave packet, the maximum amplification factor in the core of the wave packet is 45 m^{-1} which is higher than the values reported in literature presented in Table 2.1.

Also observed in Fig. 4.11b is the growth of the structures towards the boundary layer edge (indicated by red ellipses in Fig. 4.11b). This is also seen in sequences from other test cases shown in appendix A.3. The growth of waves towards the boundary layer edge agrees with the previous discussion on the wall normal energy distribution (see section 4.2.1), in which it was concluded that the second mode wave concentrates high amplitudes close to the boundary layer edge. From the observations of this section and section 4.2.1 it is concluded that the second mode waves tend to amplify the structures toward the boundary layer edge, which explains the observations of Kimmel et al. [18] and Laurence et al. [25] who observed that the waves are concentrated at the boundary layer edge.

4.3. Applying wavelet analysis to study harmonic waves

Fig. 4.12 shows a schlieren image (top), wavelet transform of the image with frequency range corresponding to second mode fundamental wave (Fig. 4.12 middle) and wavelet transform of the schlieren image with a frequency range corresponding to the first harmonic of the fundamental wave (Fig. 4.12 bottom). These high frequency waves have been reported in hot wire measurements[10, 48], PCB sensors [5, 9], heat flux measurements [37] and schlieren images [23, 25]. The frequency band in which the high frequency waves occur is predicted to be stable according to the linear theory, the frequency is too low to be the third mode

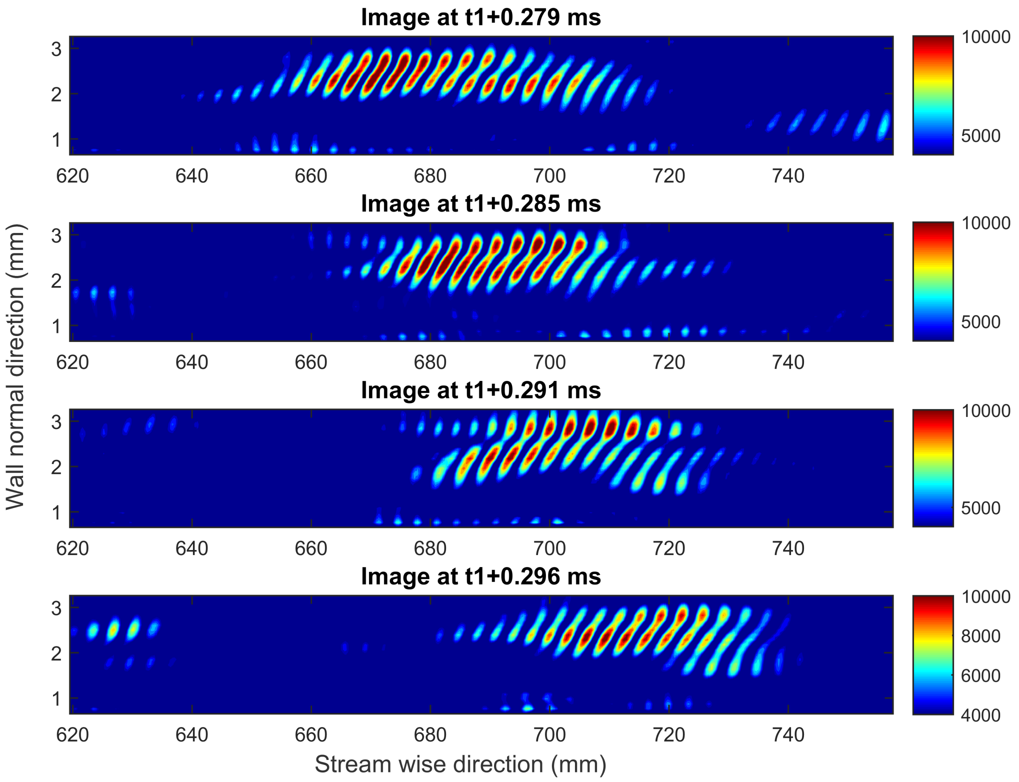

(a) Wavelet transform of images 50-53 of run 1438, used to compute the growth rates in Fig. 4.11b.

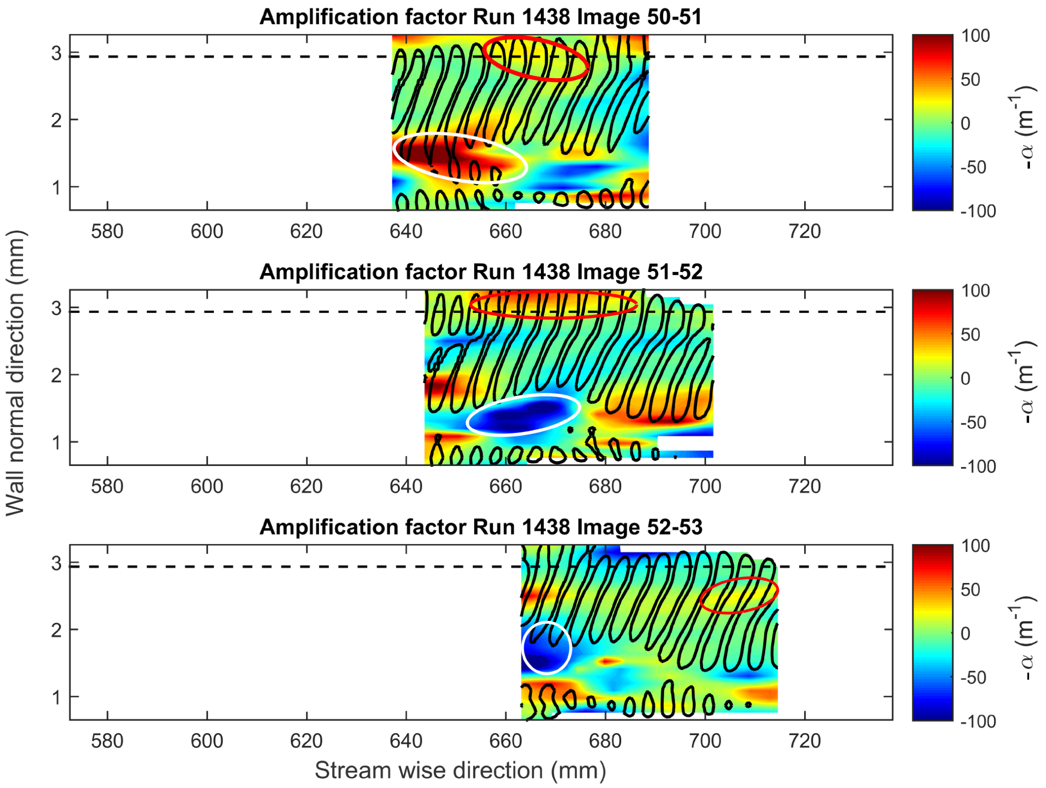

(b) Amplification factor computed from images shown in Fig. 4.11a. The white ellipses indicate regions of strong growth and decay showing the rapid change in wave packet structure. Red ellipses show amplification of wave close to boundary layer edge.

Figure 4.11: Growth rates for a sequence of images from run 1438.

instability [47] and the high frequencies are multiples of the fundamental frequency. Based on these reasons researchers concluded that this high frequency wave is a harmonic of the second mode fundamental wave, generated due to non-linear mechanisms in the boundary layer [47]. Fig. 4.12 shows that the wavelet transform can successfully identify the harmonic waves in a schlieren image.

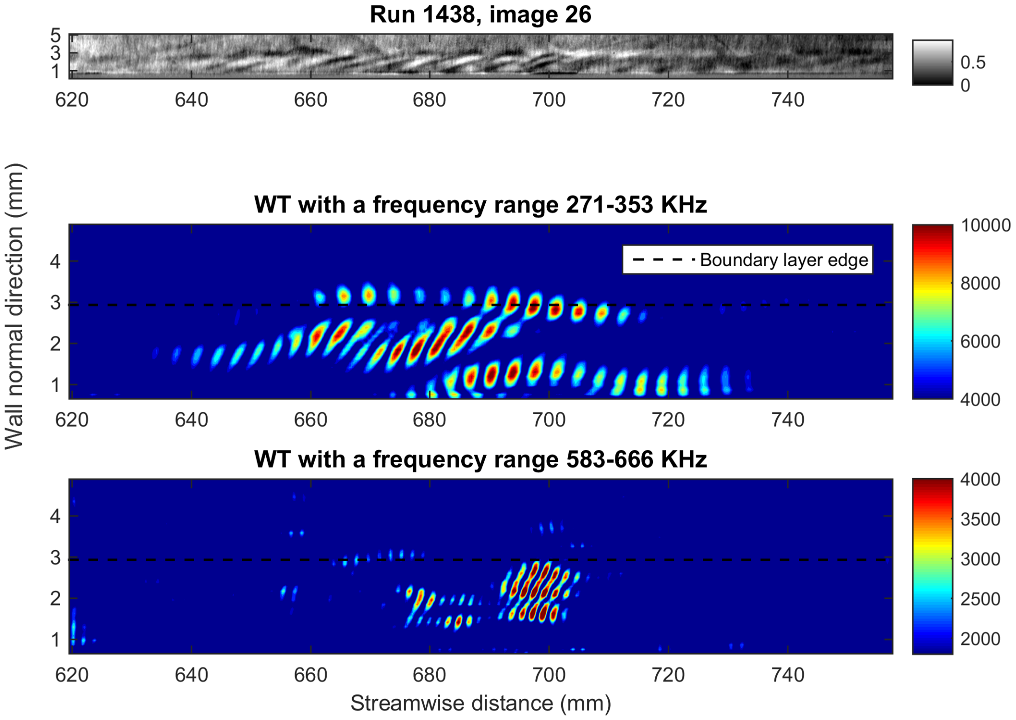

Figure 4.12: Wavelet analysis applied to a schlieren image (top) to capture the second mode waves (middle) and the first harmonic (bottom). Figure shows absolute wavelet coefficients.

4.3.1. Discussion on first harmonic wave

As stated earlier the appearance of harmonics indicate that non linear mechanisms are present in the boundary layer. Harmonics are expected to develop in a boundary layer that is in the late stages of transition. From the Fourier transform of schlieren images (Fig. 4.1 and 4.2), runs 1438 and 1439 are the ones with strong harmonics present. Fig. 4.12 shows the first harmonic for Run 1438. On performing the wavelet analysis on the schlieren images with frequency range corresponding to the first harmonic, it was found that the harmonics were present for run 1438 and not present for run 1439, contrary to the result from Fourier analysis. On inspection of run 1439 it was found that there were too many diaphragm particles in the images which contributed to high frequency content and not harmonic waves. In this way the wavelet analysis can even correct the results of the Fourier analysis.

It was also observed that the harmonics developed at the center of the wave packet. In Fig. 4.12 (middle) the stream wise extent of the fundamental wave is from 660 - 720 mm and the harmonics are present from 690 - 700 mm, approximately at the center of the wave packet. This result agrees with the observations of Laurence et al. [25], who also concluded that harmonics were concentrated at the center of the wave packet (see Fig. 2.13). Fig. 4.13 compares the stream wise amplitude distribution of the second mode fundamental wave and its harmonic. Fig. 4.13 shows that the harmonic amplitude is stronger where the fundamental wave amplitude is strong. This was also observed in other test cases shown in appendix A.8. This indicates that the harmonics develop where the fundamental wave amplitudes are high. Comparing the stream wise amplitude distribution of the fundamental and harmonic waves (Fig. 4.13 and A.8), it is concluded that the harmonic waves develop in regions where the amplitude of the fundamental second mode wave are high.

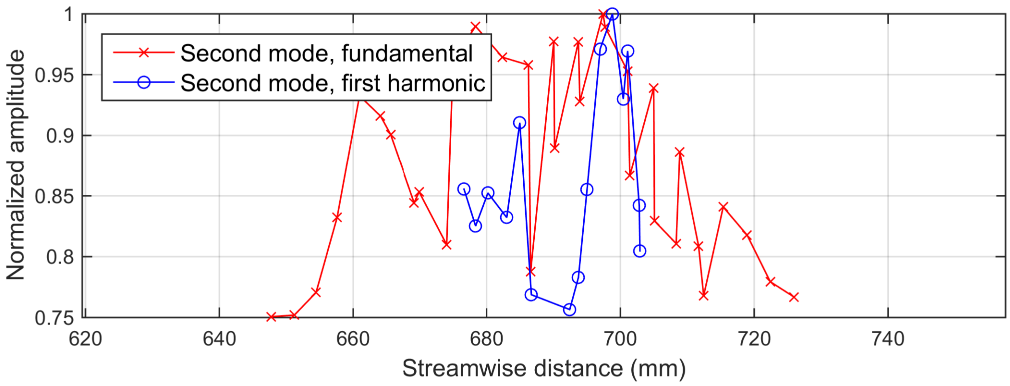

Figure 4.13: Comparing stream wise amplitude distribution of the second mode fundamental wave and its harmonic.

4.3.2. Discussion on growth rates of first harmonic waves from schlieren images

As discussed in the previous section the presence of harmonics of the fundamental wave were strong in run 1438. Fig. 4.14 shows the growth rates of the fundamental and it's first harmonic for a sequence of images from run 1438. From Fig. 4.14 it is observed that the growth rate of the fundamental wave and the harmonic have an inverse relation i.e. where the fundamental wave grows, the harmonic decays and vice versa. For example compare the regions marked in the fundamental and harmonic growth rates at t1+0.136 - t1+0.142 ms. The regions of harmonic amplification are marked by white ellipses and those of harmonic decay by red ellipses in Fig. 4.14. The negative cross correlation coefficients at zero displacement given in the figure also support this observation.

From the regions marked in Fig. 4.14, it can be concluded that the growth rate of the second mode fundamental wave and it's harmonic has an inverse relation. Stetson and Kimmel [47], observed that in the initial stages of second mode development the maximum amplification factor obtained experimentally agreed with the theoretical value. At a later stage, the experimental maximum amplification factor is less than the theoretical calculation (see Fig. 2.3b, section 2.1). Stetson and Kimmel [47] postulated that the reduction in second mode growth rate to be due to the growth of harmonics, which interact and exchange energy with the fundamental wave. The bispectral analysis of Hofferth et al. [16] also revealed that second mode waves interact with its first harmonic. Fig. 3.6e shows that the visualization window for run 1438 is downstream of the point at which transition is initiated, indicating that the boundary layer is transitional. Following the reasoning of Stetson and Kimmel [47] and taking into account the results of Hofferth et al. [16], the observations of Fig. 4.14 show that the amplification of harmonics cause the fundamental wave to decay during transition, indicating a transfer of energy from the fundamental to its harmonic.

4.4. Analysing low frequency waves in schlieren images

While performing the wavelet analysis on schlieren images, it was observed that there was significant amplitude present in lower δ/λ ranges, see Fig. 4.15. Grossir et al. [15] discarded these waves as low frequency noise, but it will be shown that these waves are present within the boundary layer and not scattered throughout the schlieren image and hence cannot be noise. Recently Zhu et al. [53] measured low frequency waves in a hypersonic boundary layer using PCB transducers. In the study of Zhu et al. [53], it was concluded that the second mode waves trigger the growth of low frequency waves through a phase resonance mechanism, and these low frequency waves eventually drives the boundary layer to turbulence while the second mode waves die. In a phase resonance mechanism two waves with equal phase speeds interact with each other to exchange energy. In this section the wavelet analysis is applied to a sequence of schlieren images to investigate the role these low frequency waves play.

Fig. 4.16 shows a sequence of schlieren images capturing second mode waves and a turbulent boundary layer developing at the end of the visualization window. These sequence of events (second mode development to boundary layer transition) can now be studied in different frequency (or wavelength) spaces by applying the wavelet transform. The wavelet transform is applied in two wavelength ranges corresponding to the second mode waves and that of the low frequency waves obtained from Fig. 4.15.

Fig. 4.17 and 4.18 shows the result of applying the wavelet transform to the image sequence. The low frequency waves have considerable amplitude in the sequence analyzed. Unlike the second mode waves the

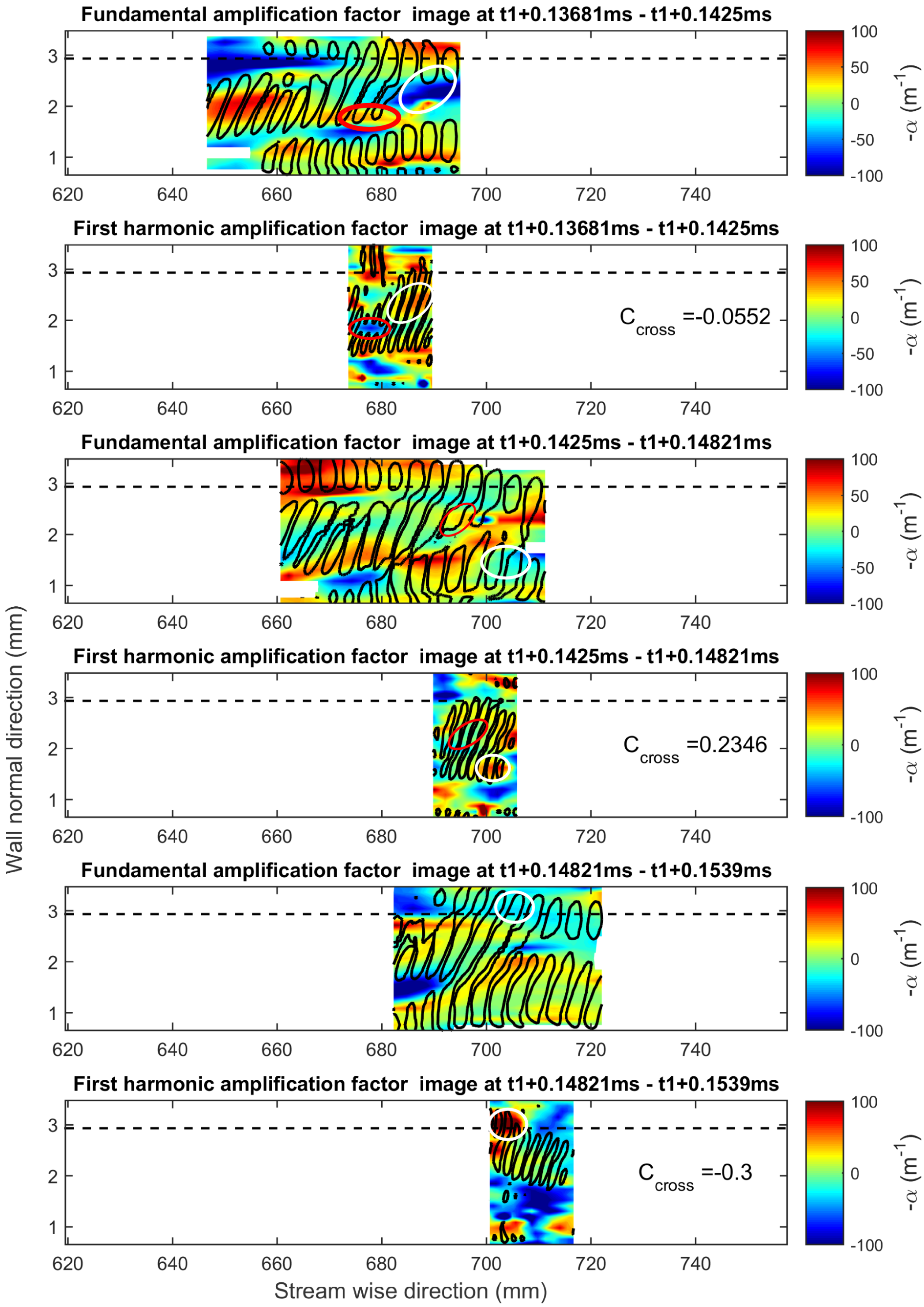

Figure 4.14: Comparing growth rates of second mode fundamental and the first harmonic for a sequence of images from run 1438. Red ellipses indicate region where fundamental wave grows (or harmonic decay) and white ellipses indicate region of fundamental decay (or harmonic growth). Cross correlation coefficients at zero displacement are shown as well.

low frequency waves are concentrated only at the boundary layer edge (Fig. 4.18, Image at $t_0+\Delta t$ - $t_0+3\Delta t$). It is also observed that the second mode waves die as time progresses and is absent at $t_0+8\Delta t$ when the boundary layer is becoming turbulent, where as the low frequency waves are still present. The absence of second mode in a schlieren image could also mean that the wave angle is no longer zero, and the waves have traveled off the plane of view. In the absence of span wise sensors this cannot be verified. The growth of harmonics were weak in this sequence. The results support the observation of Zhu et al. [53] mentioned earlier, that the second mode waves die and the low frequency waves are responsible for boundary layer transition. The wavelength, velocity and frequency of the low frequency waves are shown in table 4.4.

In order to verify that the low frequency waves interact with the second mode waves through a phase resonance mechanism, the speed of the low frequency waves are computed by cross correlating wavelet transforms of schlieren images in the low frequency range (Fig. 4.18). The results of the cross correlation are shown in table 4.3. From table 4.3, it is seen that the second mode waves are faster than the low frequency waves. Since the two waves have different velocities it is seems that the second mode waves and the low frequency waves do not interact with each other through phase resonance mechanism.

There is also a possibility that these low frequency waves are three dimensional waves (non zero wave angle), which will explain why location of the wave is not fixed i.e. at some instances it is at the boundary layer edge and at another it is within the boundary layer, see Image at $t_0+3\Delta t$ and $t_0+4\Delta t$ in Fig. 4.18. The vertical shift of the low frequency waves show its oblique nature. From the linear stability theory results it is known that the first mode wave has a wave angle of 55°, see Fig. 1.2. If the true velocity of the first mode wave is assumed to be equal to free stream velocity. The projection of this velocity on a schlieren image will be $U_\infty \cos 55^\circ$ which is approximately $0.5U_\infty$, similar to the low frequency waves observed in this section. This cannot be verified without span wise sensors, and such sensors must be employed in the future to obtain a complete picture of the processes occurring.

Images Cross-correlated	v_{SM}/v_∞	v_{LFS}/v_∞
Image at $t_0 \times t_0+\Delta t$	0.85	0.57
Image at $t_0+\Delta t \times t_0+2\Delta t$	0.86	0.53
Image at $t_0+2\Delta t \times t_0+3\Delta t$	0.85	0.62
Image at $t_0+3\Delta t \times t_0+4\Delta t$	0.86	0.53

Table 4.3: Velocity of second mode waves and low frequency structures computed by cross correlating wavelet transform of schlieren images.

Instability	λ/δ	v_{SM} (m/s)	f_{LFS} (kHz)
Low frequency	15.3±0.53	1388.63±57	40±3
Second mode	2.25±0.47	2106±1	309±64

Table 4.4: Wavelength, velocity and frequency of the low frequency waves.

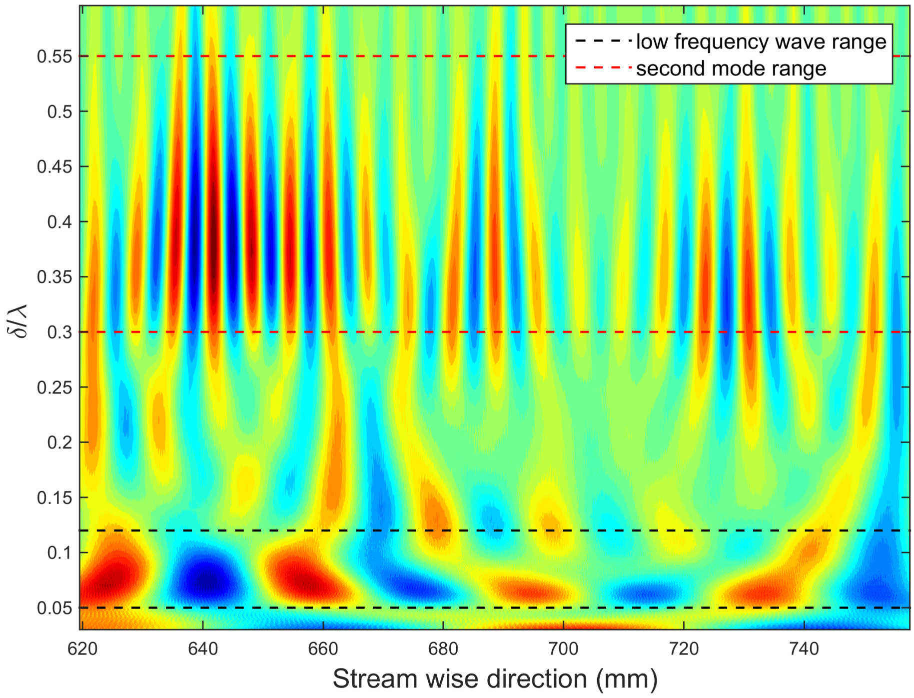

Figure 4.15: Wavelet transform of a row vector from one image, showing δ/λ ranges for the second mode and low frequency waves.

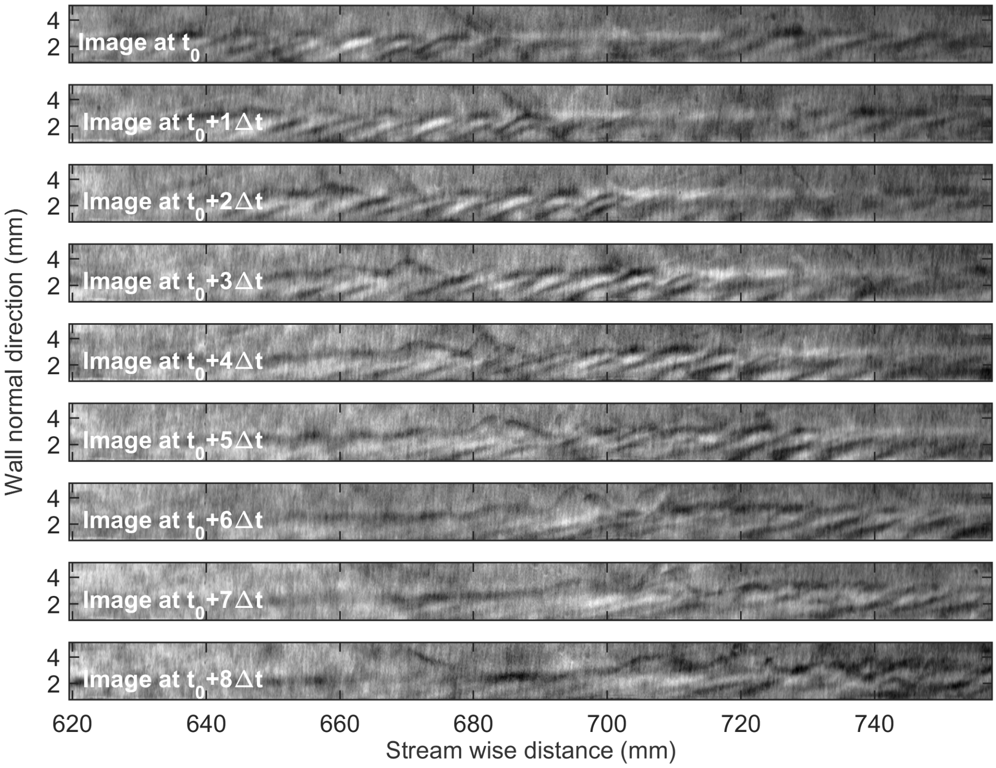

Figure 4.16: Sequence of images from run 1438, with the boundary layer breaking down at the end of visualization window at t_0+8Δt.

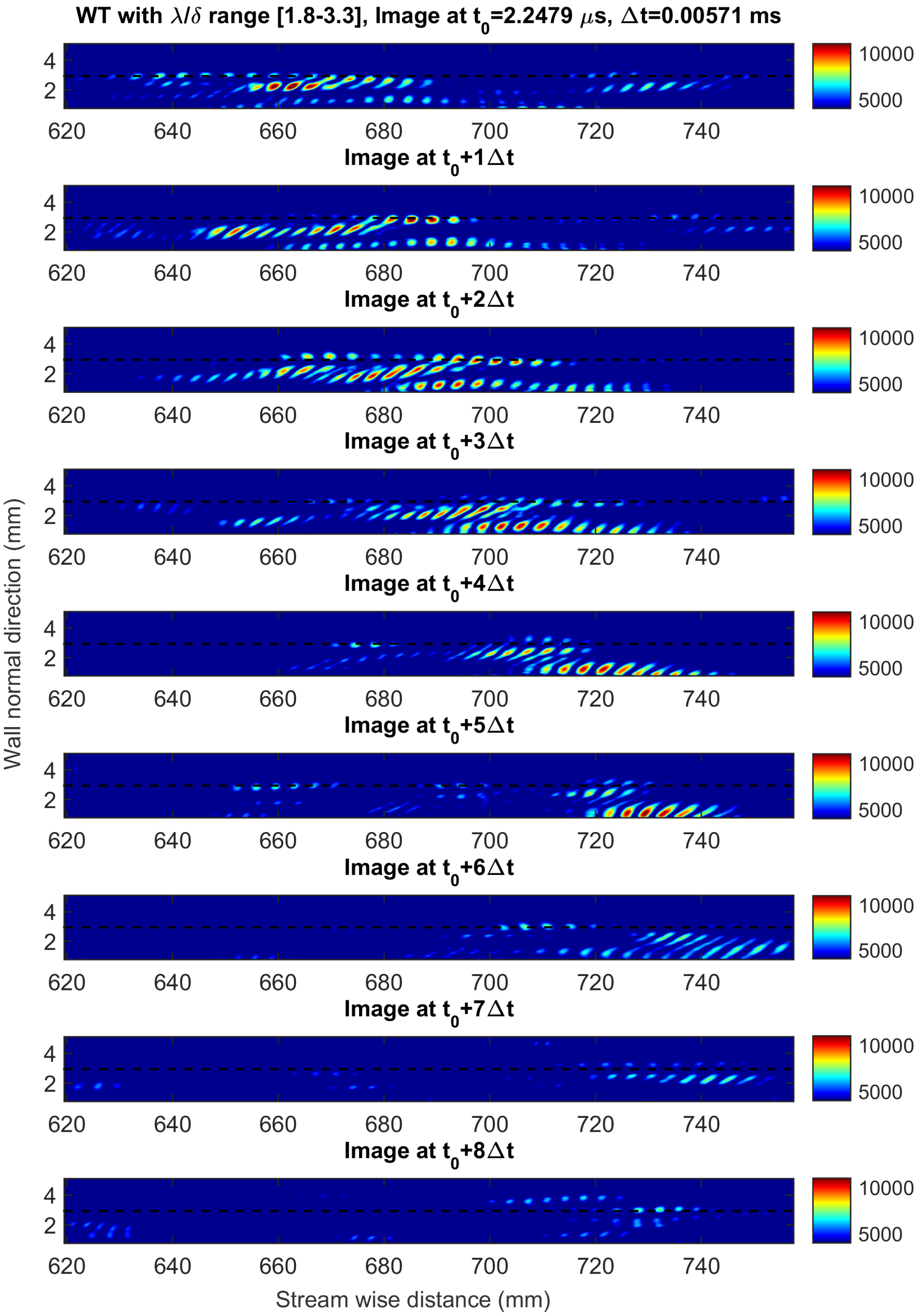

Figure 4.17: Wavelet transform of sequence shown in Fig. 4.16 with λ/δ range corresponding to second mode fundamental wave.

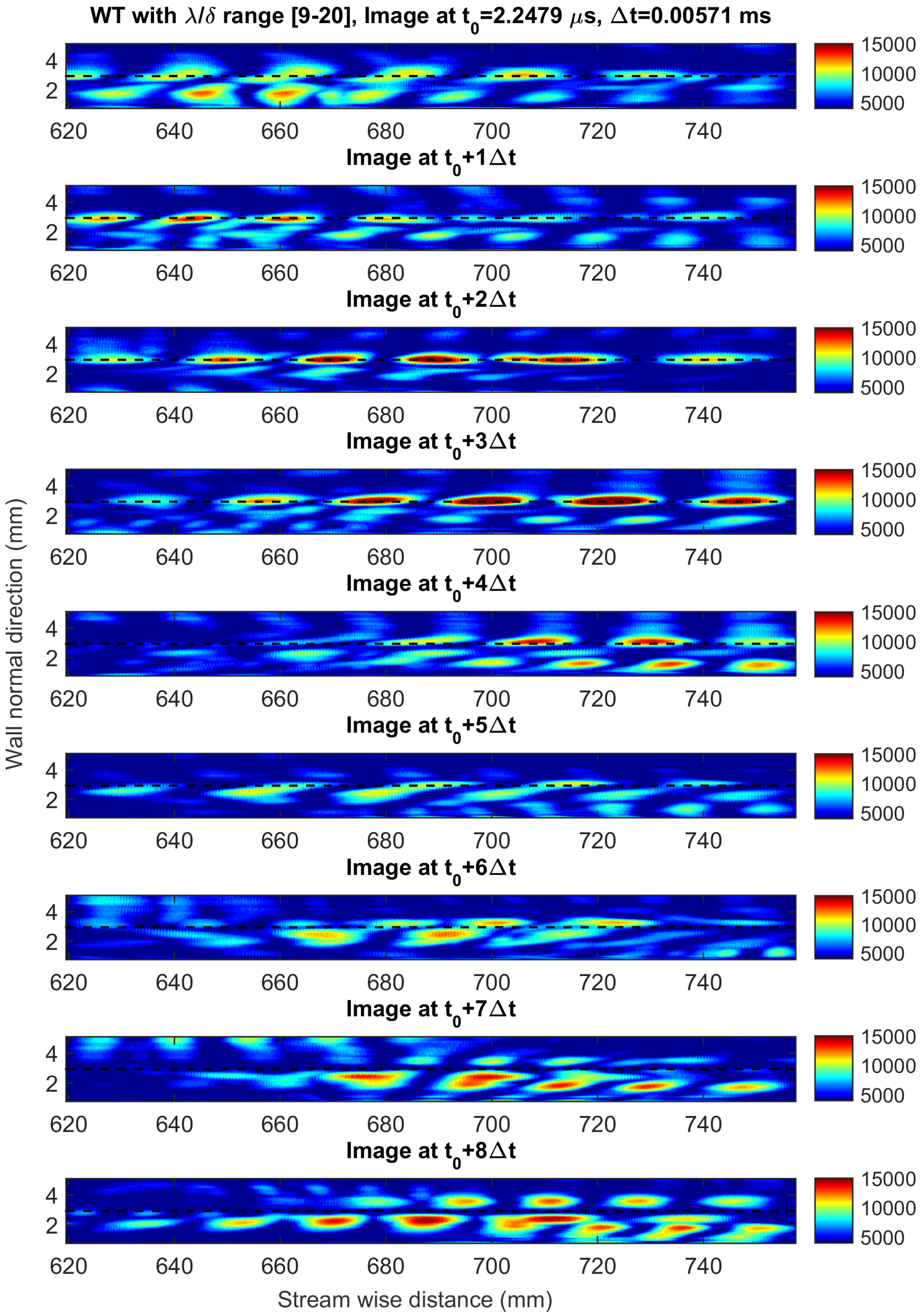

Figure 4.18: Wavelet transform of sequence shown in Fig. 4.16 with λ/δ range corresponding to low frequency waves.

4.5. Summary

In this chapter the wavelet transform was applied to schlieren images to study the properties of the second mode wave. The results can be summarized as follows:

Second mode wavelength and velocity

The wavelength of the second mode instability was found to be 2.2-2.5 times the boundary layer thickness, by taking the Fourier transform of the schlieren images. Schlieren images were cross correlated to find that the velocity of the second mode wave was $0.8V_\infty$. These results are in good agreement with theoretical and previous experimental studies. Using the wavelength and velocity the frequency of the waves are computed, shown in Table 4.1.

Second mode amplitude distribution and growth rates

The wavelet analysis is applied to the schlieren images to study the growth rates and amplitude distribution. Using the frequency of the second mode waves determined using the Fourier analysis, the range of scales of the mother wavelet is selected.

An algorithm was developed to identify the location of the maximum for each individual compression and expansion wave. Plotting the position of the maxima for an entire test case, it is observed that the waves peaks are concentrated towards the boundary layer edge (see Fig. 4.5). This is also supported by study on second mode growth rates which revealed a positive growth rate for structures close to the boundary layer edge, see Fig. 4.11b. The results from this analysis shows that second mode waves amplify structures close to the boundary layer edge.

Numerical[42] and experimental[8] results on the stream wise amplitude distribution of the wave packet prompted a similar study in this thesis. Studying the stream wise amplitude distribution for a sequence of images in section 4.2.2 we see that in the initial stages the amplitude is concentrated in the leading edge of the wave packet agreeing with the DNS results of Sivasubramanian et al. [42]. As the second mode travels energy is first redistributed towards the center of the wave packet for the least transitional boundary layers (agreeing with the experimental observations of Casper et al. [8]). For the modestly transitional and highly transitional boundary layers there is a redistribution from the leading edge to the entire length of the wave packet.

First harmonic development and growth rates

By selecting wavelet scales corresponding to the first harmonic frequency range, the harmonics of the fundamental wave can also be detected by the wavelet analysis (see Fig. 4.12). The first harmonic was observed to be concentrated towards the center of the wave packet similar to the observation of Laurence et al. [25] (see Fig. 2.13). Comparing the stream wise distribution of harmonic and fundamental wave it is concluded that, harmonics develop where the fundamental wave are high (see Fig. 4.13).

Comparing the growth rates of the fundamental and harmonic wave, it is observed that the regions of harmonic amplification correspond to regions of fundamental decay (see Fig. 4.14). Interpreting this in light of the study of Stetson and Kimmel [47], it is concluded that the harmonic grows by extracting energy from the fundamental wave leading to fundamental wave decay.

Low frequency structures

Low frequency structures were observed while analyzing the images, see Fig. 4.15. A sequence of schlieren images capturing second mode waves and boundary layer transition was analyzed in the second mode and low frequency wavelength spectra. It was found that the second mode waves die with time, and the low frequency waves were still present during boundary layer transition. Similar waves were also reported by Zhu et al. [53] in their investigations. Based on the experimental results available for this study (schlieren images), it is concluded that these low frequency waves play a more dominant role during boundary layer transition than the second mode waves which eventually die during the process.

5

Conclusion

The wavelet analysis was successfully applied to schlieren images to identify and study the development of the second mode wave and its first harmonic. Taking the wavelet transform allowed to extract the growth rates of the instability wave and the amplitude distribution in the stream wise and wall normal directions. From the study on the amplification factor and wall normal amplitude distribution of the second mode wave it is concluded that the second mode waves amplifies structures close to the boundary layer edge and shifts the maximum wave amplitude towards the boundary layer edge. These two results explain why previous studies on hypersonic cone boundary layers observed the presence second mode instability to be strong close to the boundary layer edge.

Analysis on the stream wise amplitude distribution of the second mode wave verified the numerical observation that linear wave packets have the maximum amplitude concentrated in the leading edge of the wave packet. The study also showed that as the wave packet develops high amplitudes are redistributed towards the center of the wave packet first, before being uniformly distributed over the length of the wave packet. No harmonic development was observed while the redistribution occurred; hence ruling out the possibility that non linear mechanisms to be the cause for this redistribution. Earlier studies using PCB sensors also showed that the high wave amplitudes were concentrated at the center of the wave packet close to breakdown.

Studies on the first harmonic wave showed that the harmonics develop towards the center of the wave packet where the fundamental wave amplitudes are high, indicating that second mode waves have to grow sufficiently for harmonics to develop. This observation is in line with previous schlieren studies that showed harmonics develop in the center of the wave packet. Comparing the fundamental and harmonic growth rates, it is concluded that the harmonics grow by interacting and extracting energy from the second mode waves. This was hypothesized in early hot wire measurements.

The wavelet analysis also identified the presence of strong low frequency waves in the schlieren images. The waves were observed to have high amplitudes during transition while the second mode waves decayed. The results were in line with the recent studies which propose, that second mode waves grow and interact with low frequency waves, and it is these waves which eventually cause transition. The waves show an oblique nature and there is a possibility of these waves being the first mode wave. A deeper study using surface sensors is crucial to determine the role of these waves during transition.

Numerical results show that the wave packet shows a tendency to become three dimensional as it travels downstream. In the future experiments must be performed using surface mounted sensors in the stream wise and span wise directions, to investigate the three dimensional characteristics of the wave packet. Results circumferential sensors will validate if the wave packet becomes three dimensional during its development which will explain the decay of second mode waves observed in this study. The wave angle of the low frequency waves observed in the schlieren images can be determined using span wise sensors. A comparison with the first mode wave angle from numerical results can verify that these low frequency waves are the first mode waves. Future studies should explore the role these waves play during transition.

The results from this study show that there are two possible interactions the second mode wave can undergo with either its first harmonic or the low frequency waves. Bispectral analysis should be performed on surface sensor signals to understand which of these interactions is stronger and affects transition the most. The possibility to apply bispectral techniques to schlieren images can also be explored. Interactions with oblique second mode waves can also be studied.

A

A.1. Wall normal amplitude distribution

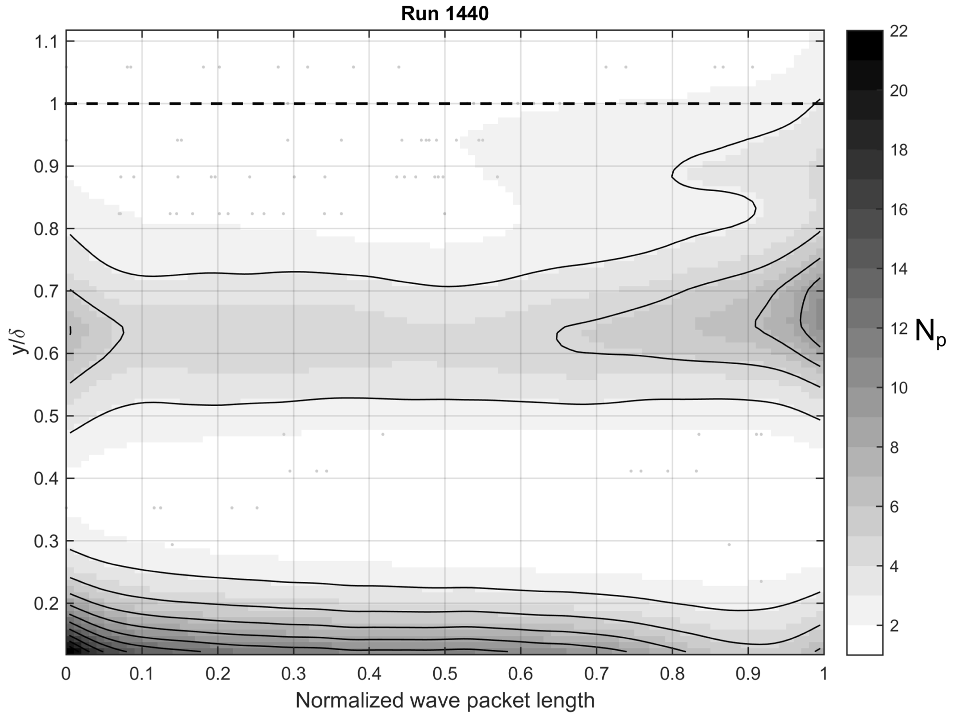

Figure A.1: Movement of the maximum wave amplitude (wave peaks), from run 1440.

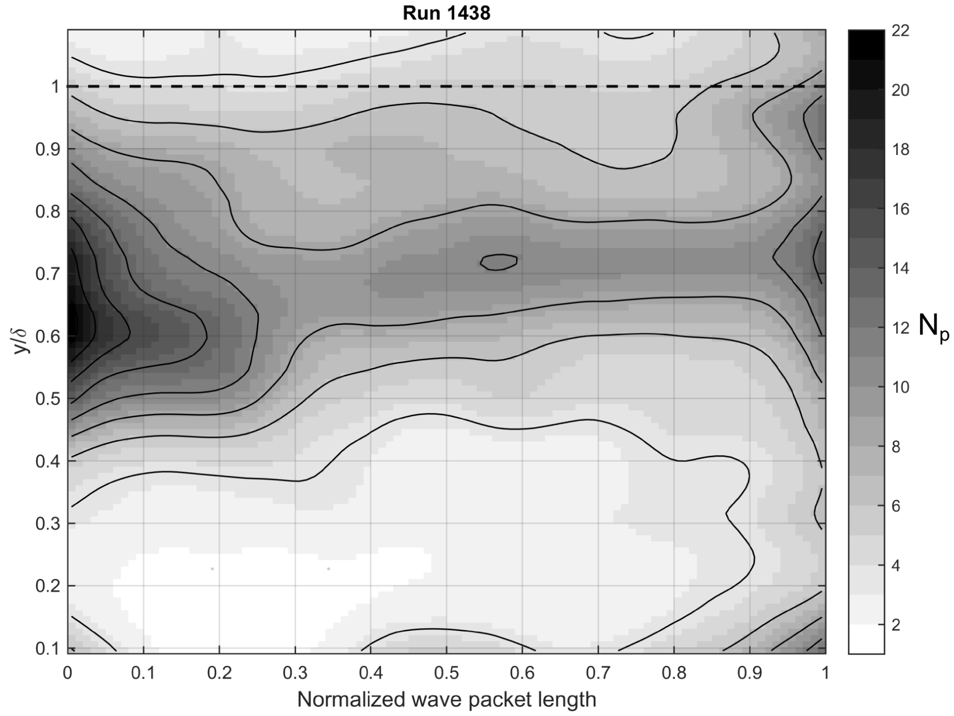

Figure A.2: Movement of the maximum wave amplitude (wave peaks) towards the boundary layer edge first, and then a shift towards the wall for a sequence from run 1438.

A.2. Stream wise energy distribution

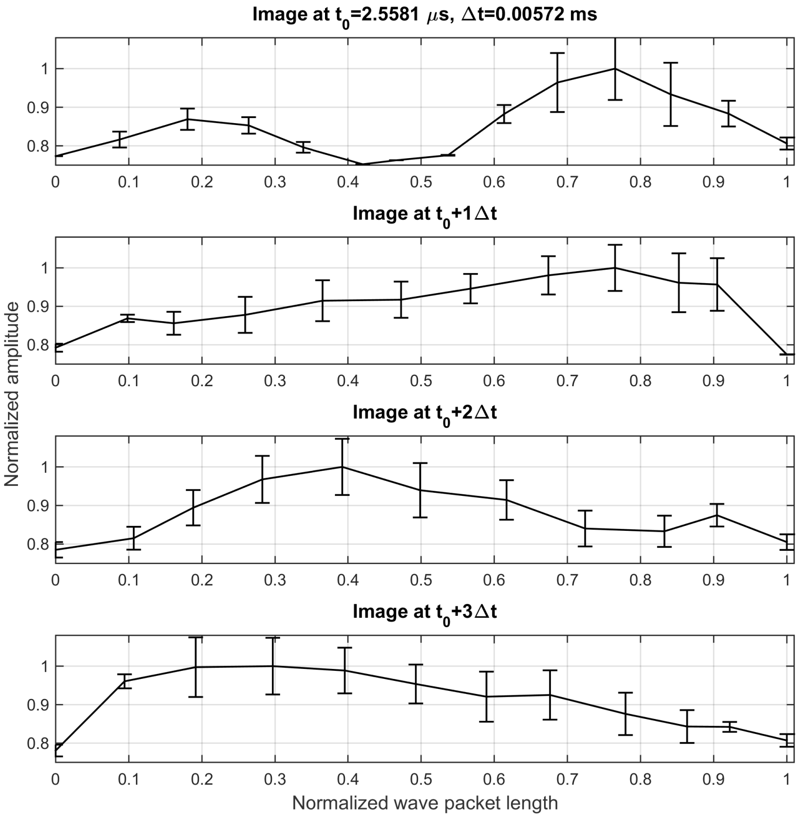

(a) Variation in stream wise energy distribution for a sequence from run 1443. Figure shows the shift of energy concentration from leading edge, to the center of the wave packet and finally to the entire length of the wave packet.

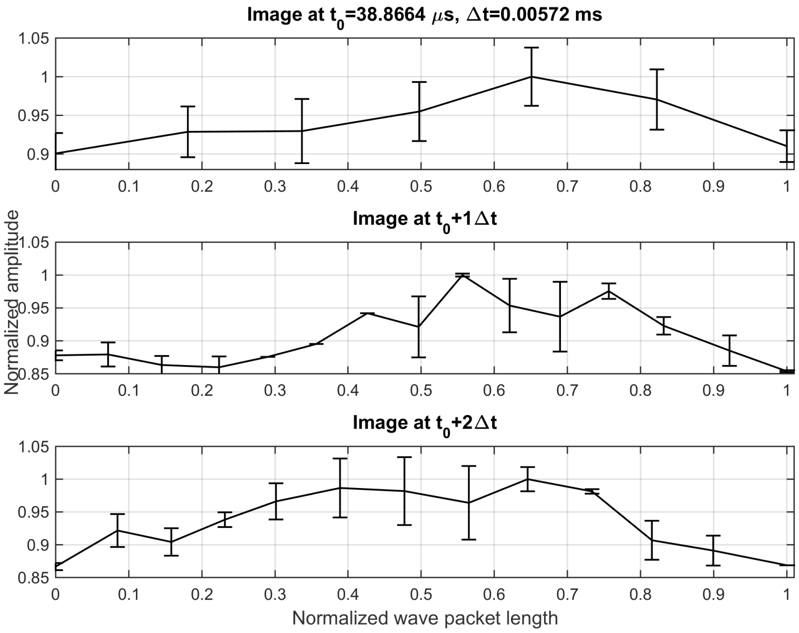

(b) Variation in stream wise energy distribution for a sequence from run 1447. Figure shows the shift of energy concentration from leading edge to the length of the entire wave packet.

Figure A.3: Variation in stream wise energy distribution.

A.3. Growth rate computed from schlieren images

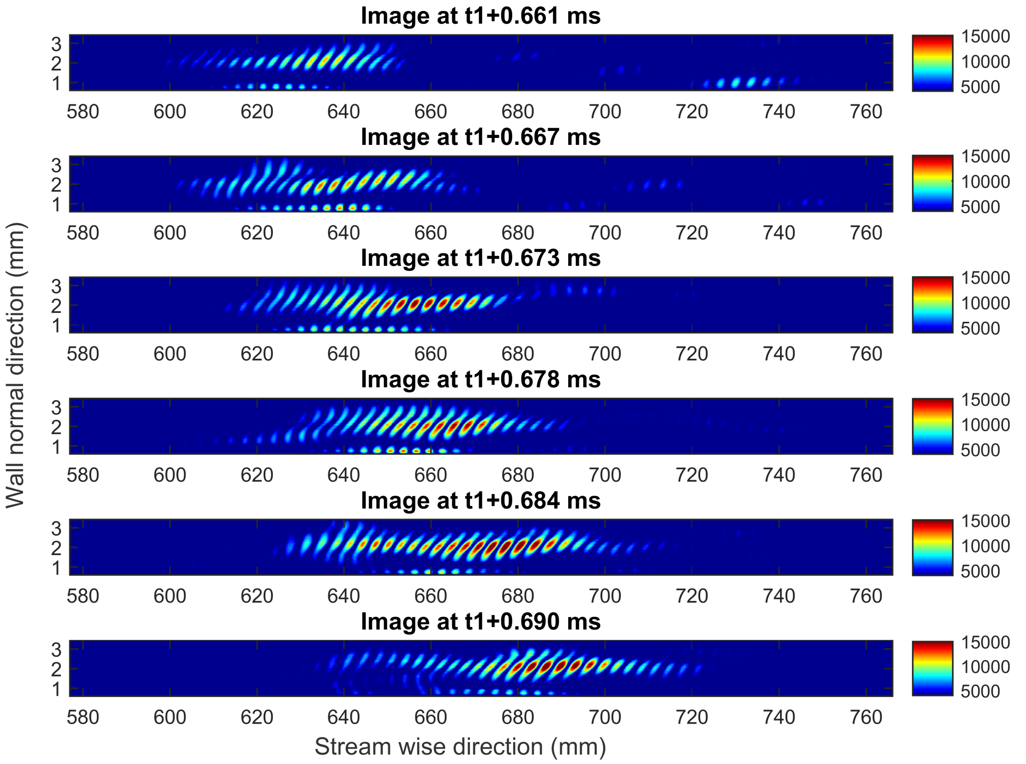

(a) Wavelet transform of images 117-122 of run 1440, used to compute the growth rates in Fig. A.4b.

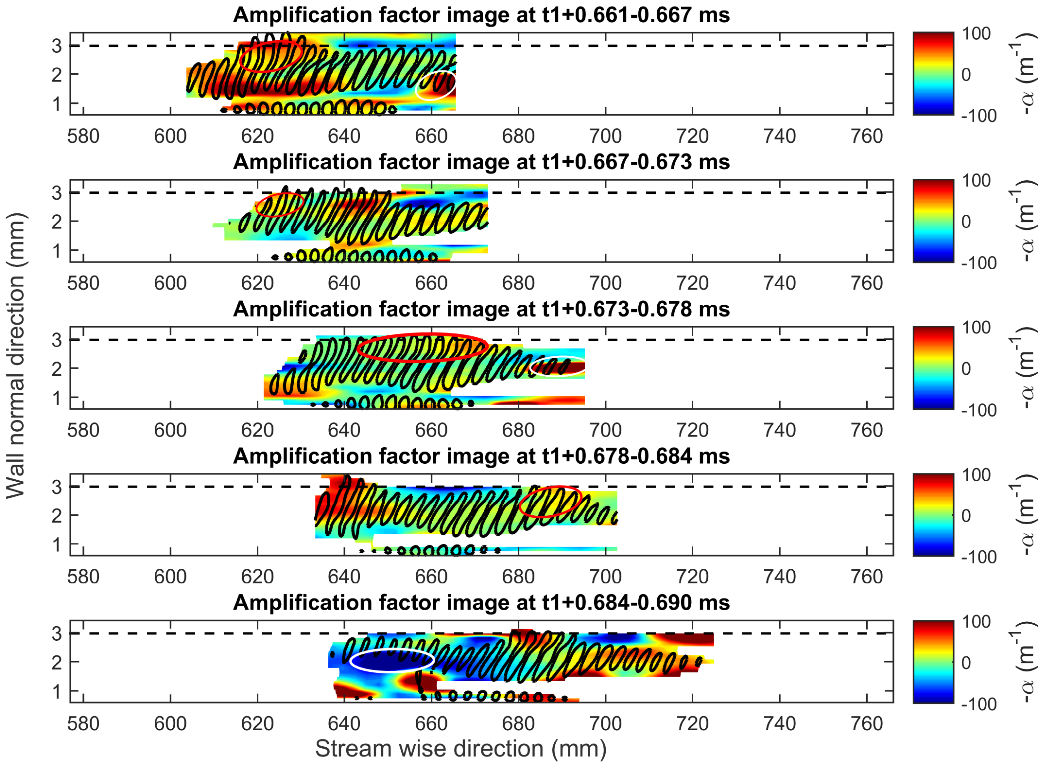

(b) Amplification factor computed from images shown in Fig. A.4a.

Figure A.4: Growth rates for a sequence of images from run 1440. The white ellipses indicate regions of strong growth and decay showing the rapid change in wave packet structure. Red ellipses show amplification of wave close to boundary layer edge.

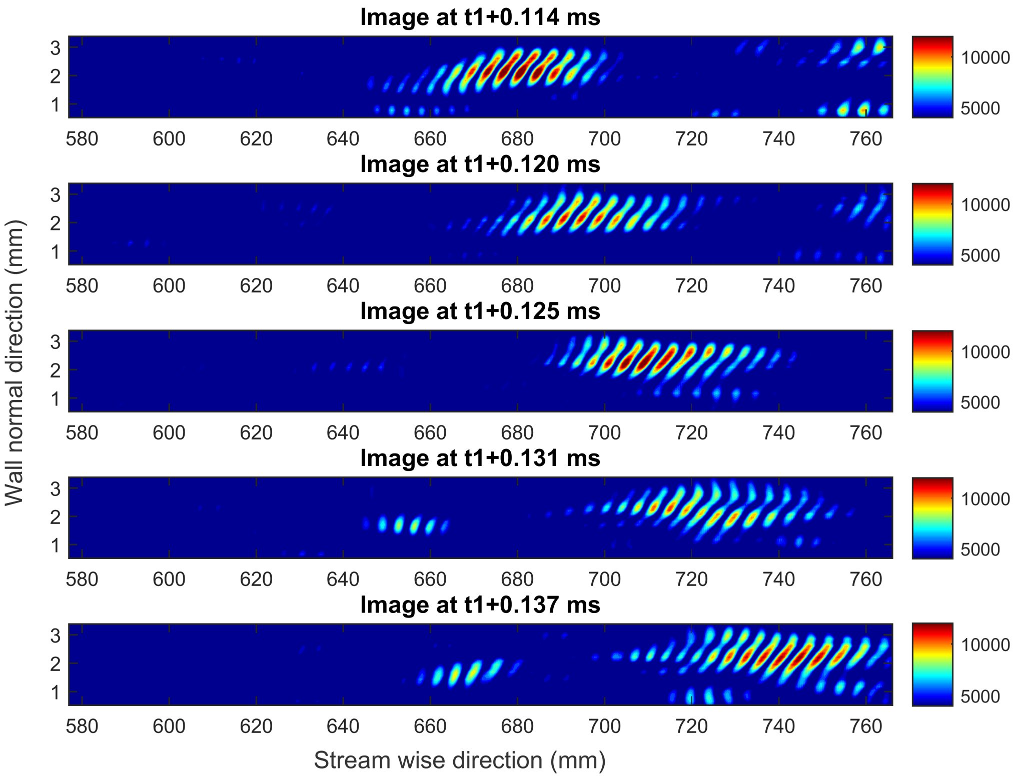

(a) Wavelet transform of images 21-25 of run 1443, used to compute the growth rates in Fig. A.5b.

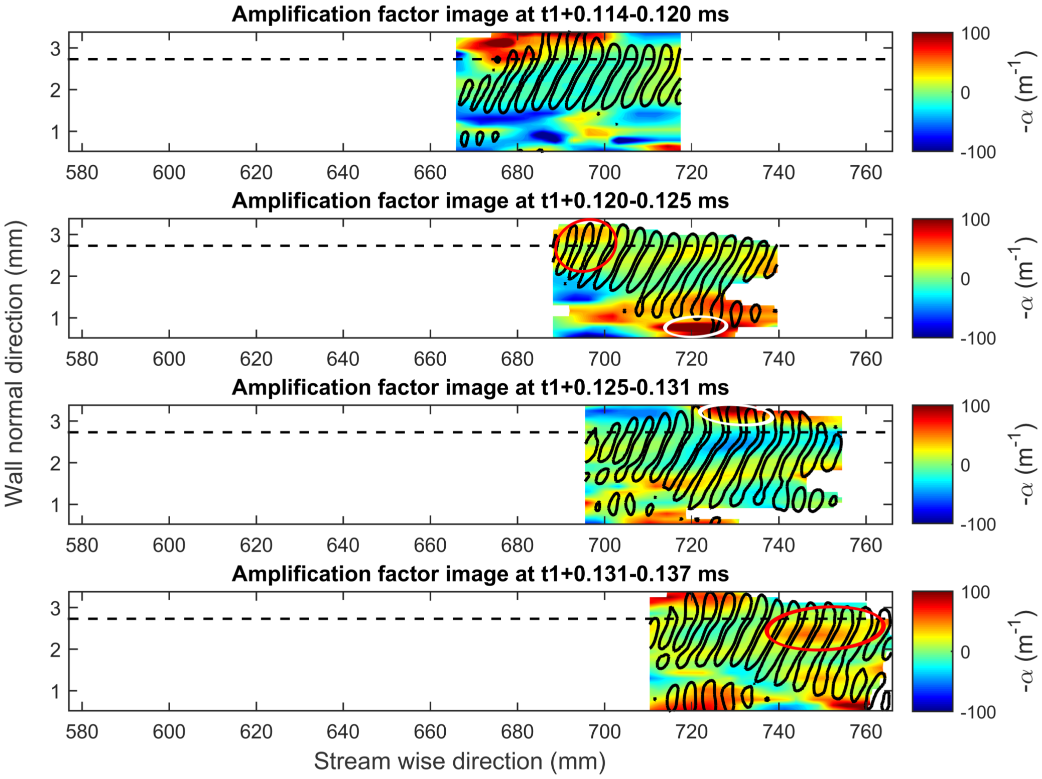

(b) Amplification factor computed from images shown in Fig. A.5a. The white ellipses indicate regions of strong growth and decay showing the rapid change in wave packet structure. Red ellipses show amplification of wave close to boundary layer edge.

Figure A.5: Growth rates for a sequence of images from run 1443.

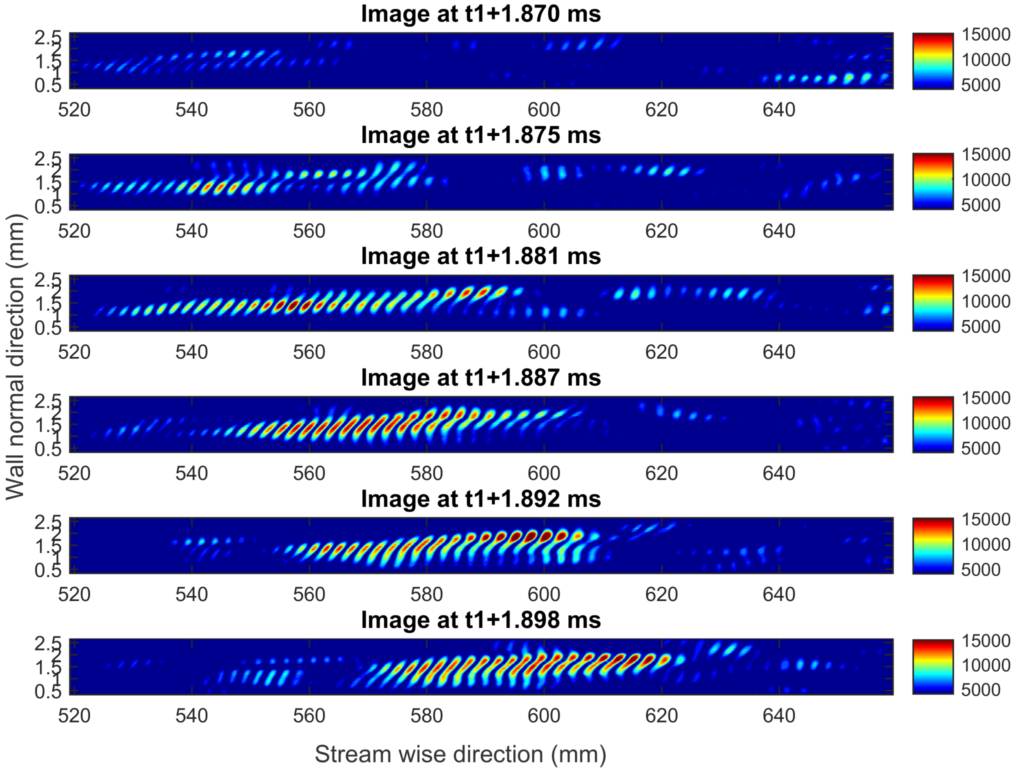

(a) Wavelet transform of images 329-334 of run 1447, used to compute the growth rates in Fig. A.6b.

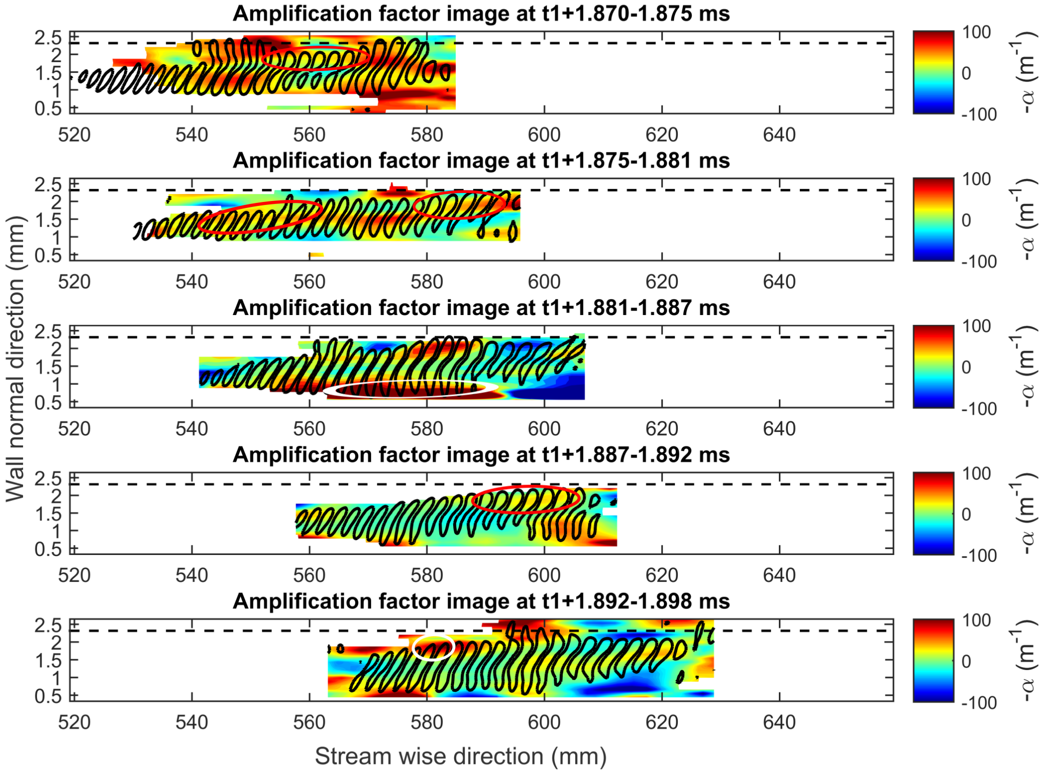

(b) Amplification factor computed from images shown in Fig. A.6a. The white ellipses indicate regions of strong growth and decay showing the rapid change in wave packet structure. Red ellipses show amplification of wave close to boundary layer edge.

Figure A.6: Growth rates for a sequence of images from run 1447.

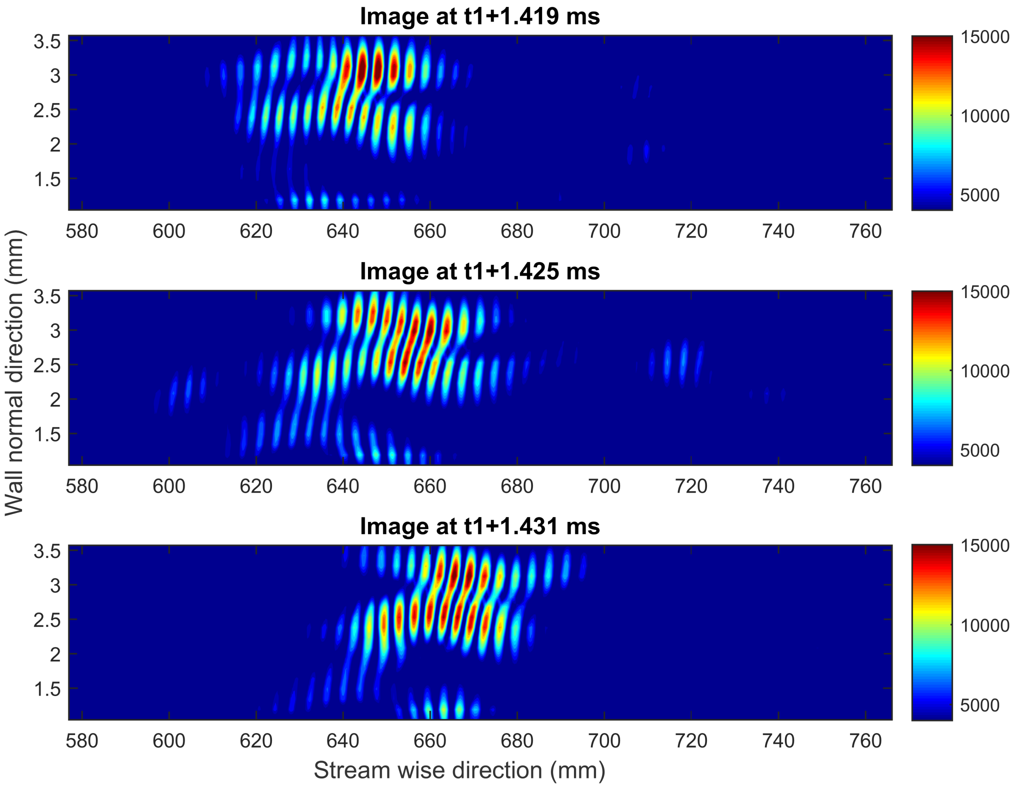

(a) Wavelet transform of images 250-252 of run 1439, used to compute the growth rates in Fig. A.7b.

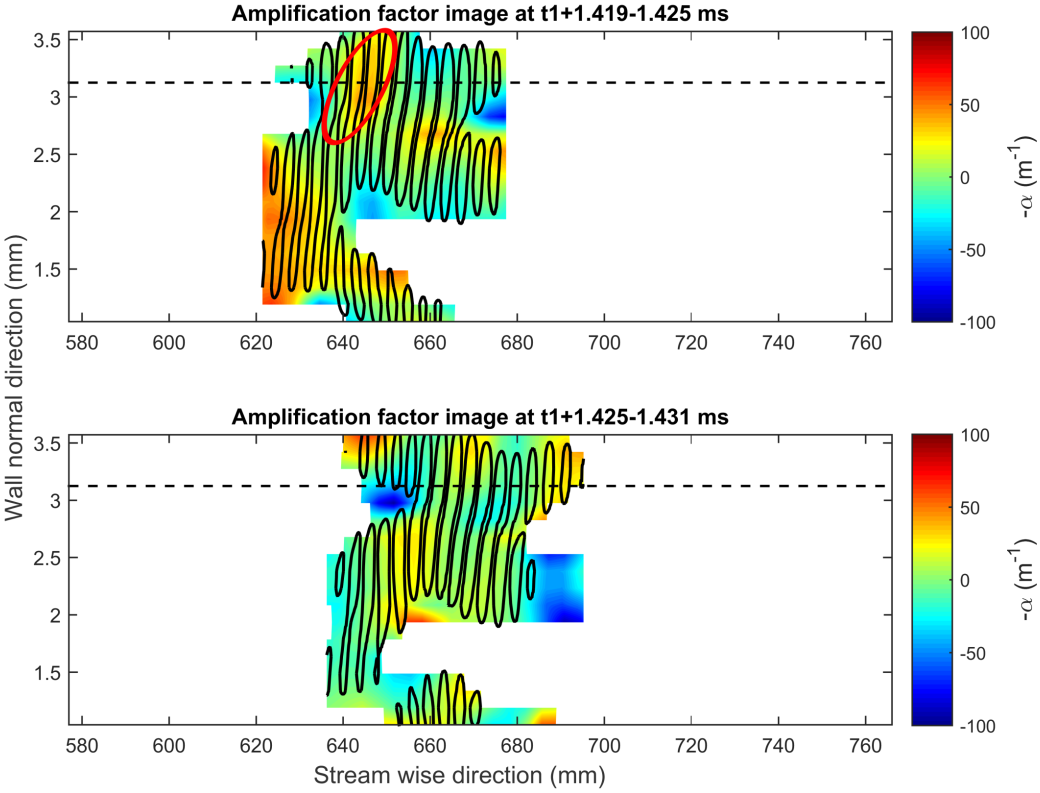

(b) Amplification factor computed from images shown in Fig. A.7a. The white ellipses indicate regions of strong growth and decay showing the rapid change in wave packet structure. Red ellipses show amplification of wave close to boundary layer edge.

Figure A.7: Growth rates for a sequence of images from run 1439.

A.4. Analyzing harmonics

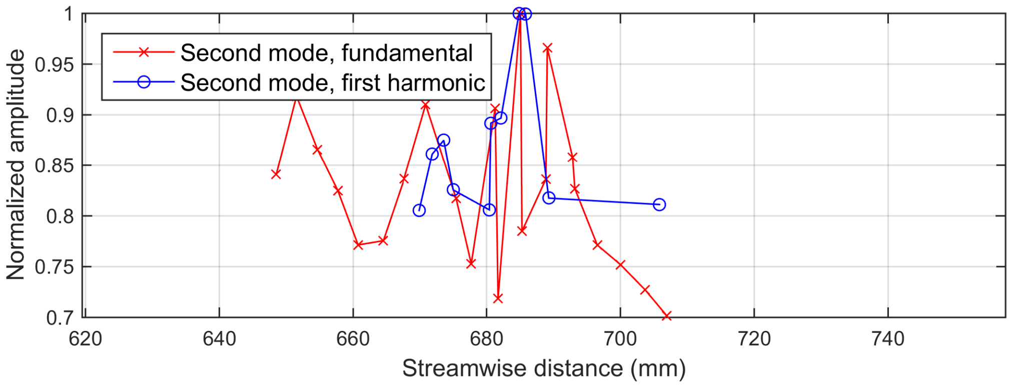

(a) Run 1438.

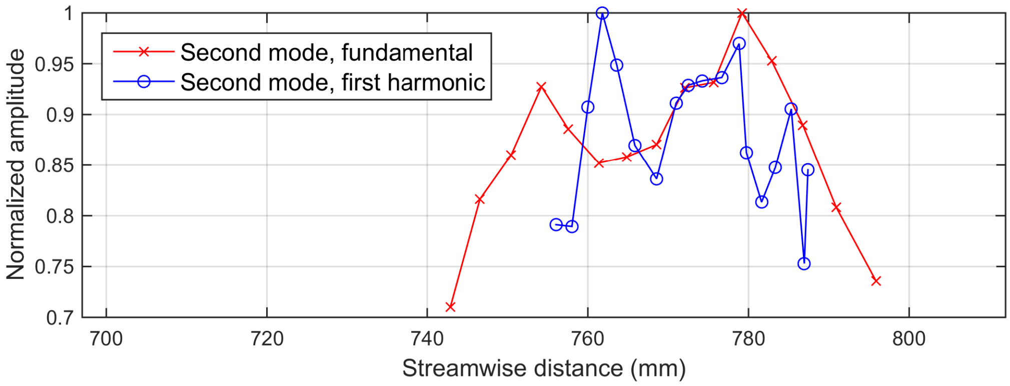

(b) Run 1308.

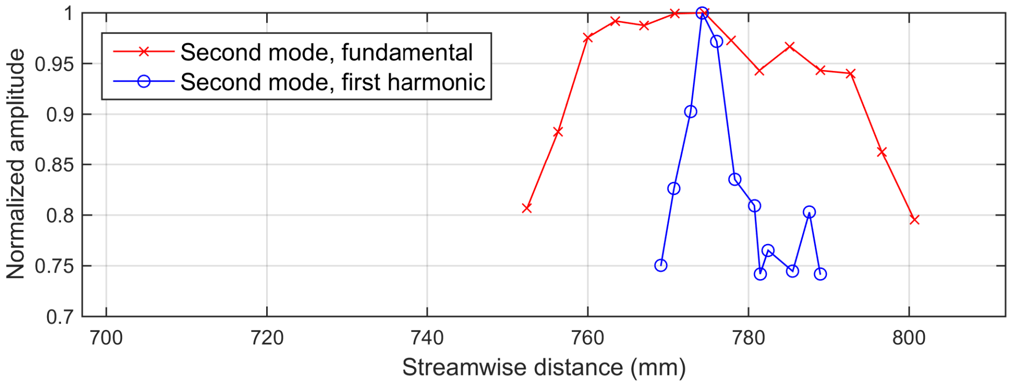

(c) Run 1308.

Figure A.8: Comparing stream wise energy distribution of the fundamental wave with its harmonics.

Bibliography

[1] John David Anderson. *Introduction to flight.* McGraw-Hill, 1989.

[2] John David Anderson. *Hypersonic and high temperature gas dynamics.* Aiaa, 2000.

[3] Paul M Bentley and JTE McDonnell. Wavelet transforms: an introduction. *Electronics & communication engineering journal*, 6(4):175–186, 1994.

[4] Karen Berger, Shann Rufer, Roger Kimmel, and David Adamczak. Aerothermodynamic characteristics of boundary layer transition and trip effectiveness of the hifire flight 5 vehicle. volume 4055, page 2009, 2009.

[5] Dennis C Berridge, Katya M Casper, Shann J Rufer, Christopher R Alba, Daniel R Lewis, Steven J Beresh, and Steven P Schneider. Measurements and computations of second-mode instability waves in three hypersonic wind tunnels. *AIAA paper*, 5002, 2010.

[6] K. M. Casper, S. J. Beresh, J. F. Henfling, R. W. Spillers, and B. O. M. Pruett. High-speed schlieren imaging of disturbances in a transitional hypersonic boundary layer. In *51st AIAA Aerospace Sciences Meeting including the New Horizons Forum and Aerospace Exposition*, number AIAA 2013-0376, Grapevine (Dallas/Ft. Worth Region), Texas, January 2013. AIAA. doi: 10.2514/6.2013-376. AIAA 2013-0376.

[7] Katya M. Casper, Steven J. Beresh, Ross M. Wagnild, John F. Henfling, Russell W. Spillers, and Brian O. M. Pruett. Simultaneous pressure measurements and high-speed schlieren imaging of disturbances in a transitional hypersonic boundary layer. In *43rd Fluid Dynamics Conference*, number AIAA 2013-2739, San Diego, CA, June 2013. AIAA. doi: 10.2514/6.2013-2739.

[8] Katya M Casper, Steven J Beresh, and Steven P Schneider. Pressure fluctuations beneath instability wavepackets and turbulent spots in a hypersonic boundary layer. *Journal of Fluid Mechanics*, 756:1058–1091, 2014.

[9] Katya M Casper, Steven J Beresh, John F Henfling, Russell W Spillers, Brian OM Pruett, and Steven P Schneider. Hypersonic wind-tunnel measurements of boundary-layer transition on a slender cone. *AIAA Journal*, pages 1–14, 2016.

[10] A. Demetriades. Hypersonic viscous flow over a slender cone, part iii: Laminar instability and transition. In *AIAA 7th Fluid and Plasma Dynamics Conference*, 1974. AIAA74-535.

[11] G Eitelberg. First results of calibration and use of the heg. In *25th Plasmadynamics and Lasers Conference*, page 2525, 1994.

[12] M. Estorf, R. Radespiel, S. P. Schneider, H. B. Johnson, and S. Hein. Surface-pressure measurements of second-mode instability in quiet hypersonic flow. In *46th AIAA Aerospace Sciences Meeting and Exhibit*, Reno, Nevada, January 2008. AIAA 2008-1153.

[13] Marie Farge. Wavelet transforms and their applications to turbulence. *Annual review of fluid mechanics*, 24(1):395–458, 1992.

[14] Guillaume Grossir, Fabio Pinna, Gabriele Bonucci, Tamas Regert, Patrick Rambaud, and Olivier Chazot. Hypersonic boundary layer transition on a 7 degree half-angle cone at mach 10. *AIAA Paper*, 2779, 2014.

[15] Guillaume Grossir, Davide Masutti, and Olivier Chazot. Flow characterization and boundary layer transition studies in vki hypersonic facilities. page 0578, 2015.

[16] Jerrod Hofferth, Raymond Humble, Daniel Floryan, and William Saric. High-bandwidth optical measurements of the second-mode instability in a mach 6 quiet tunnel. page 378, 2013.

[17] J. M. Kendall. Wind tunnel experiments relating to supersonic and hypersonic boundary-layer transition. *AIAA Journal*, 13(3):290–299, 1975.

[18] R. L. Kimmel, A. Demetriades, and Joseph C. Donaldson. Space-time correlation measurements in a hypersonic transitional boundary layer. *AIAA Journal*, 12(12):2484–2489, December 1996.

[19] Roger L Kimmel and Jonathan Poggie. Disturbance evolution and breakdown to turbulence in a hypersonic boundary layer—ensemble-averaged structure. *AIAA Paper*, 555, 1997.

[20] Jason T Lachowicz, Ndaona Chokani, and Stephen P Wilkinson. Boundary-layer stability measurements in a hypersonic quiet tunnel. *AIAA journal*, 34(12):2496–2500, 1996.

[21] Jason T Lachowicz, Ndaona Chokani, and Stephen P Wilkinson. Hypersonic boundary layer stability over a flared cone in a quiet tunnel. *AIAA paper*, 96:0782, 1996.

[22] S. Laurence, A. Wagner, K. Hannemann, V. Wartemann, H. Lüdeke, H. Tanno, and K. Ito. Time-resolved visualization of instability waves in a hypersonic boundary layer. *AIAA Journal*, Vol. 50(1):243–246, January 2012. doi: 10.2514/1.J051112.

[23] S. Laurence, A. Wagner, and K. Hannemann. Schlieren-based techniques for investigating instability development and transition in a hypersonic boundary layer. *Experiments in Fluids*, 55(8), 2014. ISSN 0723-4864. doi: 10.1007/s00348-014-1782-9.

[24] S. Laurence, A. Wagner, Hiroshi Ozawa, and K. Hannemann. Visualization of hypersonic boundary-layer transition on a slender cone (invited). In *19th AIAA International Space Planes and Hypersonic Systems and Technologies Conference*, 2014. doi: 10.2514/6.2014-3110. URL `http://dx.doi.org/10.2514/6.2014-3110`. AIAA 2014-3110.

[25] SJ Laurence, A Wagner, and K Hannemann. Experimental study of second-mode instability growth and breakdown in a hypersonic boundary layer using high-speed schlieren visualization. *Journal of Fluid Mechanics*, 797:471–503, 2016.

[26] Xinliang Li, Dexun Fu, and Yanwen Ma. Direct numerical simulation of hypersonic boundary layer transition over a blunt cone with a small angle of attack. *Physics of Fluids (1994-present)*, 22(2):025105, 2010.

[27] L. M. Mack. Boundary layer stability theory. Technical Report NASA-CR-131501, Jet Propulsion Laboratory, NASA, 1969.

[28] L. M. Mack. Boundary layer linear stability theory. *AGARD - Special Course on Stability and Transition of Laminar Flow*, 1984.

[29] L. M. Mack. On the inviscid acoustic-mode instability of supersonic shear flows. *Theoretical and Computational Fluid Dynamics*, 2:97–123, 1990.

[30] Leslie M Mack. Boundary-layer stability analysis for sharp cones at zero angle-of-attack. Technical report, DTIC Document, 1986.

[31] Michel Misiti, Yves Misiti, Georges Oppenheim, and Jean P Michel. Wavelet toolbox: for use with matlab. 1996.

[32] Michel Misiti, Yves Misiti, Georges Oppenheim, and Jean-Michel Poggi. Matlab wavelet toolbox user\'s guide. version 3. 2004.

[33] NJ Parziale, JE Shepherd, and HG Hornung. Differential interferometric measurement of instability in a hypervelocity boundary layer. *AIAA journal*, 51(3):750–754, 2012.

[34] NJ Parziale, JE Shepherd, and HG Hornung. Differential interferometric measurement of instability at two points in a hypervelocity boundary layer. In *AIAA 51st Aerospace Sciences Meeting*, number 2013-0521, 2013.

[35] NJ Parziale, JE Shepherd, and HG Hornung. Observations of hypervelocity boundary-layer instability. *Journal of Fluid Mechanics*, 781:87–112, 2015.

[36] J Leith Potter and Jack D Whitfield. Boundary-layer transition under hypersonic conditions(boundary layer transition under hypersonic conditions- reynolds number tendency to increase with mach number). Technical report, AGARDograph No 97, Part 3, 1965.

[37] T. Roediger, H. Knauss, E. Kramer, M. Estorf, S. P. Schneider, and B. V. Smorodsky. Hypersonic instability waves measured using fast-response heat-flux gauges. *AIAA*, 2008-638:1–11, 2008. 46th AIAA Aerospace Science Meeting and Exhibit 7-10 January 2008, Reno, Nevada.

[38] N Shumway and S Laurence. Methods for identifying key features in schlieren images from hypersonic boundary-layer stability experiments. *AIAA Paper*, 1787, 2015.

[39] J. Sivasubramanian and H. F. Fasel. Direct numerical simulation of a turbulent spot in a cone boundary-layer at mach 6. In *40th Fluid Dynamics Conference and Exhibit*, Chicago, Illinois, June and July 2010. AIAA. AIAA 2010-4599.

[40] Jayahar Sivasubramanian and Hermann F Fasel. Numerical investigation of the development of three-dimensional wavepackets in a sharp cone boundary layer at mach 6. *Journal of Fluid Mechanics*, 756: 600–649, 2014.

[41] Jayahar Sivasubramanian and Hermann F Fasel. Direct numerical simulation of transition in a sharp cone boundary layer at mach 6: fundamental breakdown. *Journal of Fluid Mechanics*, 768:175–218, 2015.

[42] Jayahar Sivasubramanian, Christian SJ Mayer, Andreas C Laible, and Hermann F Fasel. Numerical investigation of wavepackets in a hypersonic cone boundary layer at mach 6. *AIAA paper*, 3560, 2009.

[43] Linda G Smith. Pulsed-laser schlieren visualization of hypersonic boundary-layer instability waves. In *AIAA, Aerospace Ground Testing Conference, 18 th, Colorado Springs, CO*, 1994.

[44] Steven W Smith et al. *The scientist and engineer's guide to digital signal processing*. California Technical Pub. San Diego, 1997.

[45] E SOFTLEY. Boundary layer transition on hypersonic blunt, slender cones. In *2nd Fluid and Plasma Dynamics Conference*, page 705, 1969.

[46] Kenneth Stetson and Roger Kimmel. On the breakdown of a hypersonic laminar boundary layer. In *Aerospace Sciences Meetings*, pages –. American Institute of Aeronautics and Astronautics, January 1993. doi: 10.2514/6.1993-896. URL `http://dx.doi.org/10.2514/6.1993-896`.

[47] Kenneth F Stetson and Roger L Kimmel. On hypersonic boundary-layer stability. In *AIAA, Aerospace Sciences Meeting and Exhibit, 30 th, Reno, NV*, page 1992, 1992.

[48] KF Stetson, ER Thompson, JC Donaldson, and LG Siler. Laminar boundary layer stability experiments on a cone at mach 8. i- sharp cone. In *American Institute of Aeronautics and Astronautics, Fluid and Plasma Dynamics Conference, 16 th, Danvers, MA*, 1983.

[49] Colin P VanDercreek, Michael S Smith, and Kenneth H Yu. Focused schlieren and deflectometry at aedc hypervelocity wind tunnel no. 9. *AIAA Paper*, 4209:2010, 2010.

[50] A. Wagner. *Passive Hypersonic Boundary Layer Transition Control Using Ultrasonically Absorptive Carbon-Carbon Ceramic with Random Microstructure*. PhD thesis, Katholieke Universiteit Leuven, 2014. URL `https://lirias.kuleuven.be/handle/123456789/463042`.

[51] Alexander Wagner, Klaus Hannemann, Viola Wartemann, and Tobias Giese. Hypersonic boundary-layer stabilization by means of ultrasonically absorptive carbon–carbon material—part 1: experimental results. *AIAA paper*, 270, 2013.

[52] Frank M White. *Viscous fluid flow*, volume 3. McGraw-Hill New York, 2006.

[53] Yiding Zhu, Chuanhong Zhang, Xi Chen, Huijing Yuan, Jiezhi Wu, Shiyi Chen, Cunbiao Lee, and Mohamed Gad-el Hak. Transition in hypersonic boundary layers: Role of dilatational waves. *AIAA Journal*, pages 1–11, June 2016. ISSN 0001-1452. doi: 10.2514/1.J054702. URL `http://dx.doi.org/10.2514/1.J054702`.